

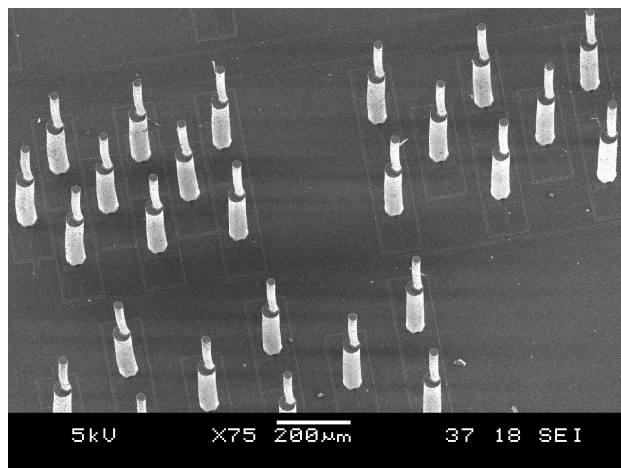
University of Twente

Faculty of
Electrical Engineering,
Mathematics and Computer Science



Master of Science Thesis

Viscous Coupling Between Bio-Inspired Hair-Sensors



Björn Hagedoorn

Master of Science Thesis

Viscous coupling between bio- inspired hair-sensors

Björn Hagedoorn

*University of Twente
Department of Electrical Engineering
Chair for Transducer Science and Technology
Enschede, The Netherlands*

Supervisors: Prof. Dr. Ir. G.J.M. Krijnen
Prof. Dr. Ir. H.W.M. Hoeijmakers
Dr. Ir. R.J. Wiegerink
Ing. R.G.P. Sanders
R. Kottumakulal Jaganatharaja

Period of work: May 2007 - April 2009
Date: April 17, 2009

1	Introduction	2
1.1	Mechano-receptors - a source of inspiration	2
1.2	Original project description	3
2	Theory	4
2.1	Introduction	4
2.2	Viscous coupling	4
2.3	Previous research on viscous coupling	6
2.4	Hair sensors	7
2.5	Hair sensor model	8
2.6	Oscillating flow	9
2.7	Capacitance model	11
2.8	Mechanical hair sensor analysis	17
2.9	Electrostatic hair sensor analysis	21
2.10	The very near field	26
3	Design	27
3.1	Introduction	27
3.2	Sensor design	27
3.3	Experimentation platform design	29
4	Fabrication and inspection	32
4.1	Introduction	32
4.2	Fabrication process	32
4.3	Inspection	34
5	Experiments and results	36
5.1	Introduction	36
5.2	Measurement plan	36
5.3	Laser vibrometry	37
5.4	Loudspeaker calibration	40
5.5	Acoustic experiments and results	42
5.6	Electrostatic experiments and results	48
5.7	Modal decomposition	49
6	Conclusions	52
6.1	Future improvements	52
	References	54
A.	Appendix , Device reference list	56

1 Introduction

1.1 Mechano-receptors - a source of inspiration

For many years, biological organs and processes (incl. sensing, actuation and neural activity) found on different species of animals, have always been a source of inspiration for engineers. Working together with biologists and studying these sophisticated biological systems, engineers have been very successful in developing systems mimicking these natural phenomena. Using the biological knowledge, many engineered equivalents of these complex biological systems have since been introduced. This field of engineering inspired from the nature is commonly known as biomimetics.

Recently, biologists and engineers across Europe are working together in the Custom Intelligent Life Inspired Array project (CILIA), focusing on the mechano-receptive sensor arrays found on arthropods and fish. Using the knowledge gathered by the biologists, engineers are attempting to implement similar sensing arrays in engineered systems. A primary difference between the sensor array systems found on arthropods (crickets, spiders, etc.) and fish is that the former operates in air while the latter, obviously operates in water.

Cricket have evolved with a highly sensitive system of mechano-receptive hairs that are able to pick up low-frequency air flows [Fig. 1-1]. The sensory hairs are radially distributed on a pair of special appendages called cerci, located at the back of the abdomen of the cricket [1]. These hairs are used to sense the approaching predators and therefore, play a predominant role in the escape mechanism of the crickets [2].

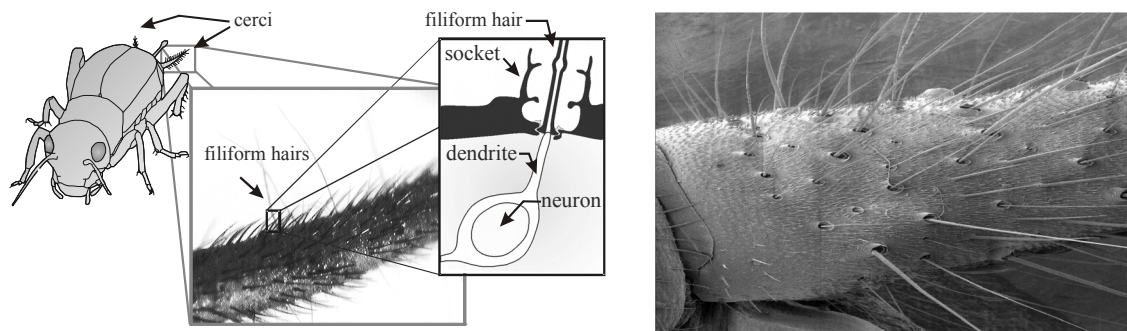


Fig. 1-1: Location of the cerci on crickets and a close-up SEM image showing the mechano-receptive hairs. [SEM image courtesy to Jérôme Casas, IRBI, Université de Tours.]

The cercal hairs vary in length between 30 μm and 1500 μm and have diameters ranging from 1.5 μm to 9 μm [3,4]. The direction of sensitivity varies among the different hairs [5,6]. This enables the cricket to pick up flow perturbations in its surrounding environment. The difference in the hair length makes them sensitive in different frequency ranges [3]. Each of the mechano-receptive hairs is lodged in a socket under which a sensory neuron is also located. When a hair is triggered, the neuron instantaneously fires a neural signal to the abdominal ganglion, where it will further processed [5,6]. Hence, by using this system of highly sensitive mechano-receptive hairs, the cricket is able to pick up velocity amplitudes as low as 0.03 mm/s and respond appropriately to the attacks from its predators [7].

Because of their high sensitivities to extremely low-range flow velocities, engineers are attempting to mimic these arrays of mechanical receptors. Making use of the state-of-the-art MEMS technology, high density arrays of SU-8 based artificial hair sensors have been successfully fabricated recently [Fig. 1-2][8].

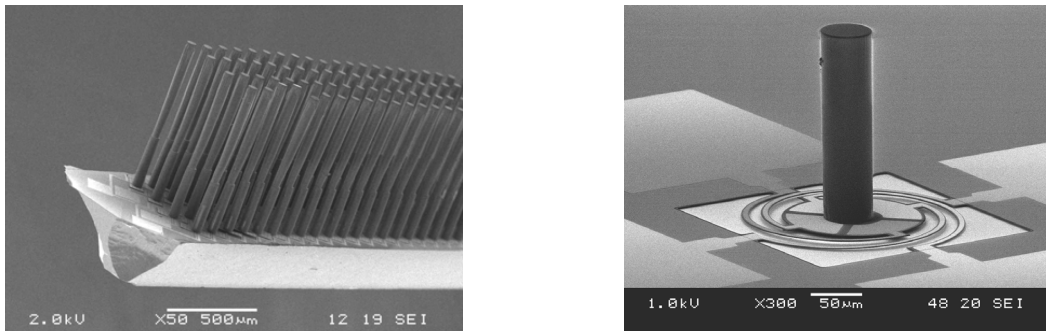


Fig. 1-2: SEM images of a SU-8 based artificial hair sensor and a high density array of hair sensors

Despite the successful bio-mimicking, several behavioral characteristics of the cercal hairs in an array - like viscous coupling, still remain unknown or less understood by scientists. Some seminal research has been carried out on the subject of viscous coupling effects between the actual cercal hairs found in nature [9,10]. In parallel to these biological studies on viscous coupling, characterization of similar effects between the artificial hair sensors would make a significant contribution to the scientific research. With the major advantage of having manual control over the operation of the artificial sensory hairs, a wide range of experimental characterizations is now possible.

Making use of the latest developments in the artificial hair sensor research, several artificial hair sensors are arranged in various patterns on a dedicated experimentation platform. These patterns are used to characterize the viscous coupling effects between the hair sensors, if present, by measuring the deflection of the hair sensor membranes using an optical, non-contact measurement method, i.e. laser vibrometry.

1.2 Original project description

The aim of this work is to study the presence of viscous coupling between hair sensors currently in development in the Custom Intelligent Life Inspired Array (Cilia) project. Initially, the parameters which play a major role in viscous coupling are identified. Using this knowledge, an experimentation platform design is made. This platform enables experiments to characterize the viscous coupling between the hair sensors, if present. The design of the experimentation platform is realized and different characterization experiments are carried out. Experimental findings are compared to model/numerical predictions, if necessary derived by our partners in the Cilia project.

2 Theory

2.1 Introduction

The flow receptive hairs found on arthropods have been a subject of scientific research for many years. Part of this research is focused on the viscosity mediated coupling between these flow sensitive receptors [9,10]. Scientists have been successful in mimicking these flow receptive hairs using MEMS technology to create artificial hair sensors. The presence of viscous coupling between these artificial hair sensors is yet unknown. Studying the coupling between the MEMS sensors may also benefit the research on the flow receptive hairs found on arthropods and other animals.

2.2 Viscous coupling

Many terrestrial arthropods like crickets, spiders, etc. use filiform hairs as receptors to detect the direction and magnitude of air-flows. The behavior of these systems has been studied extensively [3,11]. Arachnids and insects are able to detect small perturbations in their surrounding air by using a fine system of motion receptors. The perturbations in the flow are picked up by hairs of different lengths having different directions of sensitivity. The receptive hairs on these animals are often arranged in dense arrays or groups with spacing's of tens to hundreds of micrometers between them. Being this close together can result in viscous coupling effects between the hairs in an array. Having arrays of hairs with different lengths, increases the range of frequencies the system is able to detect. Arrays, containing receptive hairs having their sensitivity in many different directions, increase the directional sensitivity of the flow receptive system. The absolute sensitivity of the system is also increased by using arrays of receptors.

Viscous coupling between two objects depends on different quantities. The unknown relation between different quantities playing a role in a physical phenomenon, can be investigated by dimensional analysis. This type of analysis is used to identify the major parameters in viscous coupling and the relation between them. A simple model of two straight cylindrical rods represents two hair sensors separated by a distance S [Fig. 2-1].

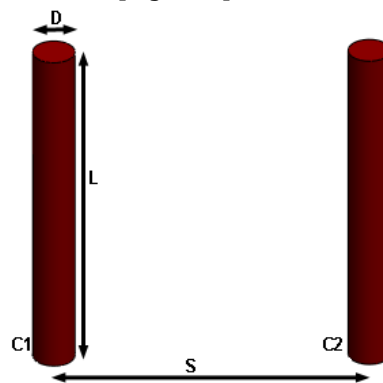


Fig. 2-1: Simple model to derive the dominant parameters in viscous coupling and the relation between them. Two straight cylinders having length L , diameter D and a separation S between the two.

In this case, viscous coupling is described as the force F on cylinder C2 as a result of the motion of cylinder C1. This force is dependent on different geometric and physical quantities. The geometry of the model is specified by the length L , the diameter D of the two cylinders and the their spacing S . The medium surrounding the cylinders affects the coupling between them. The dynamic viscosity μ and the density ρ of the medium can affect the response of C2 while C1 is moving. The motion of C1 is represented by amplitude A and frequency ω . The quantities are expressed in units, written in terms of basic SI-units [Tab. 2-1].

Quantity	Description	Unit
P	Density medium	kg·m ⁻³
D	Diameter hair	m
L	Length hair	m
S	Separation sensors	m
μ	Dynamic viscosity	kg·m ⁻¹ ·s ⁻¹
Ω	Frequency	s ⁻¹
A	Amplitude	m

Tab. 2-1: Different quantities with their respective SI units

The force on cylinder C2 as a result of the motion of cylinder C1 is written as the multiplication of all quantities raised to an unknown power with each other.

$$F = \rho^a \cdot D^b \cdot L^c \cdot S^d \cdot \mu^e \cdot \omega^f \cdot A^g \quad (1)$$

Expressing the quantities in their respective SI units and re-arranging the unknown powers give:

$$kg \cdot m \cdot s^{-2} = kg^{a+e} \cdot m^{-3a+b+c+d-e+g} \cdot s^{-e-f} \quad (2)$$

The powers of the separate units on both side need to be equal, this results in three equations with seven unknown variables.

$$a + e = 1 \quad (3)$$

$$-3a + b + c + d - e + g = 1 \quad (4)$$

$$-e - f = -2 \quad (5)$$

Analytically there is no solution for this but by inspecting the model and making some careful assumptions a solution is possible. For instance at low velocities, the effect on cylinder C2 is expected to be linear with the velocity of cylinder C1, hence f and g are both equal to one. It is also expected that the force scales with the length of the two cylinders, hence c is also equal to one. Putting the value for f in equation (2) results in the force having a linear dependence on the viscosity of the medium. Equation (3) then states that the force on cylinder C2 is independent of the density ρ of the medium. A single equation containing two unknown variables is left.

$$b + d = 0 \quad (6)$$

These two variables represent the diameter and separation between the two cylinders. When the distance between the two cylinders increases, it is expected that the coupling between the two is less. The force on cylinder C2 is than proportional to the reciprocal of the distance between the two hence equation (6) states that it is proportional to the diameter of the cylinder. With the velocity $A\omega$ written as V the relation between the force on cylinder C2 as a result of the motion of cylinder C1 is then written as:

$$F \propto \frac{LD}{s} \mu V \quad (7)$$

2.3 Previous research on viscous coupling

In the past research on the subject of viscous coupling between flow receptor hairs has been focused on spiders [9] and crickets [10]. The possibility of viscous coupling between pairs of hairs on the spider '*Cupiennius salei*' was first remarked by Humphrey et al. [12].

Bathellier et al. [9] studied viscous coupling by conducting experiments on a pair of trichobothria on the leg of the spider '*Cupiennius salei*'. A coupling coefficient κ introduced by Bathellier, relates the deflection angle of a hair when another hair is present to the angle of deflection when the other hair is absent. When the deflection of a hair in the presence of a second hair is represented by ϕ , and the deflection of this hair in case the other hair is absent is represented by ϕ_{ref} , the coupling coefficient for hair i is written as:

$$\kappa_i = \frac{(\phi_{ref} - \phi_i)}{\phi_{ref}} \quad (8)$$

This coupling coefficient depends on hair properties like the effective moment of inertia I_{eff} , the effective damping constant R_{eff} and the torsion restoring constant S . In general the coupling coefficient is expected to be related to several parameters, like:

$$\kappa_i = g_i \left(\frac{s}{d}, \lambda, G_{Ri}, G_{Si}, G_{Rj}, G_{Sj}, \frac{L_i}{L_j} \right) \quad (9)$$

Where s is the spacing between the hairs, d is the diameter of the hairs and L is the hair length. The subscripts i and j denote the hair number and for G_R and G_S holds [12]:

$$G_R = \frac{R_{eff}}{I} \omega \quad (10)$$

$$G_S = \frac{S}{I_{eff}} \omega^2 \quad (11)$$

The parameter λ is given by Stokes and is necessary to characterize the dynamics of the flow and the total force on a cylinder [13]:

$$\lambda = \frac{d}{2} \sqrt{\frac{2\pi f}{\nu}} \quad (12)$$

In the experiments on the leg of the spider by Bathellier et al. , the amplitude of the flow velocity was kept below 1 m/s. The biologically relevant air-flows experienced by the spider "*Cupiennius salei*" are usually well below this value [14]. The animal was observed using a camera setup with a measurement resolution of 5 μ m. All experiments focused on two neighboring hairs on the leg. One hair (H1) was free to move under the viscous action of the airflow passing over the leg which can include any disturbances resulting from manipulating a second neighboring hair (H2). The results of a baseline experiment in which H1 is free to move without the presence of other hairs is used as reference. In the other experiments a second hair H2 was present. Either this hair was free to move, it was kept at its equilibrium position or it was driven by a mechanical oscillator. In all cases the amplitude and phase of both hairs were recorded.

Bathellier et al., conducted these experiments on pairs of hairs having spacings S of 250 μ m and 350 μ m. With hair diameters d close to 7-8 μ m, their relative spacing (S/d) is rather large. Other hairs in the vicinity have been removed. Only small perturbations in the motion of H1 were measured when H2 was immobilized. Small deflections of H1 were also observed in the case where H2 was driven by a mechanical oscillator, however no exact data was retrieved.

These experiments were repeated on another pair of hairs with a spacing of 180 μ m. With hair lengths of H1=650 μ m and H2=750 μ m, $S/d \approx 22.5$. The results of these experiments indicated that there was little natural coupling between the hairs (H1 and H2 can move freely). However in case of an immobilized hair H2 or when H2 was driven by the oscillator, coupling was perceptible. The results of the experiment in which H2 is immobilized also indicated that the airflow can be significantly affected by the immobilized hair, effects up to a distance of 400 μ m were recorded.

The interaction between receptor hairs on crickets was studied by Cummins et al. [10]. They developed a model based on the dense arrays of hairs on the cercus of a cricket. These hairs are much denser packed compared to similar hairs on a spider and not ordered with respect to their length [11]. Cummins extended models studied by others [9,11,12] by enabling the calculation of the mutual interaction between hairs. Cummins modeled the cercus of a cricket by a cylindrical section, 700 μm in length having an angular extend of $\pi/2$. For frequencies of 50 Hz, 100 Hz and 200 Hz, the model is used in a simulator to calculate the coupling coefficient κ for pairs of hairs having lengths of 700 μm and 1400 μm . The results of the numerical simulations in their figure 6 [[10] show that the effect of a second free moving hair on the reference hair, decreases with frequency. Bathellier measured no significant coupling between two free moving hairs of equal length at frequencies between 50-200 Hz. The results of the simulations by Cummins et al. however, show significant coupling between free moving hairs across all tested distances. In case of a stationary second hair, the results of Cummins shows a gradual decrease of the coupling coefficient κ up to $S/d = 50$ where the result of Bathellier shows a sharp decrease of κ . Cummins also studied a patch of cercus with seven hairs having lengths between 100 μm and 400 μm . The response of each hair in the group is compared to its individual response without presence of other hairs. Results of simulations on this patch of cercus indicated that hairs of intermediate length are most affected by the presence of other hairs, amplitude changes of 75%-100% are experienced in this range, where shorter and longer hairs experienced amplitude changes of 59% to 70%.

Biologically, free moving hairs are most relevant, so knowing about viscous coupling in this case is essential to understand the operation of these receptor hairs. Although the mechano-receptors on arthropods use hairs diameters smaller than used on the hair sensors, the viscous coupling research by Bathellier and Cummins provides a base for similar research on the bio-inspired hair sensors.

2.4 Hair sensors

A new generation of hair based flow sensors is used for the viscous coupling research. The principle of operation of these sensors is based on a pair of differential capacitors. A differential capacitor setup is a set of two parallel plate capacitors equal in size using only three electrodes, so one of the electrodes is shared between the two capacitances. The hair sensors are fabricated in a surface micromachining process. A conductive silicon substrate is used as the common electrode in the differential capacitor setup. Above this substrate a square membrane is suspended by two rectangular torsion beams [Fig. 2-2]. This membrane is able to tilt about the axis of these torsion beams. On top of the membrane two electrodes are located, one on each side of the axis of rotation. Together with the substrate these electrodes make up the differential capacitor setup used for electronic sensor readout. On top of the membrane, in the centre, a cylindrical hair is present. A passing airflow causes a drag-force on this hair. This drag-force results in a drag-torque on the membrane causing it to tilt. Tilting the membrane changes the capacitance of the two capacitors. Dedicated electronics are available to measure this by feeding two out of phase sinusoidal signals to the two electrodes on the membrane. These signals are coupled to the common electrode, which is the output of the sensor, by the two capacitors. Tilting the membrane will couple one of the two sinusoidal signals stronger than the other, hence the output is related to the velocity and direction of the flow.

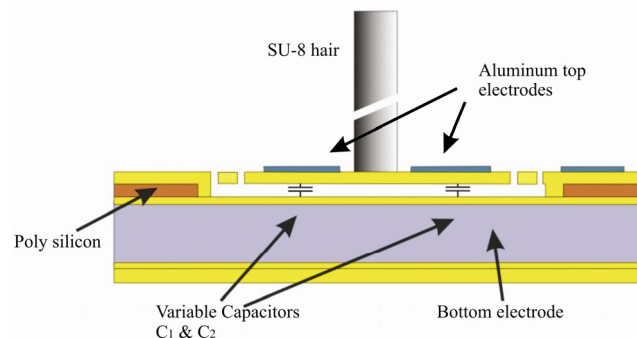


Fig. 2-2: Schematic sensor overview, a hair on top of a membrane suspended by torsion beams. Two differential capacitors C_1 and C_2 are used for electronic readout. The passing flow induces a drag-force on the hair, the resulting drag-torque tilts the membrane, and hence the capacitance of C_1 and C_2 changes differentially.

2.5 Hair sensor model

Different aspects of the hair sensors can be mathematically analyzed, like the motion of the hair and membrane of the sensor. The hairs on the cricket are modeled by an inverted pendulum, which is a second order mechanical system [12,15]. This model also fits the MEMS hair sensors. The oscillating hair is modeled as a ridged shaft having length l_0 , suspended at the bottom by a torsion stiffness K [Fig. 2-3]. The friction in the suspension is represented by a damping constant R and the drag torque $T_{drag}(t)$ results from the friction induced drag-force by the air flow along the hair shaft. For a rigid hair which is oscillating about a fixed axis of rotation, the conservation of angular momentum states that the rate of change of angular momentum of this hair is equal to the total torque acting on the hair [16].

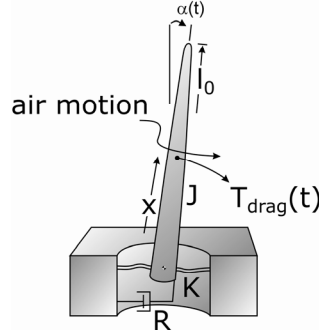


Fig. 2-3: Inverted pendulum as a model for the cricket hairs and the MEMS sensors

Besides the drag-torque acting on the hair shaft is, a torque associated with the added (or virtual) mass of the air is acting on the hair. When the hair accelerates, at least some air needs to be accelerated along with it [16]. Writing this torque as $T_{VM}(t)$, the torque applied by the stiffness K as $T_S(t)$ and the torque $T_R(t)$ due to the damping R , the rate of change of the angular momentum (L) of the hair is written as:

$$\frac{dL(t)}{dt} = I \frac{d^2\alpha}{dt^2} = T_{Drag}(t) + T_{VM}(t) - T_R(t) - T_S(t) \quad (13)$$

With I the moment of inertia of the hair. The torque $T_S(t)$ applied by stiffness K and the damping torque $T_R(t)$ always act opposite to the direction of deflection of the hair. The restoring torque $T_S(t)$ is proportional to the angular deflection α by the torsion stiffness K .

$$T_S(t) = K \cdot \alpha(t) \quad (14)$$

The total damping torque $T_R(t)$ is proportional to the angular velocity of the hair.

$$T_R(t) = (R + R_{VM}) \frac{d\alpha}{dt} \quad (15)$$

Specific relations for the damping R_{vm} due the resistance between the added mass and the surrounding air, and the damping R in the suspension of the hair are presented by Shimozawa [11,16].

$$R = 2.88 \cdot 10^{-14} \left(\frac{L_{hair}}{1000} \right)^{2.77} \quad (16)$$

$$R_{VM} = 4\pi\mu G \left(\frac{L_{hair}^3}{3} \right) \quad (17)$$

With μ the dynamic viscosity of air and G , a dimensionless parameter introduced by Stokes [13]. Stokes stated that for a dimensionless parameter s :

$$s = \frac{d}{4} \left(\frac{2\pi f}{\nu} \right)^{\frac{1}{2}} \quad (18)$$

Such that $s \ll 1$, G is equal to:

$$G = \frac{-(x+\ln(s))}{(x+\ln(s))^2 + (\frac{\pi}{4})^2} \quad (19)$$

The drag torque $T_{Drag}(t)$ is written as the integral of the drag-force $F_D(x,t)$ along the hair shaft

$$T_{Drag}(t) = \int_0^{l_0} F_D(x,t) x dx \quad (20)$$

A similar approach is followed for the added mass torque, which is written as the integral of the added mass force per unit length acting along the hair shaft.

$$T_{VM}(t) = \int_0^{l_0} F_{VM}(x,t) x dx \quad (21)$$

In a fluid oscillating at frequency f , having a flow velocity of $V_F(x,t)$, the drag force $F_D(x,t)$ and the force $F_{vm}(t)$ on a cylindrical piece of hair at height x are written as [13]:

$$F_D(x,t) = 4\pi\mu G V_F(x,t) \quad (22)$$

$$F_{VM}(x,t) = \frac{-\pi\mu G V_F(x,t)}{2g \cdot f} + \pi\rho \left(\frac{d}{2}\right)^2 V_F(x,t) \quad (23)$$

Herein are μ and ν the dynamic and kinematic viscosity of air respectively and d is the diameter of the hair. The dimensionless parameters G is already introduced in (19). This completes the description of the model of the hair sensor, the velocity $V_F(x,t)$ is discussed separately in the next section.

2.6 Oscillating flow

An object present in an air-flow affects the flow pattern. The flow near the object, is dependent on the size and shape of the object as well as flow properties like velocity and medium viscosity. Specifically at the surface of an object it is interesting to know what is going on.

The hair sensors are made in a surface micromachining process which means the sensors are on top of a substrate. Near a surface, the velocity of a fluid is slowed down by the shearing action of viscous forces. Viscosity affects the velocity of a fluid in motion with respect to a surface. The fluid layer near the surface in which this shearing occurs is referred to as the boundary layer. The thickness of this boundary layer depends on the fluid viscosity, the velocity of the flow and the distance to the leading edge of the plate. For a steady flow over a thin plate with a sharp leading edge holds that the boundary layer thickness as a function of the distance x to the leading edge is approximated by [17]:

$$\delta \approx 5 \sqrt{\frac{\nu x}{U_\infty}} \quad (24)$$

In this expression ν is the kinematic viscosity of the medium and U_∞ is the free stream velocity of the fluid which is the velocity of the fluid at infinite distance away from the surface.

In case of an oscillating flow, the boundary layer thickness is uniform over the entire surface, it is independent of the distance to a leading edge. It is however related to the frequency of the oscillating flow and the viscosity of the medium [15,17]. The thickness of the boundary layer in case of a flow oscillating parallel to a surface is written as:

$$\delta_o = \sqrt{\frac{\nu}{\pi f}} \quad (25)$$

The kinematic viscosity of air at a temperature of 20 °C is equal to $1.5 \cdot 10^{-5} \text{ m}^2\text{s}^{-1}$. The boundary layer thickness under these conditions is displayed in a graph for frequencies between 10 Hz and 10 kHz [Fig. 2-4].

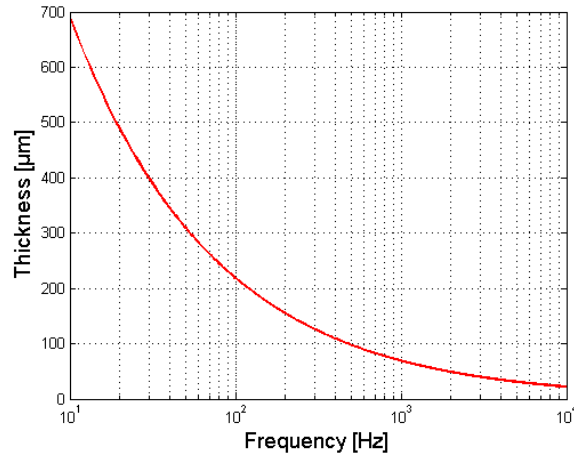


Fig. 2-4: Boundary layer thickness of an oscillating airflow (20 °C $\nu=1.5 \cdot 10^{-5} \text{ m}^2\text{s}^{-1}$) on an infinite flat surface for different flow frequencies.

At low frequencies the boundary layer is quite thick compared to the length of the sensor hairs ($\sim 1 \text{ mm}$). Near a surface, in the boundary layer the velocity of the airflow is lower. So at low frequencies, the reduced velocity in the boundary layer affects the response of the sensors. The velocity of an oscillating flow $u_z(t)$ at a height z above an infinite flat surface, when the air moves parallel to this surface, is given by [13,15].

$$u_z(t) = U_0 \sin(2\pi ft) - U_0 e^{-\beta z} \sin(2\pi ft - \beta z) \quad (26)$$

With U_0 the magnitude of the flow oscillating at frequency f and β the reciprocal of (25), the boundary layer thickness for an oscillating:

$$\beta = \sqrt{\frac{\pi f}{\nu}} \quad (27)$$

In this expression, f is the frequency of the flow and ν is the kinematic viscosity of air. Writing $U_z(t)$ as a complex expression, the modulus and phase of the flow velocity are calculated:

$$U_z(t) = \text{Re}\left(\left(1 - e^{-\beta z} e^{-j(\beta z)}\right) U_0 e^{j\left(2\pi ft - \frac{\pi}{2}\right)}\right) \quad (28)$$

Writing the part of equation (28) between brackets as the sum of a real and imaginary part, $U_z(t)$ is written as

$$u_z(t) = U_z \sin(2\pi ft + \zeta_z) \quad (29)$$

With modulus U_z and phase ζ_z equal to:

$$U_z = U_0 \sqrt{1 + e^{-2\beta z} - 2e^{-\beta z} \cos(\beta z)} \quad (30)$$

$$\zeta_z = \tan^{-1}\left(\frac{e^{-\beta z} \sin(\beta z)}{1 - e^{-\beta z} \cos(\beta z)}\right) \quad (31)$$

The modulus and phase of the flow velocity depend on the height z above the surface and the reciprocal of the boundary layer thickness β which is defined by (27).

For an oscillating airflow at room temperature (20 °C, $\nu=1.5 \cdot 10^{-5} \text{ m}^2\text{s}^{-1}$) the modulus and phase of the flow are displayed for several frequencies [Fig. 2-5]. No actual velocity values are displayed, since the flow profile is scaled with U_0 .

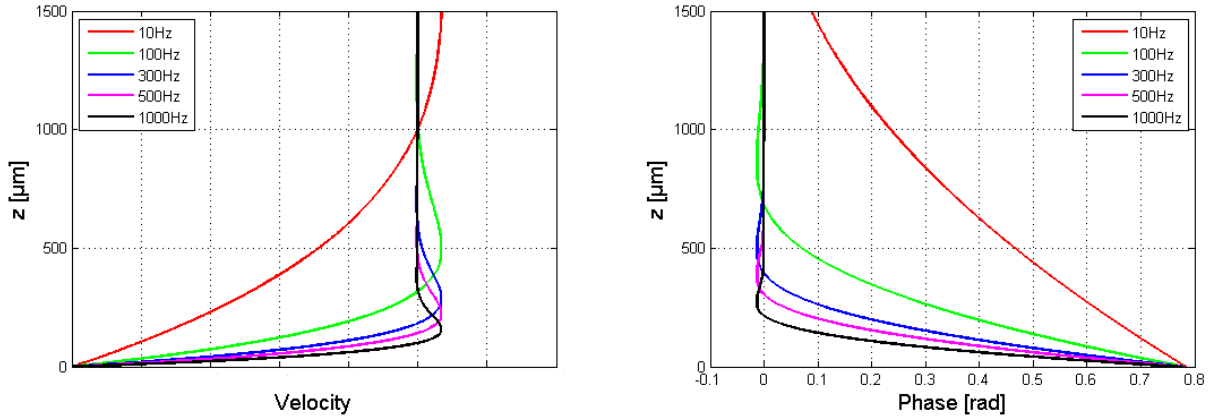


Fig. 2-5: Left: velocity profile of an oscillating airflow (20 °C) at height z at different flow frequencies. Right: phase of an oscillating air flow (20 °C) at height z at different flow frequencies.

The flow profiles in [Fig. 2-5 Left] clearly indicate the frequency dependency of the boundary layer thickness, the damping of the fluid layer near the surface is also clear. For the frequencies displayed in the graphs [Fig. 2-5 Right] the phase of the flow is advanced by about $\pi/4$ (rad) compared to the free stream velocity of the flow.

The flow near a surface is slowed down by the shearing action of the viscous forces. The relation between the inertial force and the viscous force in a fluid is described by the Reynolds number. This dimensionless number is defined as:

$$\text{Re} = \frac{\rho V D}{\mu} = \frac{V D}{\nu} = \frac{Q D}{\nu A} \quad (32)$$

In this expression, ρ is the density of the medium, V is the flow velocity and D is the characteristic length in the system. The dynamic viscosity is represented by μ and the kinematic viscosity by ν . The flow velocity V is also expressed as volume flow Q through area A . At a high Reynolds number, flow tends to become more turbulent. At low Reynolds number, the flow is more laminar. For the cricket, which has hair diameters between $1\mu\text{m}$ and $9\mu\text{m}$ [3], the Reynolds number is typically very low. Crickets are able to detect airflows as low as 0.03 mm/s [6] which means Reynolds numbers down to $1.71 \cdot 10^{-5}$.

2.7 Capacitance model

The electric sensing principle of the hair sensors is based on capacitive read-out, the flow velocity of the air is converted into a capacitance. As discussed in section 2.4 this is accomplished by a differential capacitance implemented as two electrodes on top of a membrane suspended above a common electrode. The membrane and the common electrode are separated by an air-gap. The differential change in the capacitance is realized by tilting the membrane, making the capacitance dependent on the tilt angle α .

The deflection $d(t)$ of the membrane is related to the tilt angle of tilt $\alpha(t)$ and the distance to the axis of rotation b by a simple goniometric expression:

$$d(t) = b \cdot \sin(\alpha(t)) \quad (33)$$

The capacitance C of a static parallel plate capacitor is related to the distance d between the plates and the permittivity $\epsilon_0 \epsilon_r$ of the material between the plates according to:

$$C = \frac{\varepsilon_0 \varepsilon_r A}{d} \quad (34)$$

In this expression ε_0 is the permittivity of vacuum, ε_r is the relative permittivity of the material between the two electrodes and A is the electrode area. The MEMS hair sensors use a differential capacitor setup for electronic readout. The drag torque on the hair forces the membrane to tilt and so making the geometry of the capacitor dependent on α . When the membrane tilts, the plate area of the two capacitors reduces. Tilting the membrane also change the thickness of the air-gap and the effective thickness of the membrane. Besides being dependent on α , the size of the air-gap depends also on the distance to the axis of rotation. The effective thickness of the membrane however depends only on the tilt angle α . The change in the effective thickness of the membrane is equal for both capacitors, so it does not contribute a differential change in capacitance. Since the capacitance is proportional to the reciprocal of the distance between the electrodes, the absolute change in capacitance is different for each of the two capacitors. The contribution of the air-gap to the total capacitance of the device is written as an integral over the entire electrode area.

$$C(\alpha) = \int_{-L}^L \frac{\varepsilon_0 \varepsilon_{air} \cdot w \cdot \cos(\alpha)}{(g - x \cdot \sin(\alpha))} dx \quad (35)$$

In this expression, w is the width of the electrodes, α is the tilt angle, g is the thickness of the air-gap at equilibrium, ε_0 is the permittivity of vacuum, ε_{air} is the relative permittivity of air and L is the distance from the axis of rotation to the edge of the membrane [Fig. 2-6].

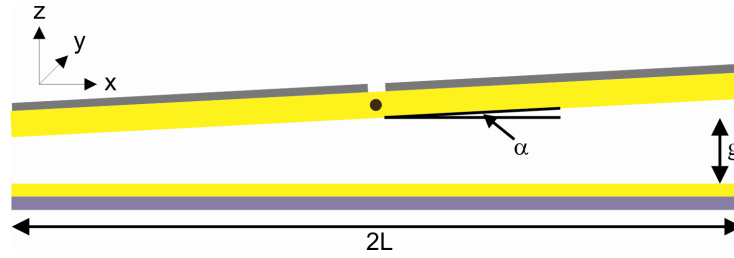


Fig. 2-6: Tilting sensor showing a the tilt angle α and the initial air-gap g and the total length $2L$ of the membrane.

The nominator in equation (35) is substituted by u ,

$$u = g - x \sin(\alpha) \quad (36)$$

$$dx = \frac{-du}{\sin(\alpha)} \quad (37)$$

Now the expression in (35) is rewritten and using the fact that the relative permittivity of air is equal to one this results in:

$$C(\alpha) = \varepsilon_0 w \cos(\alpha) \int_{-L}^L \frac{1}{(g - x \cdot \sin(\alpha))} \cdot \frac{-d(g - x \cdot \sin(\alpha))}{\sin(\alpha)} \quad (38)$$

$$C(\alpha) = \frac{-\varepsilon_0 w \cos(\alpha)}{\sin(\alpha)} \int_{g+L\sin(\alpha)}^{g-L\sin(\alpha)} \frac{du}{u} = \frac{\varepsilon_0 w \cos(\alpha)}{\sin(\alpha)} \cdot \ln \left(\frac{g + L \cdot \sin(\alpha)}{g - L \cdot \sin(\alpha)} \right) \quad (39)$$

Because in the MEMS sensors the tilting angles experienced are very small, the expression in (39) is rewritten as:

$$C(\alpha) = \lim_{\alpha \rightarrow 0} \frac{\varepsilon_0 w \cos(\alpha)}{\sin(\alpha)} \cdot \ln\left(\frac{g+L\sin(\alpha)}{g-L\sin(\alpha)}\right) = \frac{\varepsilon_0 W}{\alpha} \left[\lim_{\alpha \rightarrow 0} \ln\left(\frac{g+L\sin(\alpha)}{g-L\sin(\alpha)}\right) \right] \quad (40)$$

The term between the square brackets can be represented by a Taylor series calculated around alpha is zero. Replacing the term between the square bracket by a fifth order Taylor series and rearranging the equation results in a Taylor series of the total capacitance of:

$$C(\alpha) = \frac{2\varepsilon_0 w L}{g} \left(1 + \frac{1}{6} \left(\frac{2L^2}{g^2} - 1 \right) \alpha^2 + \frac{1}{120} \left(\frac{24L^4}{g^4} - \frac{20L^2}{g^2} + 1 \right) \alpha^4 \right) \quad (41)$$

Electronic readout of the two sensor capacitors is realized by supplying a sinusoidal signal to each of the two electrodes on the membrane. By using two equal but 180° out of phase sine waves, both absolute and directional sensitivity is obtained [Fig. 2-7]. When the device is in equilibrium, the capacitance of the two sensor capacitors is equal. In that case, both sine waves are coupled equally to the common electrode which results in a zero output signal. When the membrane tilts, the geometry of the two capacitors changes, The gap between the common electrode and the electrode on the membrane increases on one side while it decreases on the other, consequently realizing a differential change in capacitance. This difference in capacitance results in a non-zero output signal. The amplitude of this signal is related to the tilt angle which in turn is related to the flow velocity. The relative phase of the output is related to the tilt direction and hence the direction of the flow. The output signal of the sensor is amplified by a charge amplifier, demodulated and processed further by dedicated electronics.

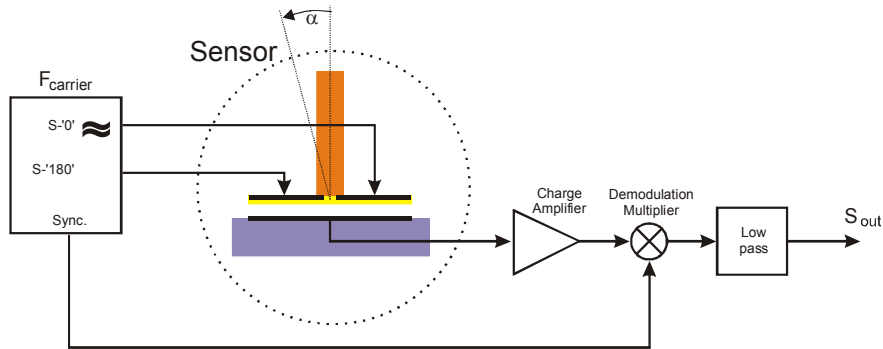


Fig. 2-7: Schematic sensor readout, using dedicated electronics. Two carrier signals ($\Delta\phi = 180^\circ$) are supplied to the two top electrodes. The output signal at the common electrode is supplied to a charge amplifier and processed further by a demodulator before being filtered.

Since the difference in capacitance of the two sensor capacitors is the quantity depending on the velocity of the flow, the two sides of the sensor need separate attention.

Using equation (39) the capacitances of the two halves of the sensor are written as separate integrals:

$$C(\alpha)_{left} = \int_{-L}^0 \frac{\varepsilon_0 w \cos(\alpha)}{(g - x \sin(\alpha))} dx = \frac{-\varepsilon_0 w \cos(\alpha)}{\sin(\alpha)} \int_g^{g-L\sin(\alpha)} \frac{1}{u} du = \frac{-\varepsilon_0 w \cos(\alpha)}{\sin(\alpha)} \ln\left(1 - \frac{L}{g} \sin(\alpha)\right) \quad (42)$$

$$C(\alpha)_{right} = \int_0^L \frac{\varepsilon_0 w \cos(\alpha)}{(g - x \sin(\alpha))} dx = \frac{-\varepsilon_0 w \cos(\alpha)}{\sin(\alpha)} \int_{g+L\sin(\alpha)}^g \frac{1}{u} du = \frac{\varepsilon_0 w \cos(\alpha)}{\sin(\alpha)} \ln\left(1 + \frac{L}{g} \sin(\alpha)\right) \quad (43)$$

The experienced angles of tilt are very small. So for small values of α , expressions (42) and (43) are written as:

$$C(\alpha)_{left} = \lim_{\alpha \rightarrow 0} \frac{-\varepsilon_0 w \cos(\alpha)}{\sin(\alpha)} \ln\left(1 - \frac{L}{g} \sin(\alpha)\right) = \frac{-\varepsilon_0 w}{\alpha} \cdot \lim_{\alpha \rightarrow 0} \ln\left(1 - \frac{L}{g} \sin(\alpha)\right) \quad (44)$$

$$C(\alpha)_{right} = \lim_{\alpha \rightarrow 0} \frac{\varepsilon_0 w \cos(\alpha)}{\sin(\alpha)} \ln\left(1 + \frac{L}{g} \sin(\alpha)\right) = \frac{\varepsilon_0 w}{\alpha} \cdot \lim_{\alpha \rightarrow 0} \ln\left(1 + \frac{L}{g} \sin(\alpha)\right) \quad (45)$$

Now a Taylor series for the term between brackets in (44) and (45) for alpha is zero is calculated:

$$C(\alpha)_{left} = \frac{\varepsilon_0 w L}{g} \left(1 + \frac{L}{2g} \alpha + \frac{1}{6} \left(\frac{2L^3}{g^3} - 1\right) \alpha^2 + \frac{1}{12} \left(\frac{3L^3}{g^3} - \frac{2L}{g}\right) \alpha^3 + \frac{1}{120} \left(\frac{24L^4}{g^4} - \frac{20L^2}{g^2} + 1\right) \alpha^4\right) \quad (46)$$

$$C(\alpha)_{right} = \frac{\varepsilon_0 w L}{g} \left(1 - \frac{L}{2g} \alpha + \frac{1}{6} \left(\frac{2L^3}{g^3} - 1\right) \alpha^2 - \frac{1}{12} \left(\frac{3L^3}{g^3} - \frac{2L}{g}\right) \alpha^3 + \frac{1}{120} \left(\frac{24L^4}{g^4} - \frac{20L^2}{g^2} + 1\right) \alpha^4\right) \quad (47)$$

Adding the capacitance of the two parts in (46) and (47) results in the total capacitance of the sensor, hence the result is equal to (41).

$$C(\alpha)_{left} + C(\alpha)_{right} = \frac{2\varepsilon_0 w L}{g} \left(1 + \frac{1}{6} \left(\frac{2L^2}{g^2} - 1\right) \alpha^2 + \frac{1}{120} \left(\frac{24L^4}{g^4} - \frac{20L^2}{g^2} + 1\right) \alpha^4\right) \quad (48)$$

The sensor output signal results from a difference in capacitance between the two capacitors on the sensor. Subtracting the two capacitances in (46) and (47) results in:

$$C(\alpha)_{left} - C(\alpha)_{right} = \frac{-\varepsilon_0 w}{\alpha} \left(-\frac{L^2}{g^2} \alpha^2 - \frac{1}{6} \left(\frac{-2L^2}{g^2} + \frac{3L^4}{g^4}\right) \alpha^4\right) = \frac{\varepsilon_0 w L^2}{g^2} \alpha + \frac{\varepsilon_0 w L^2}{g^2} \left(\frac{L^2}{2g^2} - \frac{1}{3}\right) \alpha^3 \quad (49)$$

The equations expressing the capacitance of the two sensor capacitors are displayed in a single diagram which visualizes, if and where the Taylor representation starts to deviate from the actual model [Fig. 2-8 Left]. Also the difference between the two capacitors, hence the difference between (46) and (47) as well as the Taylor series representing this difference (49) are displayed in a figure to visualize the deviation of the Taylor series.

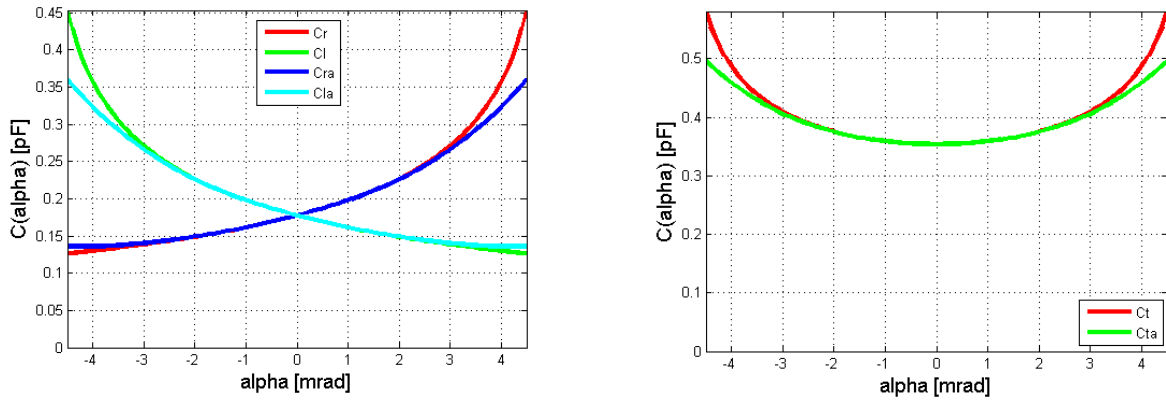


Fig. 2-8: Left: capacitance of the two capacitors on the sensor in equilibrium as a function of alpha (electrode area $L=100 \mu\text{m}$ $w=100 \mu\text{m}$). C_r and C_l represent the right and left capacitance as represented in equations (42) and (43). The Taylor series around alpha is zero for the two capacitors, expressions (46) and (47), are displayed as C_{ra} and C_{la} . Right: differential capacitance as function of alpha, the difference between (42) and (43) is represented as C_t while its Taylor representative around alpha is zero (49), is displayed as C_{ta} .

As explained, for electronic readout of the hair sensor, the two electrodes on the membrane are used as inputs while the common electrode is used as the output. An equivalent circuit diagram is used to calculate the output signal [Fig. 2-9]. This figure only shows the differential part of the capacitance, obviously there is also a common change in capacitance as a result of the reduction in electrode area. Parasitic capacitors and resistors are also part of the real system, for now the common and parasitic elements are neglected.

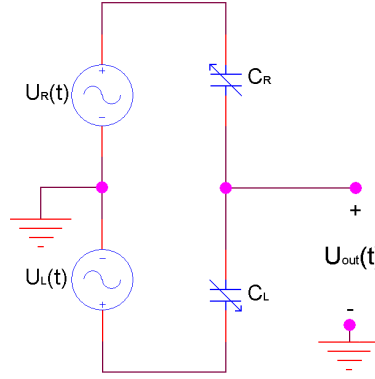


Fig. 2-9: Electronic schematic of the hair sensor readout with the two alpha dependent differentia capacitors coupling the two 180° out of input signals to the common electrode.

The two capacitors $C_L(\alpha)$ and $C_R(\alpha)$ are each supplied with cosine signal. The signals supplied to the two capacitors are 180° out of phase:

$$U_L(t) = U_0 \cos(\omega t) \quad (50)$$

$$U_R(t) = -U_0 \cos(\omega t) \quad (51)$$

To calculate the output signal $U_{out}(t)$, the principle of superposition is applied. Adding the contributions of each of the two signal sources $U_R(t)$ and $U_L(t)$ results in an output signal of:

$$U_{out}(t) = U_0 \cos(\omega t) \frac{C(\alpha)_{left}}{C(\alpha)_{left} + C(\alpha)_{right}} - U_0 \cos(\omega t) \frac{C(\alpha)_{right}}{C(\alpha)_{left} + C(\alpha)_{right}} = U_0 \cos(\omega t) \frac{C(\alpha)_{left} - C(\alpha)_{right}}{C(\alpha)_{left} + C(\alpha)_{right}} \quad (52)$$

Now substituting equations (42) and (43) in (52) results in an output signal of:

$$U_0 \cos(\omega t) \cdot \frac{\ln\left(\frac{g-L\sin(\alpha)}{g}\right) + \ln\left(\frac{g-L\sin(\alpha)}{g}\right)}{\ln\left(\frac{g-L\sin(\alpha)}{g}\right) - \ln\left(\frac{g+L\sin(\alpha)}{g}\right)} = U_0 \cos(\omega t) \cdot \frac{\ln\left(\frac{g^2 - L^2 \sin^2(\alpha)}{g^2}\right)}{\ln\left(\frac{g-L\sin(\alpha)}{g+L\sin(\alpha)}\right)} \quad (53)$$

Using the Taylor series (48) and (49), the Taylor series for the output signal for small angles evaluates to:

$$U_{out_{Taylor}}(t) = U_0 \cos(\omega t) \cdot \frac{\frac{L}{g} \left(\alpha + \frac{L}{g} \left(\frac{L^2}{2g^2} - \frac{1}{3} \right) \alpha^3 \right)}{2 \left(1 + \frac{1}{6} \left(\frac{2L^2}{g^2} - 1 \right) \alpha^2 + \frac{1}{120} \left(\frac{24L^4}{g^4} - \frac{20L^2}{g^2} + 1 \right) \alpha^4 \right)} \quad (54)$$

Optimizing the output signal is a challenge with several tradeoffs. The output Taylor series in (54) indicates a dependency of the output on the ratio of the length L and air-gap size g . Decreasing the air-gap increases the capacitance of two sensor capacitors which increases the relative change in capacitance for a given angle α resulting in a larger output signal. The downside of decreasing the air-gap is that it reduces the tilting range of the membrane [Fig. 2-10]. Increasing the length L has a similar effect, it increases the capacitance and relative capacitive change for a given α , again at the cost of lowering the tilting range of the sensor [Fig. 2-10]. Reducing the tilting range of the sensor without changing other parameters, reduces the velocity range in which the sensor can operate. As explained in section 2.2 the separation S between the sensors is one of the parameters in viscous coupling. Scaling the length L of the sensors with δ results in scaling the separation S with 2δ . Increasing the output for a given flow velocity and membrane geometry is also possible by reducing the torsion stiffness or damping in the suspension of the sensor.

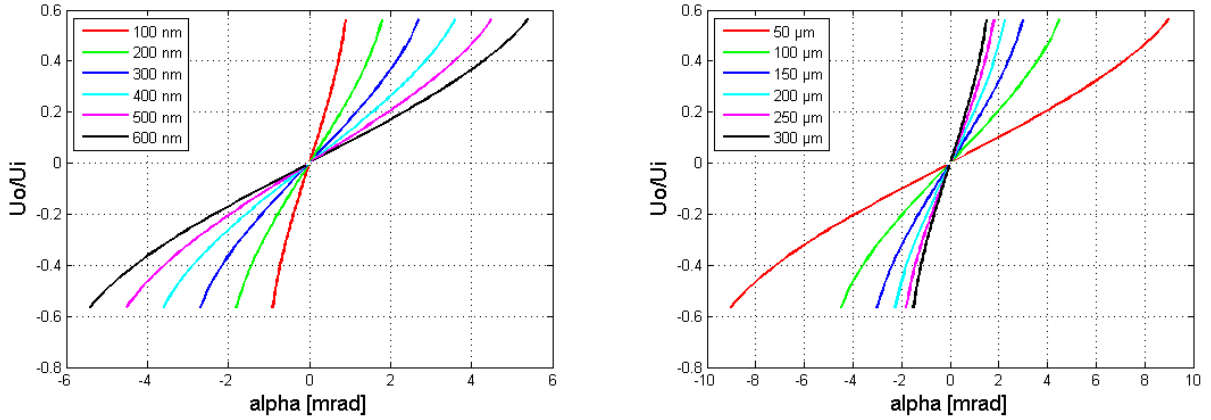


Fig. 2-10: Variations in the system transfer (U_o/U_i) and range of α as a function of L and g . Left: output voltage as function of α for different sizes of the air-gap g . Right: output voltage for different values of α for different length L of the electrodes.

Besides the two small differential capacitors, there are parasitic elements, like resistors and capacitors, in the system. On a chip with several sensors, the entire substrate is used as the common electrode of all sensors. The wiring on this chips is responsible for a parasitic capacitance parallel to the differential capacitances of the sensors. Since the total area of wiring is substantial on chips with 124 sensors, this capacitance can play a significant role in the behavior of the array of sensors [Fig. 2-11 Left]. The wiring also accounts for a certain resistance resulting in R-C combinations, slowing down the response. The capacitance resulting from the wiring is modeled by two capacitors parallel to the sensors [Fig. 2-11 Right].

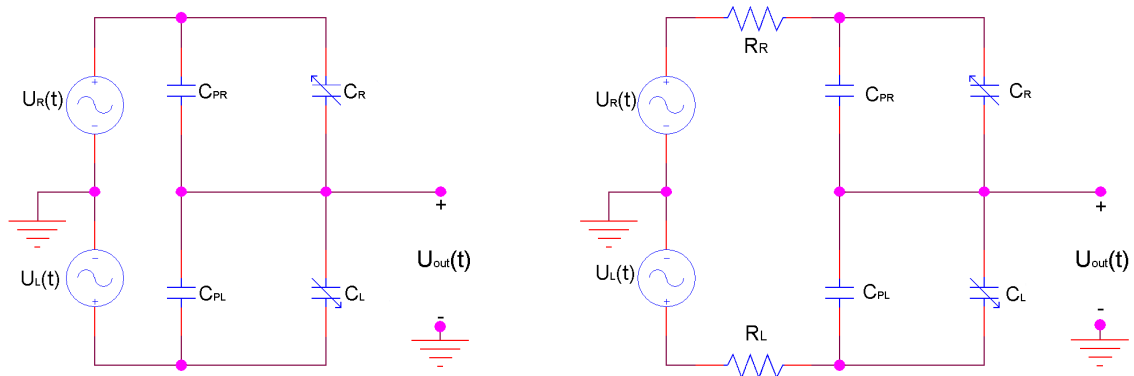


Fig. 2-11: Left: circuit diagram in case of parasitic capacitors parallel to the sensor. Right: circuit diagram including the parasitic capacitance and resistance of the wiring.

The parasitic capacitances are written as C_{pL} and C_{pR} and in general $C_{pL} \neq C_{pR}$ which results in a non zero output signal. Since the parasitic and sensor capacitors are in parallel, their values are added together. Using the principle of superposition while applying input signals described in (50) and (51), the magnitude of the output signal is written as:

$$U_{out} = \frac{C_{pR} - C_{pL} + C_{right}(\alpha) - C_{left}(\alpha)}{C_{pR} + C_{right}(\alpha) + C_{pL} + C_{left}(\alpha)} U_0 \quad (55)$$

With U_0 the magnitude of the input signal. Even when both parasitic capacitors C_{pL} and C_{pR} are equal in size, they still reduce the output signal making it important to reduce it as much as possible. Incorporating resistors in series with the two signal sources even further complicates the the output signal. Writing the two parallel capacitances as:

$$C_R = C_{pr} + C_{right}(\alpha) \quad (56)$$

$$C_L = C_{pl} + C_{left}(\alpha) \quad (57)$$

Using the circuit diagram [Fig. 2-11], and the input signals from (51) and (52), the modulus of the output is calculated.

$$U_o = \sqrt{\left(\frac{C_R^2 - C_L^2 + \omega^2 C_R^2 C_L^2 (R_L^2 - R_R^2)}{(C_L + C_R)^2 + (\omega C_L C_R (R_L + R_R))^2} \right)^2 + \left(\frac{2(\omega C_L^2 C_R R_L - \omega C_L C_R^2 R_R)}{(C_L + C_R)^2 + (\omega C_L C_R (R_L + R_R))^2} \right)^2} \quad (58)$$

With R_L and R_R representing the resistance of the wiring of the respective sides of the sensor. The α dependency is left out to get a more compact expression, of course C_r and C_l still depend on α . The phase of the output is then equal to:

$$\phi = \tan^{-1} \left(\frac{2(\omega C_L^2 C_R R_L - \omega C_L C_R^2 R_R)}{C_R^2 - C_L^2 + \omega^2 C_R^2 C_L^2 (R_L^2 - R_R^2)} \right) \quad (59)$$

Even though the modulus of the output depends on many variables, equation (58) indicates that having the two resistors as small as possible and at the same time equal to each other, results in the best output signal, as you would expect.

2.8 Mechanical hair sensor analysis

Calculating mechanical properties like the torsion stiffness of the suspension beams and the effective moment of inertia of the device provides knowledge about the behavior of the sensor at certain frequencies. The resonance frequency of the device in the desired mode of operation is calculated using the effective moment of inertia of the device and the torsion stiffness of the two rectangular suspension beams. The preferred motion of the sensors is tilting about the axis of the suspension beams [Fig. 2-12].

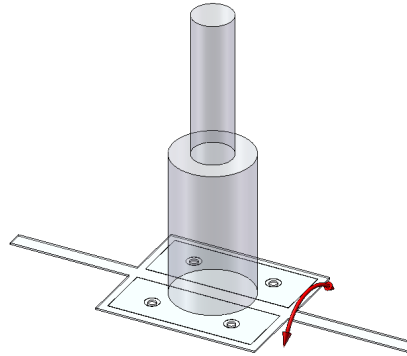


Fig. 2-12: Intended tilting motion of the hair sensor.

The torsion stiffness of a rectangular beam can be calculated using [18]:

$$T = \frac{\alpha}{l} \cdot I_p G \quad (60)$$

In this expression, T is the torque to realize a rotation of α radians. G is the shear stress modulus, l is the length of the beam and I_p is a factor depending on the shape and dimensions of the cross section of the beam. For a circular cross-section I_p is the polar moment of inertia. The hair sensor has suspension beams having a rectangular cross-section for which I_p is defined as [18]:

$$I_p = \frac{w_s t_s^3}{2} \frac{1}{8} \left(\frac{16}{3} - 3.36 \frac{t_s}{w_s} \left(1 - \frac{1}{12} \left(\frac{\left(\frac{t_s}{2} \right)^4}{\left(\frac{w_s}{2} \right)^4} \right) \right) \right) = \frac{w_s t_s^3}{3} - 3.36 \frac{t_s^4}{16} \left(1 - \frac{1}{12} \frac{t_s^4}{w_s^4} \right) \quad (61)$$

In this expression, the thickness and width of the rectangular beam are represented by t_s and w_s respectively. The shear modulus G is defined as the ratio of shear stress over shear strain. It is related to the Young's modulus E_s and the Poisson ratio ν of the beam material according to:

$$G = \frac{E_s}{2(1+\nu)} \quad (62)$$

Using the equation for the shear modulus (62) and the expression for the geometry (61) together in (60), results in the torsion stiffness K_t of a single suspension beam:

$$K_t = \frac{T}{\alpha} = \frac{KG}{l_s} = \frac{w_s t_s^3 E_s}{6l_s (1+\nu)} - 3.36 \frac{t_s^4}{32l_s (1+\nu)} \left(1 - \frac{1}{12} \frac{t_s^4}{w_s^4} \right) \quad (63)$$

Where l_s is the length of the suspension beam. The resonance frequency of an object suspended by a torsion stiffness is dependent on the moment of inertia of the object. The angular resonance frequency is next defined as;

$$\omega = \sqrt{\frac{K}{I}} \quad (64)$$

With K the torsion stiffness and I the moment of inertia of the object attached it. The membrane is suspended by two torsion beams which act in parallel. The torsion stiffness experienced by the membrane in such case, is twice that of a single beam. The moment of inertia of the sensor is the sum of the individual moments of inertia of the membrane and the hair. The moment of inertia I is defined as the integral over the volume of an object of the squared distance r between the axis of rotation and a volume element dV inside the object, multiplied by the mass-density $\rho(r)$ of the element.

$$I = \iiint_V r^2 \rho(r) dV \quad (65)$$

The mass density function $\rho(r)$ of the membrane is constant, hence this reduces to:

$$I = \rho \iiint_V r^2 dV \quad (66)$$

As stated the total moment of inertia is calculated by adding the moments of inertia of the membrane and the hair. First an expression for the moment of inertia of the membrane is derived. The rectangular membrane has a length l_m , a width w_m and thickness t_m and is tilting about the x -axis [Fig. 2-13].

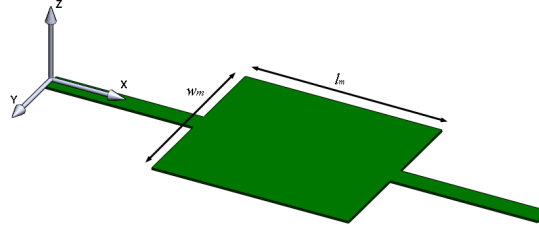


Fig. 2-13: Sensor membrane (length l_m and width w_m) with suspension beams. The suspension beams enable the membrane to tilt about the x-axis

The moment of inertia of the membrane tilting about the axis of the torsion beams and having a constant density ρ_m is written as:

$$I_m = \rho_m \int_{-\frac{l_m}{2}}^{\frac{l_m}{2}} \int_{-\frac{w_m}{2}}^{\frac{w_m}{2}} \int_0^{l_m} r^2 dx dy dz \quad (67)$$

The distance between a point on the membrane and the axis of tilt r is calculated applying Pythagoras resulting in:

$$I_m = \rho_m \int_{-\frac{l_m}{2}}^{\frac{l_m}{2}} \int_{-\frac{w_m}{2}}^{\frac{w_m}{2}} \int_0^{l_m} y^2 + z^2 dx dy dz \quad (68)$$

Evaluating this integral and writing the mass of the membrane as m_m results in:

$$m_m = l_m w_m t_m \rho_{SiRN} \quad (69)$$

$$I_m = \frac{1}{12} m_m (w_m^2 + t_m^2) \quad (70)$$

The shape of the hair on top of the membrane equals two cylinders on top of each other, the bottom cylinder having a diameter R and the top one a diameter $R/2$ [Fig. 2-14]. Each of the two cylinders has a length of $L/2$. The total moment of inertia of this structure is equal to the sum of the individual moments of inertia of the two cylinders.

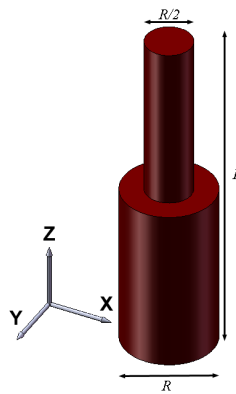


Fig. 2-14: Long sensor hair, showing diameters of the top ($R/2$) and bottom (R) part and the length of the hair L .

Using the definition of the moment of inertia (66) and changing to a cylindrical coordinate system, the moment of inertia of the bottom part of the hair tilting about the x-axis and having density ρ_h is written as:

$$I_{hb} = \rho_h \int_0^{\frac{L}{2}} \int_0^{2\pi} \int_0^R r z^2 + \frac{1}{2} r^3 - \frac{1}{2} r^3 \cos(2\phi) dr d\phi dz = \frac{1}{3} \pi \rho_h R^2 \left(\frac{L}{2}\right)^3 + \frac{1}{4} \pi \rho_h R^4 \frac{L}{2} \quad (71)$$

A similar approach is followed for the top part of the hair which also has density ρ_h , but now the diameter is $R/2$ and the axis of tilt is not at the bottom of the object but at a distance $L/2$. Using this, the moment of inertia of the top part of the hair is written as:

$$I_{ht} = \rho_h \int_{\frac{L}{2}}^L \int_0^{2\pi} \int_0^{\frac{R}{2}} r z^2 + \frac{1}{2} r^3 - \frac{1}{2} r^3 \cos(2\phi) dr d\phi dz = \frac{7}{3} \pi \rho_h \left(\frac{R}{2}\right)^2 \left(\frac{L}{2}\right)^3 + \frac{1}{4} \pi \rho_h \left(\frac{R}{2}\right)^4 \left(\frac{L}{2}\right) \quad (72)$$

The total moment of inertia of the hair tilting about its base is equal to the sum of the two parts:

$$I_{hair} = \frac{11}{96} \pi \rho_h R^2 L^3 + \frac{17}{128} \pi \rho_h R^4 L \quad (73)$$

Adding the moment of inertia of the membrane to this, results in the total moment of inertia of the hair sensor tilting about the longitudinal axis of the suspension beams:

$$I_{sensor} = \frac{11}{96} \pi \rho_h R^2 L^3 + \frac{17}{128} \pi \rho_h R^4 L + \frac{1}{12} \rho_m t_m w_m l_m (w_m^2 + t_m^2) \quad (74)$$

The angular resonance frequency ω_t of the sensor in torsion mode is then equal to:

$$\omega_t = \sqrt{\frac{K_t}{I_{sensor}}} \quad (75)$$

Besides this intended tilting motion, the sensor is able to oscillate vertically as well [Fig. 2-15]. The characteristics of this motion are different compared the torsion mode discussed above. The vertical stiffness of the suspension beams and the mass of the sensor now play a dominant role in the system.

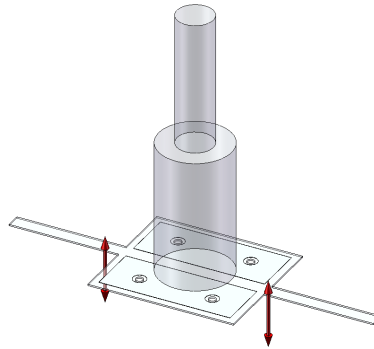


Fig. 2-15: Vertical mode of operation.

In the vertical mode the suspension beams are bending up and down, the vertical stiffness of a rectangular beam is defined as:

$$K_v = \frac{3E_s I_A}{l_s^3} \quad (76)$$

With E_s being the Young's modulus of the beam material, I_A is the second order moment of inertia over the cross section of the beam and l_s is the length of the beam. The second order moment of inertia or area moment of inertia is defined as the area integral over the cross section of the beam of the square distance r to the plane of deflection:

$$I_A = \int_A r^2 dA \quad (77)$$

In the vertical mode of the sensor, the suspension beams bent up and down about their centre plane located at $t_s/2$. The second order moment of inertia for the suspension beams is then written as:

$$I_A = \int_{-\frac{t_s}{2}}^{\frac{t_s}{2}} \int_0^{w_s} z^2 dy dz = \frac{w_s t_s^3}{12} \quad (78)$$

The angular resonance frequency ω_v in this mode is described by the expression for the resonance of a simple mass-spring system which is defined as the square root of the stiffness of the spring over the mass of the object. For the vertical motion of the hair sensor holds:

$$\omega_v = \sqrt{\frac{K_v}{m}} \quad (79)$$

With m the mass of the moving parts of the sensor which is equal to:

$$m_t = t_m w_m l_m \rho_m + \frac{5}{8} \pi R^2 L \rho_h \quad (80)$$

With t_m , w_m and l_m the dimensions of the membrane, R the radius of the bottom part of the hair, L the total length of the hair and ρ_m and ρ_h the densities of the membrane and hair respectively. Combining equations (76), (78), and (80) into (79) and realizing that (76) is the stiffness of a single beam, the angular vertical resonance frequency ω_v is written as:

$$\omega_v = \sqrt{\frac{K_v}{m}} = \sqrt{\frac{E_s w_s t_s^3}{2l_s^3 (t_m w_m l_m \rho_m + \frac{5}{8} \pi R^2 L \rho_h)}} \quad (81)$$

2.9 Electrostatic hair sensor analysis

The two differential sensor capacitors are also used to actuate the device using electrostatic forces resulting from the charge stored on the electrodes. Using this type of actuation, it is important to know the maximum voltage which can safely be applied to prevent instability of the sensor. Instability will result in pull-in of the membrane. Two different types of pull-in exist, vertical pull-in and torsion pull-in. The result of either type is a membrane stuck at the insulation layer and a permanently damaged sensor. To determine the theoretical value of the pull-in voltages, first the capacitance of the structure at rest is calculated. As stated in section 2.7 the capacitance of a static parallel plate capacitor is written as:

$$C = \frac{\epsilon_r \epsilon_0 A}{d} \quad (82)$$

In which d is the separation between the electrodes with area A , ϵ_0 is the permittivity of vacuum and ϵ_r is the relative permittivity of the material between the electrodes. In case of the hair sensors, there are three layers of two different materials between the electrodes. An air-gap is sandwiched between an insulation layer and the membrane. The capacitance of a parallel plate

capacitor having layers of different materials between its electrodes is analog to the total capacitance of a series circuit of separate capacitors with only one material between their electrodes. The material of the membrane and insulation is assumed equal here and its permittivity is represented by ϵ_s . The contribution of the two materials is then written as:

$$C_{air} = \frac{\epsilon_0 \epsilon_{air} A}{g - x} \quad (83)$$

$$C_s = \frac{\epsilon_0 \epsilon_s A}{t} \quad (84)$$

In these equations A is the electrode area of a an electrode on the membrane, t is the sum of the thicknesses of the membrane and insulation layer, g is the size of the air-gap at equilibrium and x is the reduction of the air-gap. Adding the two contributions, and noting that the relative permittivity of air is equal to one, leads to a total capacitance of a sensor at equilibrium ($x=0$) of:

$$C = \frac{\epsilon_0 \epsilon_{air} \epsilon_s A}{\epsilon_s g + \epsilon_{air} t} = \frac{\epsilon_0 A}{g + \frac{t}{\epsilon_s}} \quad (85)$$

Vertical pull-in

To derive an expression for the vertical pull-in voltage, the hair sensor is modeled by a simple electrostatic transducer with a spring [Fig. 2-16]. The transducer itself is a parallel plate capacitor with one stationary electrode and the other one suspended by the spring. The sensor membrane is suspended by two beams each with a vertical stiffness expressed in (76), the stiffness of the spring in the transducer model is than twice the vertical stiffness of a single beam K_v .

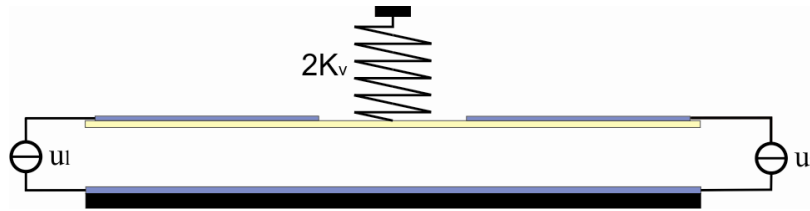


Fig. 2-16: Model of an electrostatic transducer with spring. In this case it is assumed that $U_l = U_r$.

Deriving an expression for the vertical pull-in voltage starts with the total energy in the system:

$$E = \frac{q^2}{2C} + K_v x^2 \quad (86)$$

In this case the sensor is driven by voltage and not by charge, so the energy cannot be used to describe the behavior of the sensors. The co-energy is used in cases where a electrostatic transducer is driven by voltage. The co-energy is derived from the expression for the energy by applying the Legendre transform:

$$E_{co} = E - qu \quad (87)$$

Using the energy of the electrostatic transducer with spring from equation (86), the co-energy is calculated using the Legendre transform (87) and the relation between the charge stored on and the voltage across the electrodes of a capacitor. The sensor uses two capacitors, in this case the capacitance expressed by C is the capacitance of a single capacitor. In case of vertical pull-in these capacitors act in parallel, so C is multiplied by two. The co-energy is then written as:

$$E_{co} = -Cu^2 + K_v x^2 \quad (88)$$

In this equation x is the vertical displacement of the sensor membrane. The total external force acting on the hair sensor is equal to the derivative of the co-energy to x :

$$F_{ext} = \frac{-u^2 \epsilon_0 A}{\left(g - x + \frac{t}{\epsilon_s}\right)^2} + 2K_v x \quad (89)$$

The first term in this expression is the contribution of the two capacitors while the second is the contribution of the suspension beams, note that K_v is the vertical stiffness of a single suspension beam. Vertical pull-in occurs when the electrostatic force is no longer balanced by the force applied the spring. Calculating the pull-in voltage starts by equating the electrostatic force to the spring force and solve the equation for u , the voltage across the electrodes [19]. Hence equating (89) to zero results in an expression for the voltage u necessary to reduce the air-gap by a distance x :

$$u = \pm \frac{\sqrt{2\epsilon_0 AK_v x} \left(g - x + \frac{t}{\epsilon_s}\right)}{\epsilon_0 A} \quad (90)$$

At a certain voltage the air-gap is reduced so much that the force applied by the spring and the electrostatic force are no longer balanced. In that case, the electrostatic force surpasses the force applied by the spring resulting in pull-in of the sensor membrane. The value for x , at which the electrostatic force starts to surpass the spring force is calculated by differentiating the expression in (90) to x , equating it to zero and solving it for x . The expression in (90) represents two equal but opposite expressions, the positive one is used for further analysis. The negative expression results in an equal but opposite value of the pull-in voltage, since it the polarity of the voltage does not affect the electrostatic force. Differentiating the positive part of expression (90) to x yields:

$$\frac{du}{dx} = \frac{K_v \left(g - x + \frac{t}{\epsilon_s}\right) \sqrt{2}}{2\sqrt{\epsilon_0 AK_v x}} - \frac{\sqrt{2\epsilon_0 AK_v x}}{\epsilon_0 A} \quad (91)$$

Equating this expression to zero and solving it for x results in an expression for the reduction of the air-gap x at which pull-in of the sensor occurs:

$$x_{pull-in} = \frac{1}{3} \left(g + \frac{t}{\epsilon_s}\right) \quad (92)$$

To calculate the pull-in voltage, x in (90) is substituted by this expression, the resulting vertical pull-in voltage is then equal to:

$$u_{piv} = \frac{2}{9} \frac{\sqrt{6} \sqrt{\epsilon_0 AK_v} \left(g + \frac{t}{\epsilon_s}\right) \left(g + \frac{t}{\epsilon_s}\right)}{\epsilon_0 A} \quad (93)$$

Torsion pull-in

Torsion pull in occurs when the effective torsion stiffness goes to zero. In that case, the tilt angle α is so large that the membrane tilts on until it hits the insulation layer. As stated in section 2.7 the capacitance of the sensor depends on the tilt angle α . Again the system is modeled by an electrostatic transducer with a spring, however in this case the movable electrode is suspended by a torsion spring $2K_t$ [Fig. 2-17]

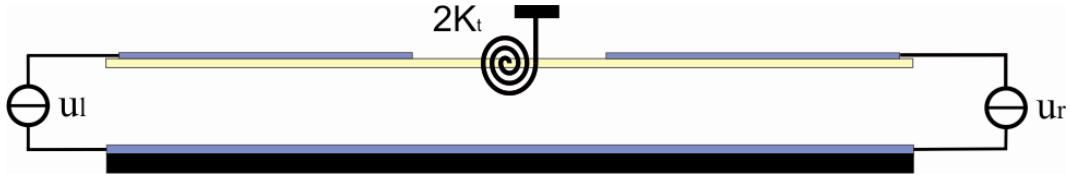


Fig. 2-17: Model of an electrostatic transducer with a torsion spring K_t . A voltage applied by either U_l or U_r results in a certain tilt angle α .

Calculating the voltage at which the effective torsion stiffness goes to zero, starts again with the energy function of the system. For the electrostatic transducer with a torsion spring holds:

$$E(\alpha) = \frac{q^2}{2C(\alpha)} + K_t \alpha^2 \quad (94)$$

Because the transducer is driven by voltage instead of charge, again the co-energy needs to be used for further analysis. Applying the Legendre transform to (94) results in:

$$E_{co}(\alpha) = \frac{q^2}{2C(\alpha)} + K_t \alpha^2 - qu \quad (95)$$

When the membrane tilts the size of the air-gap between the capacitor plates depends on the distance to the axis of rotation. When the membrane is tilted by α degrees, at a distance w from the axis of rotation the size of the air-gap between the electrodes changes by:

$$x = w \sin(\alpha) \quad (96)$$

Using the capacitor relation between the charge stored on the electrodes and the voltage across the electrodes, rewriting equation (95) results in an expression for the co-energy which depends on alpha.

$$E_{co} = -\frac{1}{2} C(\alpha) u^2 + K_t \alpha^2 \quad (97)$$

The alpha dependence of the capacitance makes it difficult to find an analytical expression for the effective torsion stiffness for a non-zero alpha. Fortunately, the angles of tilt experienced by the hair sensors are very small so a parallel plate approximation is used. The effective torsion stiffness is equal to the second derivative of the co-energy to α :

$$K_{eff} = \frac{d^2}{d\alpha^2} \left(-\frac{1}{2} C(\alpha) u^2 + K_t \alpha^2 \right) \quad (98)$$

In tilting mode not only the size of the air-gap is dependent on the angle α , the electrode area of both capacitors is also α dependent. Expecting that the electrodes do not cover the entire surface of the membrane, the capacitance of a single capacitor is written as an integral over the electrode area. With l_e the length of the electrode (along the tilt axis), representing the start and end position of the electrodes with respect to the tilt axis by a and b and knowing that the relative permittivity of air (ϵ_{air}) is equal to one, the capacitance of the two capacitor is written as:

$$C_l(\alpha) = \int_{-b}^{-a} \frac{\varepsilon_0 \varepsilon_{air} \varepsilon_s l_e \cos(\alpha)}{\varepsilon_s (g - w \sin(\alpha)) + \varepsilon_{air} t} dw = \int_{-b}^{-a} \frac{\varepsilon_0 l_e \cos(\alpha)}{g - w \sin(\alpha) + \frac{t}{\varepsilon_s}} dw \quad (99)$$

$$C_r(\alpha) = \int_a^b \frac{\varepsilon_0 \varepsilon_{air} \varepsilon_s l_e \cos(\alpha)}{\varepsilon_s (g - w \sin(\alpha)) + \varepsilon_{air} t} dw = \int_a^b \frac{\varepsilon_0 l_e \cos(\alpha)}{g - w \sin(\alpha) + \frac{t}{\varepsilon_s}} dw \quad (100)$$

For small angles of α holds that

$$\sin(\alpha) \approx \alpha \quad (101)$$

$$\cos(\alpha) \approx 1 \quad (102)$$

Using these expressions in equation (99) and (100), the total capacitance of the sensor is written as the sum of the two integrals:

$$C(\alpha) = \int_{-b}^{-a} \frac{\varepsilon_0 l}{(g - \alpha w + \frac{t}{\varepsilon_s})} dw + \int_a^b \frac{\varepsilon_0 l_e}{(g - \alpha w + \frac{t}{\varepsilon_s})} dw \quad (103)$$

Using the parallel plate approximation, the effective stiffness for small angles is then written as:

$$K_{eff} = \lim_{\alpha \rightarrow 0} \frac{\partial^2}{\partial \alpha^2} \left(-\frac{1}{2} \int_{-b}^{-a} \frac{\varepsilon_0 l_e u^2}{(g - \alpha w + \frac{t}{\varepsilon_s})} dw - \frac{1}{2} \int_a^b \frac{\varepsilon_0 l_e u^2}{(g - \alpha w + \frac{t}{\varepsilon_s})} dw \right) + \frac{\partial^2}{\partial \alpha^2} K_t \alpha^2 \approx \lim_{\alpha \rightarrow 0} \left(-\frac{1}{2} \int_{-b}^{-a} \frac{\partial^2}{\partial \alpha^2} \frac{\varepsilon_0 l_e u^2}{(g - \alpha w + \frac{t}{\varepsilon_s})} dw - \frac{1}{2} \int_a^b \frac{\partial^2}{\partial \alpha^2} \frac{\varepsilon_0 l_e u^2}{(g - \alpha w + \frac{t}{\varepsilon_s})} dw \right) + 2K_t \quad (104)$$

Evaluating the integrals in the previous expression leads to an effective stiffness of:

$$K_{eff} = -\frac{\varepsilon_0 l_e u^2}{(g + \frac{t}{\varepsilon_s})^3} \left(\int_{-b}^{-a} w^2 dw + \int_a^b w^2 dw \right) + K_t = -\frac{\varepsilon_0 l_e u^2}{(g + \frac{t}{\varepsilon_s})^3} \frac{2}{3} (b^3 - a^3) + 2K_t \quad (105)$$

Equating the effective torsion stiffness to zero and solving it for u results in an expression for the torsion pull-in voltage:

$$u_{pit} = \pm \frac{\sqrt{3\varepsilon_0 \varepsilon_s l_e K_t (b^3 - a^3) (\varepsilon_s g + t) (\varepsilon_s g + t)}}{\varepsilon_0 \varepsilon_s l_e (b^3 - a^3)} \quad (106)$$

2.10 The very near field

To characterize the viscous coupling between the hair sensors, a flow source is needed. For this a loudspeaker characterized for flow is used. A characterization experiment is conducted in which the velocity of the membrane of the speaker is measured using a laser vibrometer. As a result of the motion of the loudspeaker membrane, the air in front of this membrane starts to vibrating as well. The velocity of the motion of this air is related to the velocity of the loudspeaker membrane. Because the experimentation platform containing the different hair sensor structures is placed in front of this membrane, it is important to know the velocity of the airflow. In general the sound field in front of a loudspeaker can be divided into three separate sections, the far field, the near field and the very near field [17]. For the hair sensor research, the particle velocity level (PVL) of the air in front of the speaker is the important parameter. The particle velocity at a distance r_n normal to the surface of a sound source depends on the size L of the source and the sound frequency f the source is emitting. In the very near field the particle velocity is almost independent of distance r_n to the source [Tab. 2-2] [20]. In the near field the PVL drops very rapidly with the square of the distance to the source and in the far field it is proportional to the reciprocal distance to the source.

Region	Condition	Particle velocity
Very near field	$r_n \ll \frac{L}{2\pi} \ll \frac{\lambda}{2\pi}$	$u(r_n) \approx \text{constant}$ $u(f) = \text{constant}$
Near field	$\frac{L}{2\pi} \ll r_n \ll \frac{\lambda}{2\pi}$	$u(r_n) \sim r^{-2}$
Far field	$r_n \gg \frac{\lambda}{2\pi}$	$u(r_n) \sim r^{-1}$

Tab. 2-2: Different sound fields with conditions

The loudspeaker which acts as the flow source in the experiments on the hair sensors is fitted with a four inch circular membrane. The very near field condition [Tab. 2-2] states that a source with such a diameter generates a relatively constant particle velocity up to a normal distance of 16 mm from the surface of the source provided the frequency of the sound is less than ~ 3 kHz. The different hair sensor structures need to be within a distance of 16 mm from the surface of the loudspeaker to be in the very near field.

3 Design

3.1 Introduction

In order to set up an experiment to investigate the viscous coupling between the MEMS hair-sensors, hair sensors have to be positioned in close proximity. The regular hair sensors are usually arranged in groups up to 124 sensors arranged in a regular pattern. Their design and dimensions are optimized for capacitive readout. Since the capacitive readout method is not used in the viscous coupling research, the design of the sensors is changed to enable groups of hair sensors to be positioned more close together.

This chapter discusses the design of the hair sensors. For viscous coupling research, the design is adapted and used as a building block to create the design of the experimentation platform containing several different hair sensor structures.

3.2 Sensor design

The principle of operation of the sensor has been discussed in section 2.4, here the actual design is discussed in more detail. The basic design of the sensor is a hair on top of a membrane with two electrodes on top. This membrane is suspended above a conductive substrate by two suspension beams. The electrodes together with the conductive substrate form a set of differential capacitors enabling electronic readout of the sensor.

Since the hair sensors are made using surface micromachining techniques, its design starts with the conductive substrate. This substrate acts as the common electrode in the differential capacitor setup. The substrate is insulated with silicon-rich nitride (SiRN) for processing reasons. The layer is engineered down to a minimum thickness of 200 nm in order not to decrease the capacitance of the device too much. To create the air-gap between the substrate and the membrane a sacrificial layer of 600 nm poly-silicon is used. The poly-silicon under the membrane is isolated by trenches for processing reasons. On top of the poly-silicon, the membrane is fabricated using 1 μm of SiRN. The membrane has a rectangular shape and is suspended by torsion beams [Fig. 3-1]. The membrane is equipped with four etch holes (5 μm) to speed up the release step during fabrication. The regular sensors use a membrane of a different and larger size (90 μm x 200 μm). The dimension of the membrane, perpendicular to the suspension beams is reduced from 200 μm to 90 μm enabling the sensors to be very close together.

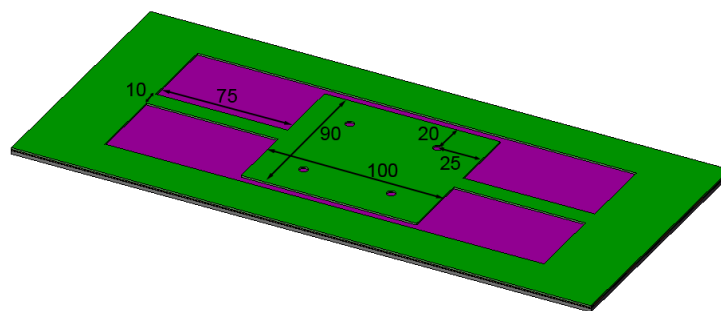


Fig. 3-1: Shape and dimensions [μm] of the membrane and torsion beams. The SRN layer itself has a thickness of 1 μm

The wiring and electrodes on top of the membrane are fabricated in a 100 nm layer of aluminum [Fig. 3-2]. In the aluminum the etch holes are slightly bigger (9 μm) to prevent the holes in the membrane from being covered in case of alignment issues concerning the wiring. The electrodes on the membrane are connected to the wiring on the chip by wires running over the suspension beams. On top of the electrodes in the centre of the membrane the hair is positioned. The hair is made of SU-8, a common type of photo resist used in MEMS processing. The desired length of the hair is 1 mm, however the current types of SU-8 are only capable of creating smooth layers having a thickness of 450 μm . Using two separate layers of SU-8 on top of each other enables fabrication

of a hair 900 μm in length. The use of two separate layers has the advantage that the diameter of the top and bottom part of the hair can be dissimilar. To reduce the moment of inertia of the hair, the diameter of the top part is reduced. For the bottom part a diameter of 50 μm is used while the top has a diameter of 25 μm . Reducing the moment of inertia increases the range of frequencies the sensor can operate in. Another advantage of having two separate layers of SU-8 is that it enables having two different lengths of hairs which is interesting for the viscous coupling research. A downside of using two separate layers is that it introduces many extra processing steps, complicating the fabrication process. Misalignment of the two layers with respect to each other or with respect to the membrane can cause strange effects in the behavior of the hair sensor.

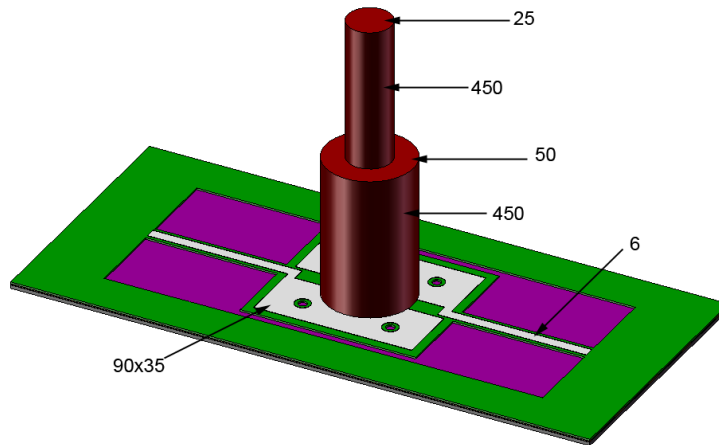


Fig. 3-2: Sensor design, dimensions of the hair and electrodes [μm].

For convenience, the properties of the materials used for fabricating the sensor and the sensor dimensions are summarized in table [Tab. 3-1].

Description	Symbol	Value	Unit	Description	Symbol	Value	Unit
Length, membrane	l_m	$100 \cdot 10^{-6}$	m	Length, total hair	L	$900 \cdot 10^{-6}$	m
Width, membrane	w_m	$90 \cdot 10^{-6}$	m	Poisson ratio SiRN	ν_{SiRN}	0,24	
Thickness, membrane	t_m	$1 \cdot 10^{-6}$	m	Youngs modulus SiRN	E_{SiRN}	$310 \cdot 10^9$	Pa
Length, suspension beam	l_s	$75 \cdot 10^{-6}$	m	Permittivity of Vacuum	ϵ_0	$8,854 \cdot 10^{-12}$	F/m
Width, suspension beam	w_s	$10 \cdot 10^{-6}$	m	Relative permittivity, Air	ϵ_{air}	1	
Thickness, suspension beam	t_s	$1 \cdot 10^{-6}$	m	Relative permittivity, SiRN	ϵ_{SiRN}	7,5	
Thickness, insulation layer	t_i	$0,2 \cdot 10^{-6}$	m	Density of SU-8	ρ_{SU8}	1200	Kg/m^3
Total SiRN thickness	d	$1,2 \cdot 10^{-6}$	m	Density of SiRN	ρ_{SiRN}	3100	Kg/m^3
Radius of the bottom hair	R	$25 \cdot 10^{-6}$	m	Kinematic Viscosity Air	ν_{air}	$1,5 \cdot 10^{-5}$	m^2/s

Tab. 3-1: Properties of the sensor and materials used.

The values in table [Tab. 3-1] and the expressions derived in chapter 2 are used to calculate the actual values for the resonance frequencies in the different modes of operation of the sensor as well as the two pull-in voltage. The results of this analysis are displayed in table [Tab. 3-2].

Mechanical property	Value	Unit	Electrostatic property	Value	Unit
Torsion stiffness	$1,0411 \cdot 10^{-8}$	Nm/rad	Pull in voltage vertical	2,93	V
Torsion resonance	1154	Hz	Pull in voltage torsional	16,4	V
Vertical stiffness	3,674	N/m			
Vertical resonance	8293	Hz			

Tab. 3-2: Numerical results of the analysis on the hair sensor.

3.3 Experimentation platform design

The experimentation platform used for characterization of viscous coupling is based on the sensor design discussed in section 3.2. The sensors are arranged in different configurations. Each configuration is assigned a unique name and each sensor within a configuration is numbered so each sensor on the experimentation platform is uniquely identifiable [Appendix A]. Various geometrical parameters are varied among the different hair sensor structures.

To study the effect of sensor separation on the viscous coupling between the hair sensors, three sensors are placed in a row [Fig. 3-3]. The platform design contains twelve of these rows of three sensors divided into six groups of two structures. Each group has a different separation between the sensors. This separation S , is defined as the distance between the tilt axis of two sensors. The separation between the sensors in these structures is varied between 100 μm and 600 μm . The hairs on the sensors in these row configurations are all 900 μm in length, each hair has the same diameter (50 μm bottom, 25 μm top) and shape. The first hair sensor in each row can be actuated by electrostatic forces to study the effect of sensor motion itself on the coupling between them. Rows of three sensors with separations of 100 μm , 150 μm , 200 μm , 300 μm , 400 μm and 600 μm are available on the experimentation platform.

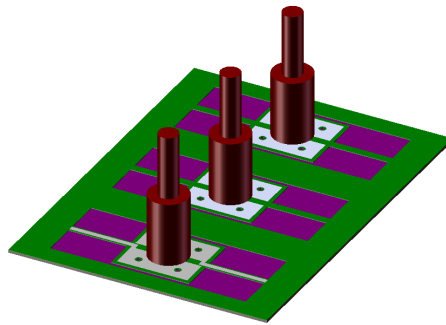


Fig. 3-3: Design of a structure with three sensors in a row (150 μm separation)

The hairs on the cerci of a cricket have variable directions of sensitivity [5,6], the orientation of one hair sensor with respect to another could play a role in viscous coupling. To study the effect of the orientation of a hair sensor, the platform design includes three rows of two hair sensors in which the second sensor has a preferred direction of tilt which is rotated 90° with respect to the tilt direction of the first one [Fig. 3-4]. The SU-8 hair on the sensors used here are all 900 μm in length. The separation between the hair sensors in each of the three rows is varied, they are separated by 190 μm , 240 μm and 290 μm respectively. The first hair sensor in each of the rows can be actuated by electrostatic forces.

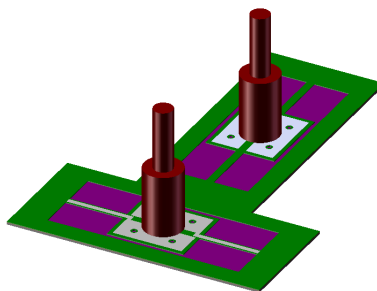


Fig. 3-4: Design of a structure containing two sensors with different orientation (separation 190 μm)

To study the effect of viscous coupling between hair sensors arranged in regular patterns, nine sensors are arranged in six rows, shifted with respect to each other [Fig. 3-5]. The hair sensors are arranged in a 1-2-1-2-1-2 configuration. The sensor on the first row is one that can be actuated by charging its capacitors. The other eight sensors are free to move under the viscous action of the airflow. As is the case in the two previous designs, the distance between the rows of sensors is

varied. Three of these kind of shifted row structures are included in the design of the experimentation platform, having separations of 113 μm , 150 μm and 200 μm between the rows.

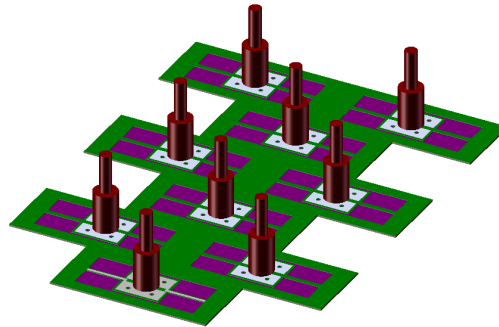


Fig. 3-5: Structure design of a pattern of shifted rows of sensors, the sensor on the first row can be set in motion.

Besides this sensor arrangement discussed above, there are several other possibilities to arrange the hair sensors in a regular pattern. For instance a very symmetric pattern, is a matrix. Five different matrix structures, each containing nine sensors arranged in three columns each having three rows, are designed. Besides the common matrix shape, another common property in these five structures is the sensor in the center. This particular sensor has a long (900 μm) hair and it can be set in motion by alternately charging and discharging its capacitors.

In the first of these five matrix designs, the eight other hair sensors are free to move and have the same orientation as the hair sensor in the center of the matrix [Fig. 3-6]. The length of the hairs on these eighth sensors is also 900 μm and the separation between the sensors in both directions is 300 μm .

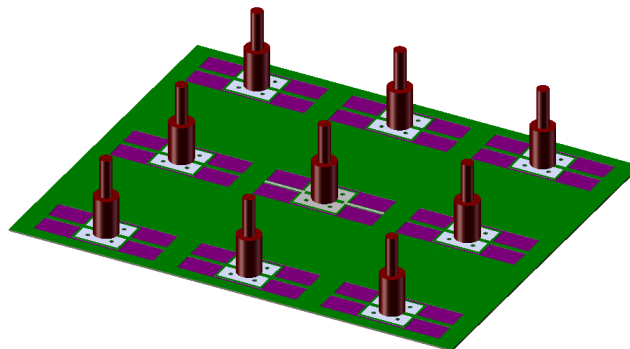


Fig. 3-6: Sensors arranged in a three by three matrix pattern. The center sensor can be set in motion, all sensors are separated by a distance of 300 μm .

To characterize the effect of the length of the hair on the viscous coupling between the sensors, three structure each containing four sensors in a 1-2-1 arrangement are designed. For this reason, the hairs of the sensors on the second and third row have a length of only 450 μm [Fig. 3-7]. This is realized by only using the bottom layer of SU-8, the diameter of these short hairs is 50 μm , which is equal to the diameter of the bottom part of the long hairs. As is the case in the other row designs, the hair sensor at the first row can be actuated and contains a hair with a length of 900 μm and the distance between the rows is varied. Separations of 113 μm , 150 μm and 200 μm are available on the platform.

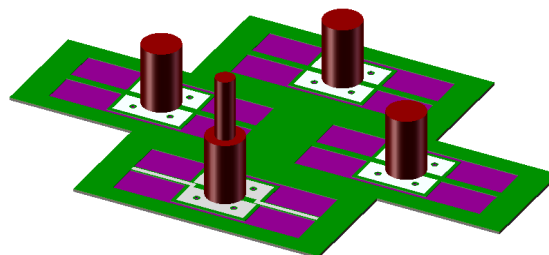


Fig. 3-7: Design of a shifted array with short hairs, the sensors on the second and third row have a hair of 450 μm in length while the first sensor has a hair of 900 μm in length. The first sensor can be set in motion.

In the four remaining matrix designs, the three parameters, separation, hair-length and sensor orientation are combined. In one of those designs, the eight sensors surrounding the sensor in the centre of the matrix have short hairs (i.e. $450\ \mu\text{m}$) [Fig. 3-8]. In this matrix design, the separation between the rows and columns is $300\ \mu\text{m}$ as is the case in the matrix design discussed above.

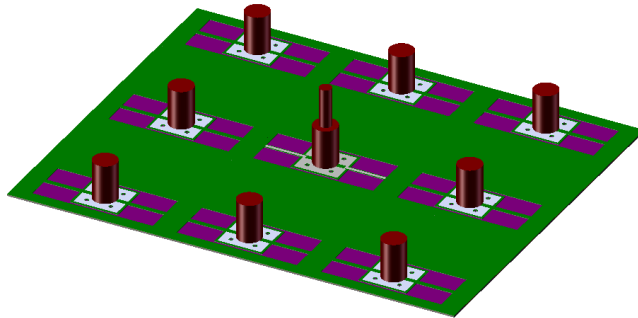


Fig. 3-8: Matrix design have a center sensor with a long hair ($900\ \mu\text{m}$), surrounded by sensors having a short hair ($450\ \mu\text{m}$). The rows and columns of sensors are separated by $300\ \mu\text{m}$.

In the last three matrix designs, there is an extra common feature. The orientation of four of the sensors in is rotated by 90° [Fig. 3-9]. In two of these designs all sensors have hairs with a length of $900\ \mu\text{m}$. The separation between the rows and columns in these structures is changed, two structures with separations of $250\ \mu\text{m}$ and $300\ \mu\text{m}$ are on the experimentation platform.

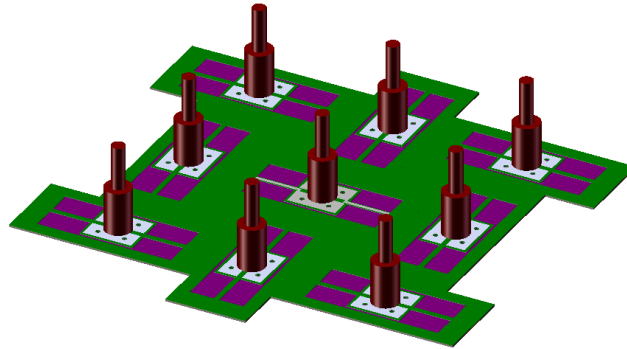


Fig. 3-9: Matrix design with four sensors rotated 90° with respect to the center sensor. For this type of configuration, two structures with separations of $250\ \mu\text{m}$ and $300\ \mu\text{m}$ between the rows and columns are on the experimentation platform.

In the last matrix design the separation between the hair sensors is kept at $250\ \mu\text{m}$. In this case the eighth sensors surrounding the center one contain a short hair ($450\ \mu\text{m}$) [Fig. 3-9].

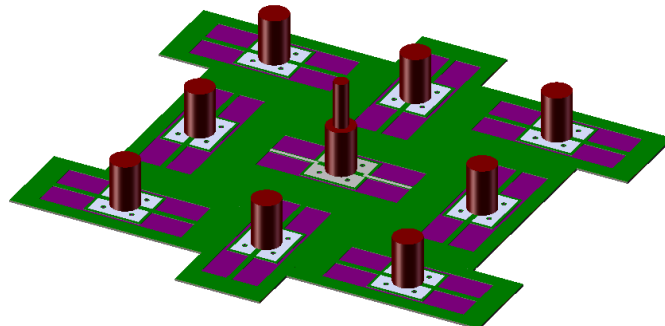


Fig. 3-10: Matrix design with four sensor rotated 90° with respect to the other sensors. The center sensor with long hair ($900\ \mu\text{m}$) is surrounded by eighth sensors with short hairs ($450\ \mu\text{m}$).

All of the structures discussed above are placed together on a single chip. Some of the structures like the rows of three hair sensors and the five different matrix designs are duplicated on the chip to have extra samples of these structures. The experimentation chip layout and the reference system for the different hair sensor structures and sensor numbers is discussed separately in appendix A.

4 Fabrication and inspection

4.1 Introduction

The research on viscous coupling between the hair sensors is part of a project focused on the properties and development of this type of hair sensors. The design of the viscous coupling experimentation platform is combined with other designs which can be fabricated using the same process. The combined design is used to create the set of masks necessary for fabrication. These masks are used by clean room technicians to process the wafers in order to realize these designs. The fabrication process itself is discussed in the next section. After fabrication, the different designs are extracted from the wafers and the chips containing the viscous coupling experimentation platform are inspected using different methods. The results of these inspections are discussed at the end of this chapter.

4.2 Fabrication process

The sensors are fabricated on top of a substrate of high conductive silicon. The silicon substrate also acts as the common electrode in the differential capacitor setup. The fabrication itself starts by insulating this conductive substrate by depositing a 200 nm layer of silicon rich nitride (SiRN) in a low pressure chemical vapor deposition (LPCVD) process [Fig. 4-1]. This layer not only insulates the substrate electrically but it also acts as an etch stop layer in the final release step. The thickness of this layer is kept at a minimum so it still protects the silicon substrate during the sacrificial layer etch, but it is thin enough not to decrease the capacitance of the two sensor capacitors too much.



Fig. 4-1: First process step, the deposition of SiRN. A: conductive silicon substrate. B: substrate insulated by the deposition of a 200 nm layer of SiRN (LPCVD).

On top of the SiRN insulation layer, a 600 nm thick sacrificial layer of poly-silicon is deposited in a LPCVD process. Isolation trenches are fabricated in this layer, these will fill up again when depositing the next layer [Fig. 4-2]. These trenches isolate the part of the poly-silicon which needs to be removed in the device release step and prevent under etching during the device release step. The width of the trenches is 3 μm and they are fabricated using reactive-ion etching (RIE). Besides these trenches a contact hole is made as well, this hole enables access to the conductive substrate to create the bond-pad for the bottom electrode later on.

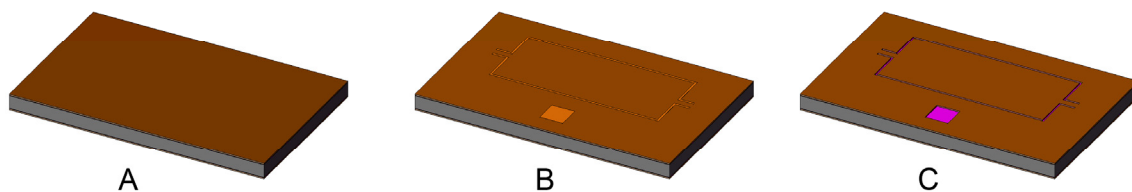


Fig. 4-2: Processing of the sacrificial poly-silicon layer. A: deposition of the 600 nm poly-silicon layer (LPCVD). B: mask for the isolation trenches and contact hole. C: isolation trenches and contact hole etched into the poly-silicon layer (RIE)

On top of the poly-silicon layer a 1 μm layer of SiRN is deposited (LPCVD). The trenches and contact hole in the poly-silicon layer underneath fill up with SiRN as well. This SiRN layer is patterned using photolithography to create the membrane and suspension beam, the etch holes in the membrane and the contact hole to the substrate as this needs to be opened up again [Fig. 4-3 B]. The SiRN is etched in a two step RIE process, the membrane and suspension beams are ready but still supported by the poly-silicon sacrificial layer [Fig. 4-3 C]

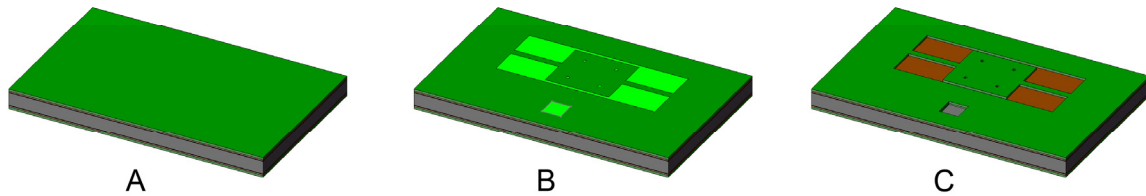


Fig. 4-3: Fabrication of the membrane and suspension beams. A: depositing the 1 μm layer of SiRN for the membrane and suspension beams (LPCVD). B: patterning the membrane, etch and contact holes and the suspension beams. C: etching the SiRN layer to fabricate the membrane, suspension beams and contact holes (two-step RIE).

The electrodes and electrical wiring are fabricated in a 100 nm layer of low stress aluminum deposited using a low-power sputtering process at room temperature [Fig. 4-4 A]. The electrodes with their etch holes, the wiring and the bond-pads are patterned and the aluminum is etched in a wet etch at room temperature using a standard resist developer [Fig. 4-4 C].

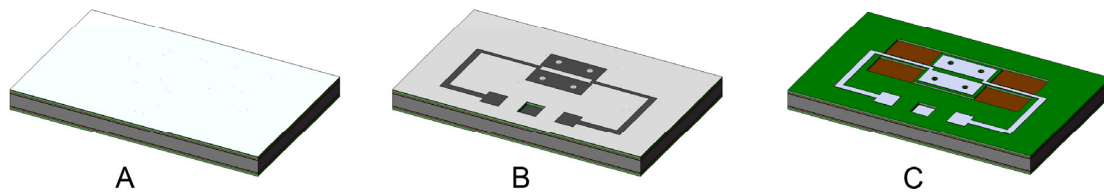


Fig. 4-4: Fabrication of the aluminum wiring, electrodes and bond-pads. A) Deposition of the 100 nm aluminum layer (Low power sputtering). B) Patterning the electrodes wiring and bondpads. C) Etching of the aluminum (Wet etching)

Before the hair is fabricated on top of the membrane the SiRN, the back side of the substrate is patterned to facilitate the backside alignment of the two SU-8 layers. The hair itself is fabricated in a two step photolithographic procedure because the current types of SU-8 can only have a maximum layer thickness of about 450 μm . The first layer of SU-8 is deposited on top of the device and the bottom part of the hair is patterned into this layer [Fig. 4-5 A]. After exposure and baking this first layer, a second layer of SU-8 is deposited on top of it. The top part of the hair is patterned into this second SU-8 layer [Fig. 4-5 B]. The two SU-8 layers are developed in a single processing step which creates the hair on top of the membrane [Fig. 4-5 C].

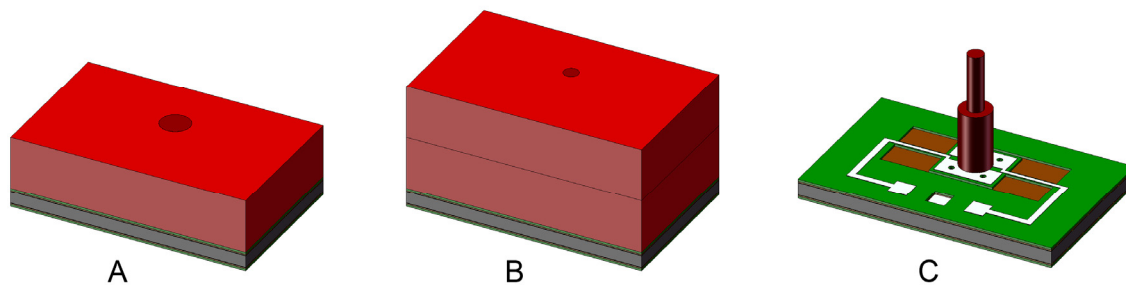


Fig. 4-5: Fabricating the SU-8 hair on top of the membrane. A: depositing and exposing the first layer of SU-8. B: depositing and exposing the second SU-8 layer. C: development of the two layers in a single step results in the SU-8 hair.

The final fabrication step is to release the device by removing the poly-silicon sacrificial layer within the area isolated by the trenches. This step involves a plasma etch. To prevent direct ion bombardment on the SiRN membrane and suspension beams during the sacrificial layer etch (SLE), the entire wafer is covered with a special two layer glass cover which is gas permeable but prevents the ions from hitting the devices directly. After the SLE the devices are released and ready [Fig. 4-6 B].

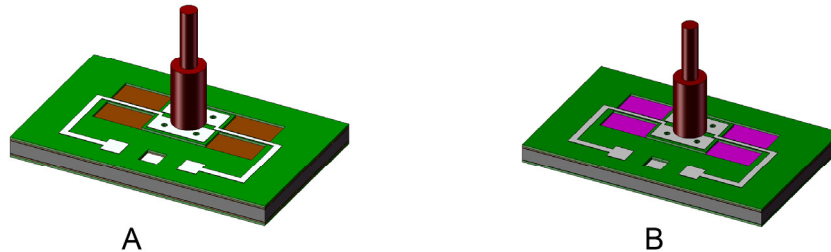


Fig. 4-6: Release step of the device. A: complete unreleased hair sensor. B: complete released device after removal of the sacrificial layer (plasma etch).

After fabrication the different chips are extracted from the wafer and inspected. The results of the inspections on the viscous coupling devices are discussed in the next section.

4.3 Inspection

After the fabrication process is completed, the devices are inspected to verify if the result of the fabrication process meets the design specifications. Inspections are conducted using an optical microscope and a scanning electron microscope (SEM). First the experimentation platform is inspected using an optical microscope. Looking at the platform from the top, the hair sensors appear to be perfect [Fig. 4-7]. The shape of the sensors and different sensor structures on the chip agrees with the design, each sensor is perfectly rectangular as are the electrodes on top and the suspension beams. Even the etch holes are clearly visible in the optical microscope images.

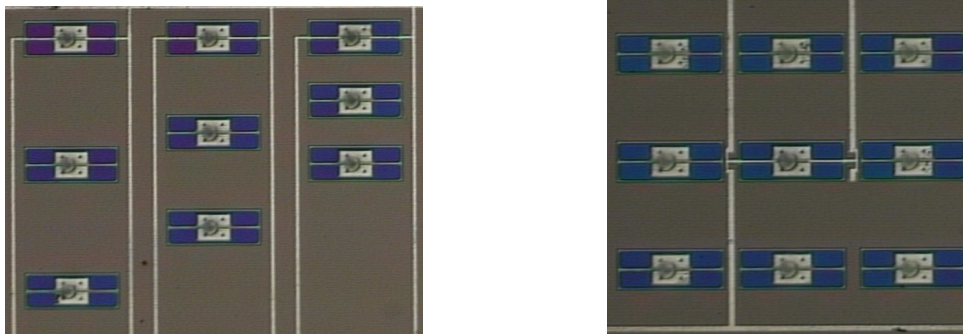


Fig. 4-7: Optical microscope image, Top view of some of the structures. Left: some of the 'Inline' series of structures. Right: matrix structure (Array-300µm)

To check if the sensors are properly released, the image of the optical microscope was focused on the tip of the hairs on the sensors. Carefully some flow was applied and indeed motion of the hair tips was observed.

Besides the successful completion of the fabrication process and the fact that motion of the sensors was observed, a more detailed inspection of the wiring revealed a couple of 'opens'. These opens turned out to be the result of an error in the mask design. As a result of this, the hair sensors in some of the structures cannot be set in motion. Inspection by optical microscope also revealed an issue with one of the six groups of three sensor row structures. The hairs on the sensors in the row structure, with a sensor separation of 100 µm, are all merged together [Fig. 4-8]. In the picture it is not clearly visible what the extend of this issue is. Anyhow, use of this particular structure in viscous coupling experiments is not possible.

For use in experiments, the chips are mounted on a printed circuit board (PCB). The PCB not only makes the chips more manageable, it also provides the necessary electrical connections to actuate some of the hair sensors on the chip. The chip itself is electrically connected to the PCB by three wire-bonds.

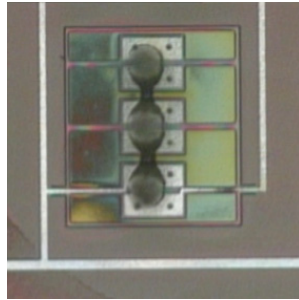


Fig. 4-8: Three hair sensors in a row with a 100 μm separation between them. Clearly all the SU-8 hairs are merged together by some SU-8 residue.

Other issues concerning the sensors showed up during inspection with the SEM. The images of the sensors made using the SEM indicate that the SU-8 hairs on the sensors are a bit curved. Inspection also revealed that the top part of the hairs is not always centered with respect to the bottom part [Fig. 4-9 left]. Even more detailed SEM inspections revealed that the SU-8 hair is not always positioned in the center of the membrane [Fig. 4-9 right]. The position of the hair with respect to the membrane affects the moment of inertia of the sensor. When positioned off center, the bottom part of the SU-8 hair can even cover the etch holes which would result in problems during the release step of the device.

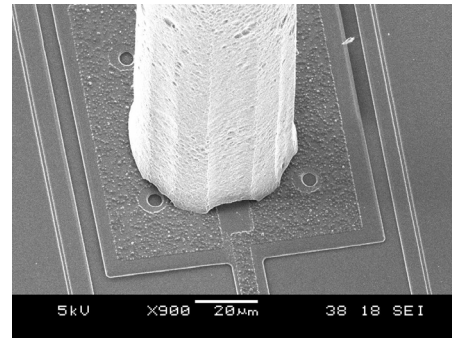
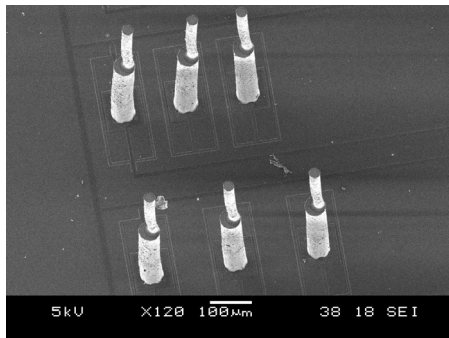


Fig. 4-9: SEM images of the hair sensors. Left: misalignment of the top part of the hair. Right: sensor having an off-center hair almost covering one of the etch holes in the membrane.

Despite the minor issues discussed above, the SEM images [Fig. 4-10] and a couple of preliminary experiments proof that the modification of the hair sensor design has been successfully realized and that these hair sensors appear to be in working order. The different hair sensor structures on the viscous coupling chip agree with their design. There are twenty different hair sensor structure designs. Of these twenty different designs, eleven have a duplicate available on the chip. The total number of different structures available for acoustic experiments is nineteen. The number of different structures available for electrostatic experiments is eighteen, since one of the 'opens' in the wiring concerns a structure with has not a copy available on the chip.

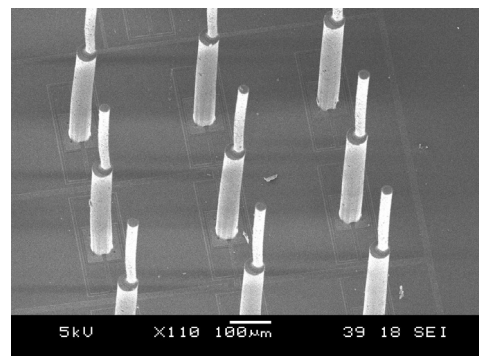
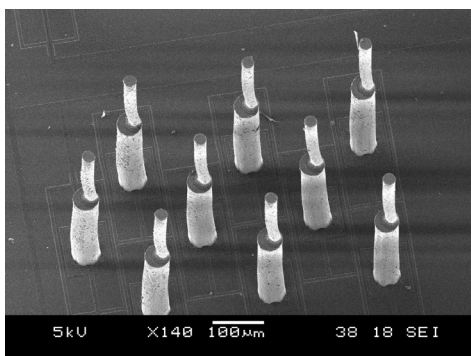


Fig. 4-10: SEM pictures of some sensor structures. Left: shifted array of sensors with a separation of 100 μm . Right: matrix design with a separation of 300 μm between the rows and columns of sensors.

5 Experiments and results

5.1 Introduction

The variety of structures on the platform enable lots of experiments. For each structure experiments under different flow conditions are possible and certain hair sensors can be set in motion by alternately charging and discharging the capacitors. Combining all these features in experiments will generate a lot of data. First a brief measurement plan is discussed. In the experiments, the deflection of the hair sensor membrane is measured using a laser vibrometer, a device using an optical, non-contact, method of measuring the velocity of a moving object. The deflection of the object is calculated using the velocity measurement data. This method of measuring and the principle behind it is discussed in section 5.3.

In the viscous coupling experiments, a loudspeaker is used to generate flow. To characterize the flow, the motion of the speaker membrane is measured using the laser vibrometer. The calibration process is discussed in section 5.4. The modified loudspeaker is used as the flow source in the measurement setup to characterize the viscous coupling between the hair sensors in the structures on the experimentation platform. At the end of this chapter the results of the different acoustic and electrostatic experiments are discussed.

5.2 Measurement plan

Because of the large amount of experiments possible a plan is made to describe the different experiments. Part of this plan is a device reference list [Appendix A]. In this list the different structures are described, tagged with a name and each hair sensor within a structures is numbered so each hair-sensor on the chip is uniquely identifiable.

The basic plan is to have two different types of actuation in the experiments [Fig. 5-1]. Acoustic actuation is accomplished by using a loudspeaker as the flow source. Electrostatic actuation of certain sensors is realized by alternately charging and discharging the capacitors by applying a combination of AC and DC voltages. The acoustic experiments should provide knowledge about viscous effects due to presence of other hair sensors. The role of hair sensor motion in the coupling between the sensors is studied in electrostatic experiments. Since only one sensor in each structure is capable of being set in motion, the effect of this motion on the other sensors in the structure can be studied by measuring the deflection of these sensors. Both methods of actuation could also be combined in a single experiment, measuring the effect of a moving hair sensor on a passing airflow.

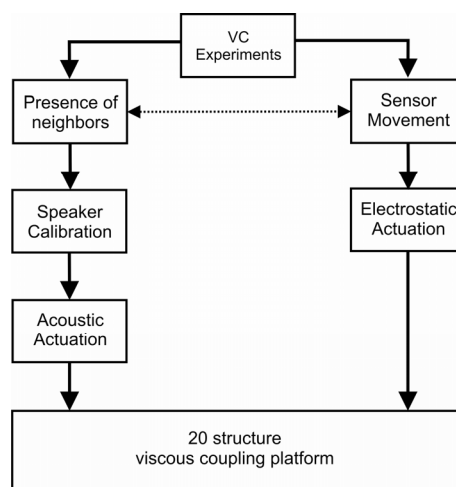


Fig. 5-1: Schematic measurement plan

5.3 Laser vibrometry

Laser vibrometry uses the principle of the Doppler frequency shift that occurs when the source of a wave is moving with respect to an observer. This effect occurs also when a wave originating from a stationary source is reflected to a stationary observer by a reflective surface in motion. In a laser vibrometer a laser beam is projected onto a vibrating surface. The vibration of this surface causes a Doppler frequency shift of the laser light. When the source of a wave is moving with respect to a stationary observer the Doppler frequency shift f_d is defined as:

$$f_d = \frac{v}{\lambda_l} \quad (107)$$

In this equation v is the velocity of the source with respect to the observer and λ_l is the wavelength of the laser light. When a wave from a stationary source is reflected by a vibrating surface towards a stationary detector a Doppler shift occurs as well. This situation is analog to a source moving towards a stationary observer at a velocity of $2v$. The Doppler effect is used in a laser vibrometer to measure the velocity of a vibrating object. The Doppler shift of the laser light in a laser vibrometer setup is written as:

$$f_d(t) = \frac{2v(t)}{\lambda_l} \quad (108)$$

In this equation $v(t)$ is the velocity of the vibrating object. Because of the high frequency of the laser light used ($4.74 \cdot 10^{14}$ Hz), it is not possible to directly demodulate the reflected light signal. In laser vibrometry an interferometer is used to measure the Doppler frequency shift. Different types of interferometers exist. In the Polytec MSA 400 setup, the setup used in the viscous coupling experiments, the Michelson arrangement is used. A Michelson interferometer uses a laser beam, which is split into two separate laser-beams by a beam splitter. Each of the two laser beams then travels through a different part of the setup [Fig. 5-2].

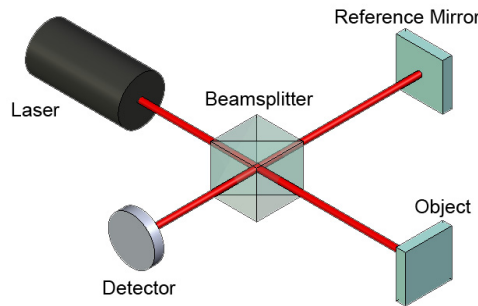


Fig. 5-2: Michelson interferometer setup.

One beam, referred to as the measurement beam, travels towards the vibrating object. The reflective surface of the vibrating object, a requirement to use this method, reflects the beam back towards the beam splitter. Besides the Doppler frequency shift a time dependent phase shift occurs because the length of the path the laser beam travels along, changes with time. The other beam coming from the beam splitter, referred to as the reference beam, travels towards a stationary mirror and is reflected back towards the beam splitter as well. At the beam splitter, the reference and measurement beam are combined and reflected towards a photo-detector. The two laser beams create an interference pattern on the surface of the photo detector. This interference pattern is modulated according to the Doppler frequency shift.

The He-Ne laser in the Polytec setup emits light of a single frequency. The light emitted by the laser can be treated as a plane wave. A plane wave has wave fronts which form parallel planes of infinite length with a constant amplitude. To explain how the intensity of the laser light that strikes the detector is related to the velocity of the vibrating object first some theory about electromagnetic waves is discussed.

The energy u per unit volume in an electromagnetic wave is equal to:

$$u = \frac{1}{2} \left(\epsilon_0 E^2 + \frac{1}{\mu_0} B^2 \right) \quad (109)$$

In which E is the electric field, B the magnetic field, ϵ_0 is the permittivity of vacuum and μ_0 the magnetic permeability. In a plane wave the amplitude of the electric field is related to the amplitude of the magnetic field according to:

$$B^2 = \frac{1}{c^2} E^2 = \mu_0 \epsilon_0 E^2 \quad (110)$$

The energy per unit volume in a plane wave is then written as:

$$u = \epsilon_0 E^2 \quad (111)$$

A travelling wave carries energy along with it. The Poynting vector S defines the energy flux density which is the energy per unit area per unit time. For plane waves, the Poynting vector is equal to the energy per unit volume multiplied by the velocity of the wave. With c indicating the speed of light the Poynting vector is written as:

$$S = cu \quad (112)$$

The intensity of a plane wave is equal to the time average power per unit area, this is equal to the time average energy density multiplied by the velocity c of the wave. It is the intensity of the laser-beam which is modulated by the vibration of the object.

$$I = \langle S \rangle = \langle c \epsilon_0 E^2 \rangle \quad (113)$$

This theory is now used to explain the operating principle of a laser vibrometer. The dependence of the light intensity on the velocity of the vibrating object is mathematically described here.

The light emitted by a laser is described using a complex expression:

$$E(t) = \text{Re} \left(C e^{j(\omega_l t + \phi)} \right) \quad (114)$$

This laser beam travels to the beam splitter which splits it into a reference and measurement beam. Each of these laser beams travels towards a different reflective surface. After being reflected, the two laser beams are joined again at the beam splitter. When the measurement beam strikes the vibrating surface a Doppler frequency shift occurs. At the point of interference, the surface of the photo detector, the reflected measurement beam is described by:

$$E_m(t) = \text{Re} \left(A e^{j(\omega_l t + \omega_d t + \phi(t))} \right) \quad (115)$$

In this equation A is the amplitude of the measurement beam at the point on interference ω_l is the angular frequency of the laser light and ω_d is the Doppler shift. The phase $\phi(t)$ represents the time dependent phase of the measurement beam because the length of the path this beam travels along changes with time. The reference beam can be described by a similar expression. Because the length of the path this wave travels does not change, the phase of this signal is constant. The reference beam striking the surface of the photo detector is described by:

$$E_r(t) = \text{Re} \left(B e^{j(\omega_l t + \phi_r)} \right) \quad (116)$$

Where B is the amplitude of the reference beam at the point of interference, ω_l is still the angular frequency of the laser and ϕ_r is the phase. At the point of interference, the two waves are added:

$$E_t(t) = \text{Re}(E_m(t) + E_r(t)) = \text{Re}\left(Ae^{j(\omega_l t + \omega_d t + \phi(t))} + Be^{j(\omega_l t + \phi_r)}\right) \quad (117)$$

The intensity of interference pattern is equal to:

$$I = \varepsilon_0 c \langle E_t E_t^* \rangle \quad (118)$$

Evaluating this by using (117) results in:

$$I = \text{Re}\left(\left(Ae^{j(\omega_l t + \omega_d t + \phi(t))} + Be^{j(\omega_l t + \phi_r)}\right)\left(Ae^{-j(\omega_l t + \omega_d t + \phi(t))} + Be^{-j(\omega_l t + \phi_r)}\right)\right) = \text{Re}\left(A^2 + B^2 + 2ABe^{j(\omega_d t + \phi(t) - \phi_r)}\right) \quad (119)$$

The real part of the expression in (119) is rewritten as a cosine, which results in:

$$I = A^2 + B^2 + 2AB \cdot \cos(\omega_d t + \phi(t) - \phi_r) \quad (120)$$

The intensity of the interference pattern is indeed modulated by the Doppler frequency shift caused by the motion of the object. Using a measurement setup like this has the issue that it is not possible to detect the direction of the motion of the object. The Doppler shift generated by a motion towards the beam-splitter is equal but opposite to the Doppler shift generated by a motion away from the beam-splitter. Because a cosine is an even function, this results in an equal amount of modulation of the intensity of the interference pattern.

This direction detection issue is solved by placing a Bragg cell in the path of the reference beam. A Bragg cell is an acoustic-optic modulator which shifts the frequency of the light passing through by the drive frequency of the Bragg cell. The Bragg cell in the Polytec setup shifts the frequency of the laser light in the reference beam from ω_l to $\omega_l + \omega_b$ hence the reference beam at the point of interference is written as:

$$E_r(t) = B\left(e^{j(\omega_l t + \omega_b t + \phi_r)}\right) \quad (121)$$

Since the equation for the measurement beam (115) is not affected, the intensity of the resulting wave at the point of interference is written as:

$$I = \text{Re}\left(A^2 + B^2 + 2ABe^{j(\omega_b t + \omega_d t + \phi(t) - \phi_r)}\right) \quad (122)$$

$$I = A^2 + B^2 + 2AB \cdot \cos(\omega_b t + \omega_d t + \phi(t) - \phi_r) \quad (123)$$

If a velocity towards the beam-splitter is defined as positive, the frequency shift is positive and the Doppler frequency ω_d is added to the Bragg frequency ω_b . When the velocity of the object is negative the Doppler shift ω_d is subtracted from the Bragg frequency ω_b . Now the modulation frequency of the intensity of the laser light at the point of interference is dependent on the direction of the motion of the object.

To accommodate the Bragg cell, the Michelson setup [Fig. 5-2] is modified. Extra optics are necessary to guide the light through the Bragg cell onto the photo detector [Fig. 5-3]. The laser beam is split into a reference and measurement beam by beam-splitter bs1, the reference beam travels via the prism, the Bragg cell and beam splitter bs3 directly to the photo detector. The measurement beam coming from bs1 travels through beam-splitter bs2 to the object of interest. It is reflected back towards beam-splitter bs2 and reflected to beam-splitter bs3. It travels through beam-splitter bs3 towards the photo detector as well. Despite the more complex optical arrangement, the operating principle of this setup is equal to that of the more simple one discussed above.

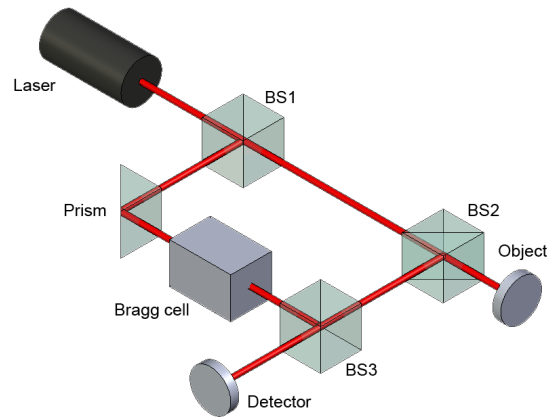


Fig. 5-3: Michelson setup with directional sensitivity

The Polytec MSA 400 used for the experiments comes with a dual fiber vibrometer which enables differential measurements using any surface as reference. The reference beam is not directly projected onto the photo detector but coupled into one of the two optical fibers. This enables the user to project it on any surface to act as a reference, for instance the surface of the viscous coupling chip. It is still possible to do an absolute measurement by terminating the reference fiber with a special mirror attachment.

Using the dedicated software on the vibrometer setup, Fourier analysis is applied to the measurement data and the deflection amplitudes are calculated. The magnitude of the deflection and/or velocity at a certain frequency can subsequently be determined.

5.4 Loudspeaker calibration

In the acoustic experiments the hair sensors in the structures on the viscous coupling chip are subjected to an airflow generated by a loudspeaker. Because the flow generated by a loudspeaker is unknown, an experiment is needed to characterize this flow. From the near field theory, discussed in paragraph 2.10 is known, that the velocity of the air close to a vibrating surface is nearly equal to the velocity of that surface. The distance to the vibrating surface for which this is true depends on the size of the vibrating surface. The membrane of a loudspeaker is usually cone shaped, to create a flat surface, a four inch wafer supported by Styrofoam is fitted to the cone of the speaker. This speaker is now calibrated by measuring the velocity of the wafer attached to the speaker using a laser vibrometer. The loudspeaker is positioned under the scanning head of the Polytec setup with the wafer attachment facing up. The loudspeaker is bolted down onto a 30 mm PVC sheet which stabilizes it and also keeps it in position [Fig. 5-4].

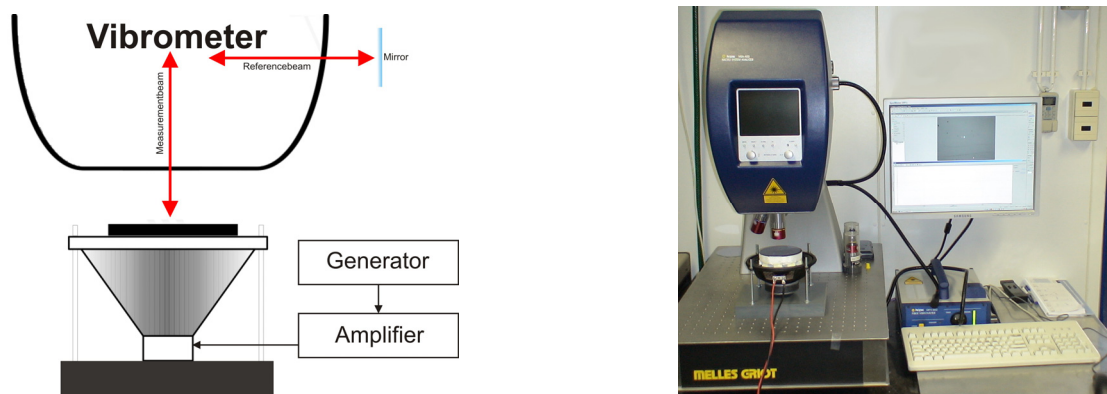


Fig. 5-4: Left: schematic of loudspeaker calibration setup. Right: Photo of the actual setup used in the calibration experiments.

The sheet of PVC serves a dual purpose, besides stabilizing the speaker, it also avoids magnetic attraction between the loudspeaker and the metal table of the Polytec setup. This magnetic attraction influences the magnetic field within the air-gap of the speaker. In this air-gap a coil attached to the speaker membrane is present. The motion of the membrane is generated by forcing a current through this coil. The magnetic field induced by the current through the coil is either repelled or attracted by the magnetic field of the permanent magnet, hence inducing a vibrating motion. When the magnetic field of the permanent magnet in the air-gap is influenced, the current needed to generate a certain velocity of the membrane alters. In the acoustic experiments on the viscous coupling platform the speaker is fitted in a nonferrous metal clamp preventing magnetic attraction. The PVC sheet between the speaker magnet and the metal table reduces the magnetic attraction considerably compared to the attraction experienced without any shielding.

The modified loudspeaker is driven by a single frequency sine wave supplied by a wave generator (HP 33120A). This sine wave is amplified (+4 dB) using a Philips PM 5175 DC to 10 MHz amplifier. The laser vibrometer is configured for absolute velocity measurements, so the fiber carrying the reference beam is terminated by its mirror attachment. The measurement beam is projected at the center of the wafer attached to the speaker. In the viscous coupling characterization experiments, the chip containing the hair sensor structures is positioned in front of the center of this membrane.

Several calibration experiments are conducted because the result of the acoustic experiments indicated issues with the flow source, different methods of calibration are used. Data of all those experiments is discussed in the next section. To avoid confusion the calibration methods are numbered, these numbers are referred to in the discussion of the results of the acoustic experiments.

In calibration experiment one, the speaker is calibrated by keeping the voltage supplied to the amplifier constant at $0.75 V_{pp}$ for all frequencies and measuring the velocity of the membrane. The result of this experiment is then used to normalize the data gathered during the acoustic viscous coupling experiments where the deflection measured is multiplied by the reciprocal of the velocity of the loudspeaker [Fig. 5-5 Left]

In calibration experiment two, the velocity of the speaker membrane is kept constant by adjusting the drive voltage. This experiment is conducted in two steps, first the velocity of the membrane is measured for many different drive voltages and frequencies. This data is used as a guide in the second step. By changing the amplitude of the drive voltage, the velocity of the speaker membrane is adjusted. Characterization using this constant velocity method is done for three different velocities, 10 mm/s, 20 mm/s and 30 mm/s for frequencies between 10 Hz and 1200 Hz [Fig. 5-5 Right].

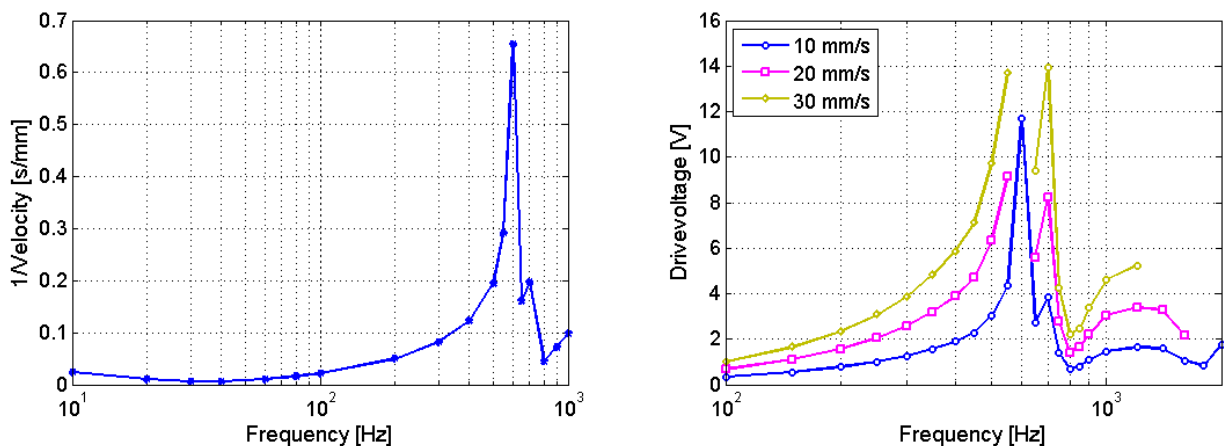


Fig. 5-5: Result of loudspeaker calibration, Left: reciprocal of the velocity of the loudspeaker membrane versus frequency at a constant drive voltage of $0.75 V_{pp}$. Right: Drive voltage versus frequency for different flow velocities.

A third calibration experiment is conducted because measurements across the wafer attached to the loudspeaker indicated large variations in its velocity across its surface. Until now, the wafer attached to the speaker is only supported in its center to keep the weight of the attachments down to a minimum. Measurements at the unsupported edge of the wafer proved that the velocity at the edge of the wafer, at a frequency of 600 Hz, was up to twenty times larger than the velocity measured at the center of the wafer. This velocity gradient is reduced by adding extra supporting foam to support the outer edge of the wafer. Adding this extra support increases the mass of the moving parts, changing the characteristics of the speaker. Again the speaker is calibrated by adjusting its drive voltage to keep the velocity of the membrane constant. Again the speaker is calibrated for velocities of 10 mm/s, 20 mm/s and 30 mm/s [Fig. 5-6]. The drive voltages measured in this experiment are used to set the flow in the acoustic viscous coupling experiments.

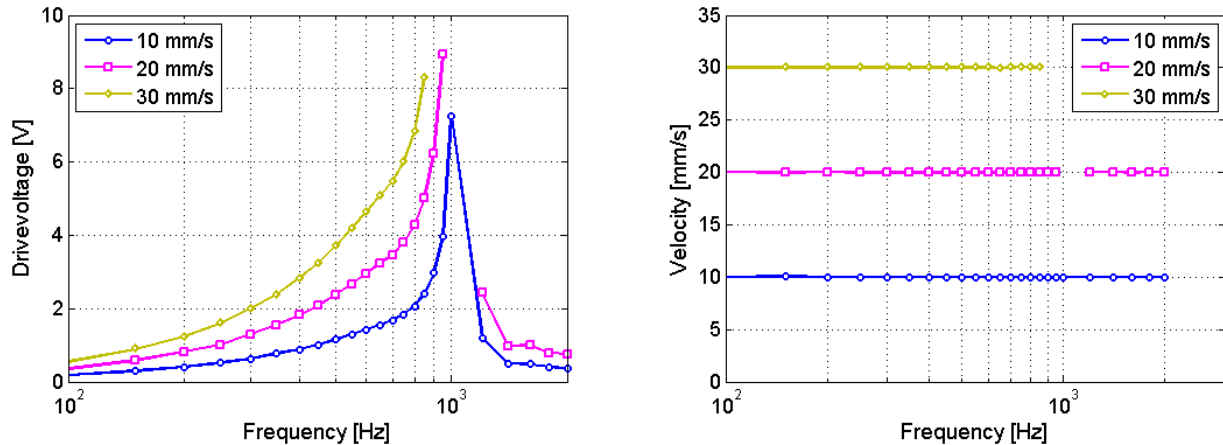


Fig. 5-6: Calibration results of the third calibration experiment. Left: drive voltage vs. frequency for different velocities of the membrane. Right: velocity, measured at the drive voltages displayed in the left graph versus frequency.

5.5 Acoustic experiments and results

To characterize the viscous coupling between the hair sensors during normal operation, the different hair sensor structures are subjected to an airflow. To study the presence and characteristics of these effects, experiments are conducted using a loudspeaker as a flow source. This loudspeaker is calibrated in the three calibration experiments discussed in section 5.4.

To characterize the viscous coupling between the hair sensors, the deflection of the hair sensor membrane is measured using a laser vibrometer. The chip containing the different sensor structures is positioned under the scanning head of the Polytec setup, which contains the fiber vibrometer [Fig. 5-7]. The chip is fitted onto a PCB which is glued to the end of a brass strip. The other end of the strip is attached to a rotation table. This rotation table can be shifted horizontally in two directions for easy access to each of the different structures on the chip [Fig. 5-7].

The deflection of the hair sensor membranes is measured by focusing the measurement beam of the laser vibrometer on the outer edge of the electrodes on the membrane. Using the Polytec scanner software, scan-points are defined on the edge of the electrodes on the membrane, since the deflection is maximum there. This also ensures that measurements are taken at the same position at all different frequencies. Defining multiple scan-points on each side of the membrane enables averaging to get a more reliable result. Depending on the position of the scan-points, a modal decomposition by averaging in a more specific way is obtained. This modal decomposition method is discussed separately in section 5.7. To be able to measure the velocity of the hair sensor membranes with respect to the surface of the chip, the reference beam is focused on the wiring on the chip. The Polytec scanner software determines the deflection of the membrane using the velocity measurement data provided by the vibrometer.

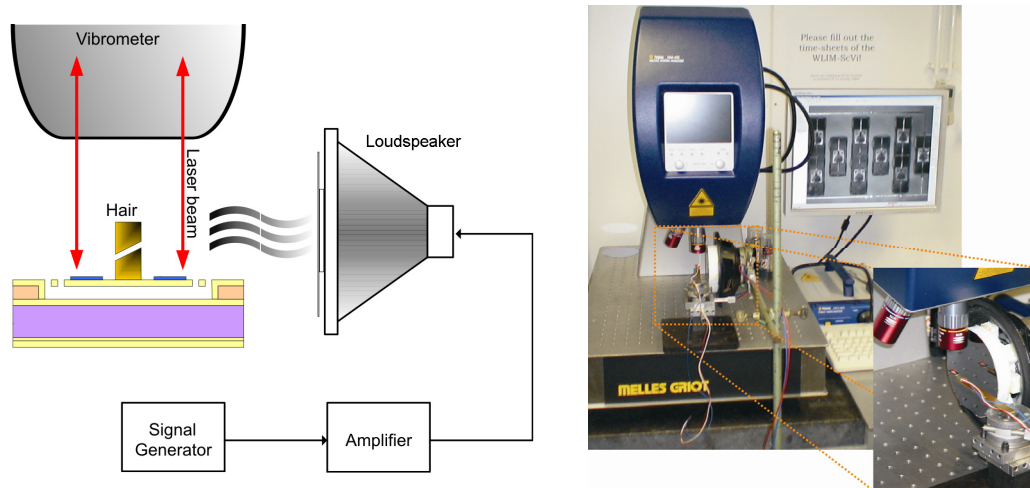


Fig. 5-7: Left: schematic of the acoustic characterization setup. Right: photo of the actual setup, the chip in front of the flow source.

The calibrated loudspeaker is positioned very close to the chip. The condition for the very near field as described in section 2.10 indicates that the hair sensors needs to be within 16 mm of the flow source to be in the very near field of the loudspeaker used. In practice, the sensor structure of interest is at a distance of 20 mm from the speaker membrane. The size of the loudspeaker and the diameter of the optics on the scanning-head of the vibrometer prevent the speaker from being closer to the sensors. The loudspeaker itself is fitted by a clamp attached to a separate stand on the floor to prevent vibrations in the vibrometer setup.

The settings of the vibrometer are kept constant during the experiments, the bandwidth is set to 2 kHz ranging from DC to 2 kHz. The number of FFT lines is set to 3200, this setting determines the number of lines in the calculated FFT spectrum. Using the setting 3200, a FFT line is calculated every 625 mHz. The average magnitude of three measurements on a single point is used as the measured value. The window function is set at rectangle. An external wave generator is used (HP33120A), so the triggering option is set to external. The sensitivity of the vibrometer is set at 5 mm/s/V. A low pass filter of 1.5 MHz is used and the high pass filter option is set to off as this is recommended when using the setup in scanning mode.

Results

The current hair sensor design, has never before been realized using the fabrication process discussed in section 4.2. The acoustic experiments first focused on the hair sensors in a row. In these structures, a dominant parameter, the separation S between the sensor is varied.

The dedicated experimentation platform contains twelve rows of three sensors divided into six groups of two structures. In each of the six groups the separation between the hair sensors is different. The experiments focused on four rows having separations of 150 μm , 200 μm , 300 μm and 400 μm (Inline-150 μm , Inline-200 μm , Inline-300 μm and Inline-400 μm [Appendix A]).

A set of experiments is conducted using a constant voltage of 0.75 V_{pp} supplied to the amplifier driving the speaker. The data gathered in these experiments is normalized by the velocity values measured in calibration experiment one.

Depending on the magnification of the objective attached to the scanning head of the vibrometer, two row structures are visible at the same time [Fig. 5-8]. If that is the case, the deflection of the sensors in these structures is measured in a single experiment. The vibration of the substrate is, in that case, measured at a position between the two structures. For a more accurate measurement, three scan-points are defined on the upstream side of each hair sensor [Fig. 5-8]. The deflection of the substrate is measured at three different points as well.

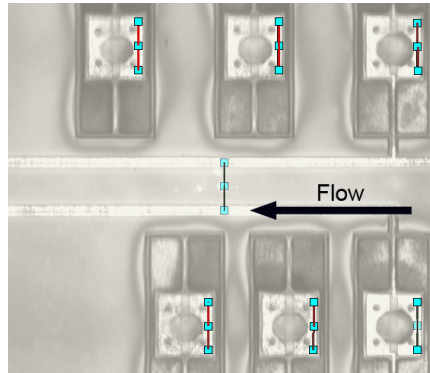


Fig. 5-8: Position of scan-points during first set of experiments.

The deflection of each of the scan points is calculated by the scanner software. The scanner software calculates the FFT spectrum of the measurement data and the magnitude of the deflection at the frequency of the loudspeaker is extracted from this FFT data. The average of the measured deflections of the three scan-points on a sensor is used as the measured value for the deflection. The deflection angle of the membranes is calculated and divided by the flow velocity generated by the speaker, the resulting data is displayed in graphs [Fig. 5-9]. The data measured on the substrate is treated like this as well, so being able to be displayed in the same graphs.

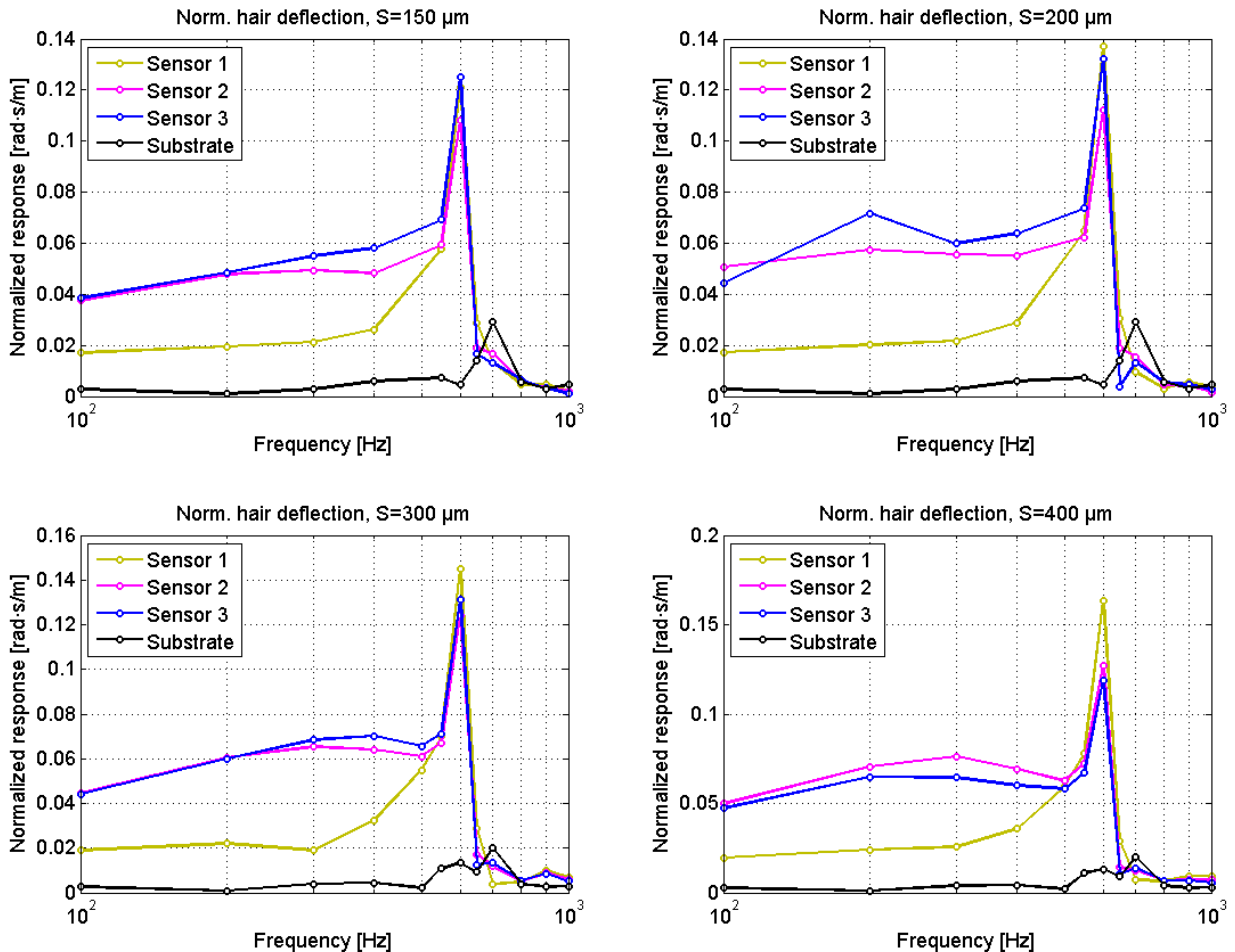


Fig. 5-9: Normalized results of measurements on three hair sensors in a row ('Inline' row series). Upper left: separation of 150 μm (Inline-150 μm), Upper right: separation of 200 μm (Inline-200 μm). Lower left: separation of 300 μm (Inline-300 μm). Lower right: separation of 400 μm (Inline-400 μm).

The data [Fig. 5-9] proves that the sensors are in motion at the driving frequency of the loudspeaker. It is quite remarkable however, that in all four row structures the deflection amplitude of the second and third sensor is larger than the deflection amplitude of the first sensor in the same row. Increasing the separation between the sensors appears to affect the amplitude of the second and third sensor, especially at the peak in the graphs at 600 Hz. For frequencies higher than 600 Hz the deflection of the sensors decreases very fast and is similar to the amplitude measured on the substrate.

Since the velocity is measured with respect to the substrate, it is expected that the velocity of the substrate would be minimal. The actual deflection values measured on the substrate are the result of a combination of real substrate vibrations as well as mechanical and electrical noise in the measurement setup.

The deflection data for the first sensor in each of the four row structures is relatively consistent, the variations in this data are probably caused by minor geometrical differences between these hair sensors.

The difference in the deflection amplitude between the sensors on the first row and the sensors on the second and third row can also be explained by the difference in their design. The hair sensor on the first row of the 'Inline' row structures can be actuated. To be able to charge the capacitors, it has aluminum wires running over its suspension beams, this is not the case in the design of the other hair sensors in the 'Inline' row structures. The presence of these metal lines affects the torsion stiffness of the beams which affects the behavior of the sensor.

Measurements on this type of structures on a different chip show a similar result [Fig. 5-10]. The sensors on this chip show deflections with a lower amplitude compared to the sensors on the chip used in the previous experiment. Since the fabrication process is never uniform between separate wafers or across the surface of a single wafer, variations in the specifications of the hair sensors do occur.

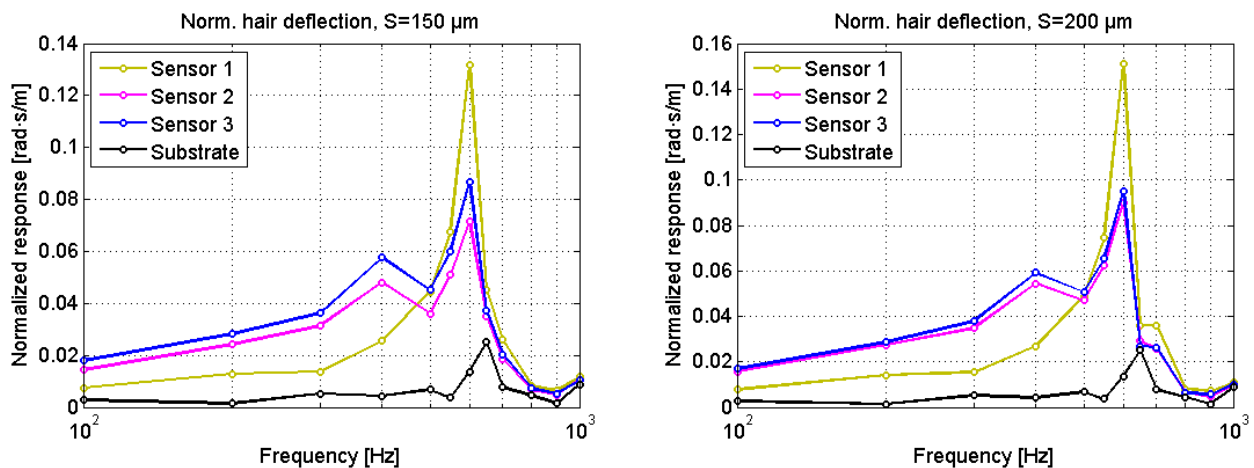


Fig. 5-10: Normalized results of measurements on hair sensors in a row ('Inline' row series). Left: separation of 150 μm (Inline-150μm) Right: separation of 200 μm (Inline-200μm).

Since the shape of the graphs presented so far is showing resemblance to the loudspeaker characteristic [Fig. 5-5 Left], new experiments are conducted using a constant flow velocity. The drive voltage of the speaker is set to the values gathered in loudspeaker calibration experiment two. The flow is now kept at 10 mm/s and 30 mm/s, the deflection of a pair of hair sensors is measured as a function of different frequencies. The experiments focused on the two sensors on the first line of a couple of adjacent 'Inline' row structures, so both sensors have metal lines running over their suspension beams.

Since the flow is kept at a constant velocity, now the actual deflection determined by the laser vibrometer is displayed for different frequencies [Fig. 5-11]. Again the measured data shows a peak at about 600 Hz as was the case in the previous experiments. Since no resonance is expected at a frequency of 600 Hz, the source of the flow is tested once again.

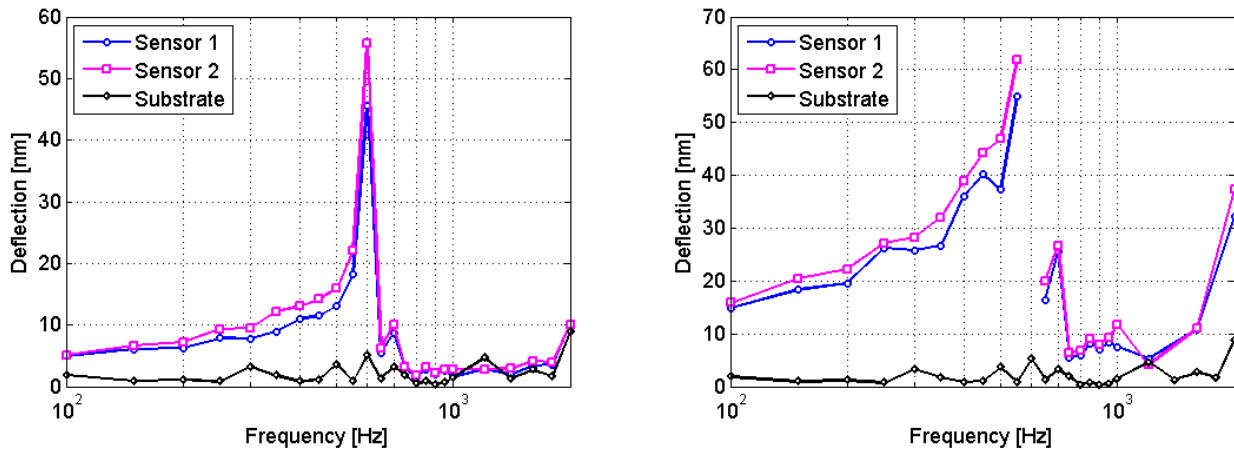


Fig. 5-11: Hair sensor deflection of two adjacent hair sensors, sensor 1 is the first sensor in an 'Inline-150 μ m' structure and sensor 2 is the first sensor in the 'Inline-200 μ m' structure next to it. Left: flow-velocity of 10 mm/s, Right: flow velocity of 30 mm/s, a flow of 30 mm/s could not be generated at 600 Hz

Since there is still the unexpected peak at 600 Hz, the flow source is inspected again. As discussed in section 5.4, measurements indicated a large velocity gradient across the surface of the loudspeaker membrane at 600 Hz. The issue was solved and again new acoustic experiments are conducted, this time setting the drive voltage according to the data gathered in calibration experiment three.

A new experiment focused on a solo sensor. The deflection of its membrane is measured, applying a flow of 10 mm/s at different frequencies. Since all sensors are arranged in structures, possible coupling due to presence of other sensors is avoided by removing them carefully [Fig. 5-12]. The deflection measurement is still with respect to the substrate although the deflection of the substrate itself is not measured.

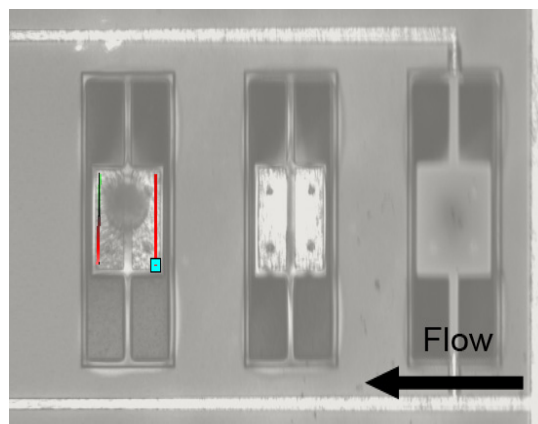


Fig. 5-12: Optical microscope image of an 'Inline-150 μ m' sensor structure with sensors one and two removed. The direction of the oscillating flow is indicated by the arrow.

The deflection on both the upstream and downstream side of the sensor is measured at three different points. The deflection values of the three points on each side are averaged and the result is displayed in a graph [Fig. 5-13]. This graph shows two lines roughly having the same shape, but indicating a small difference between the deflection of the two sides of the membrane. There are several probable causes for this. The measured deflection is dependent on the distance of the scan-points to the tilt axis. Since the scan-points are defined and positioned by hand, it is very likely the deflection is not measured at exactly the same distance from the tilt axis. The position of the hair might also play a role in this. The position of the hair itself and the alignment of the two parts of the hair might also have an effect on the deflection of the sensor. The image of the hair sensor [Fig. 5-12] indicates that the hair of the sensor in question is not perfectly centered, however it appears to be right on top of the expected tilt axis of the hair sensor. These alignment problems occur during fabrication, the relative large thickness of the SU-8 layer necessary to fabricate the hairs complicates the exposure process, a probable cause of these issues

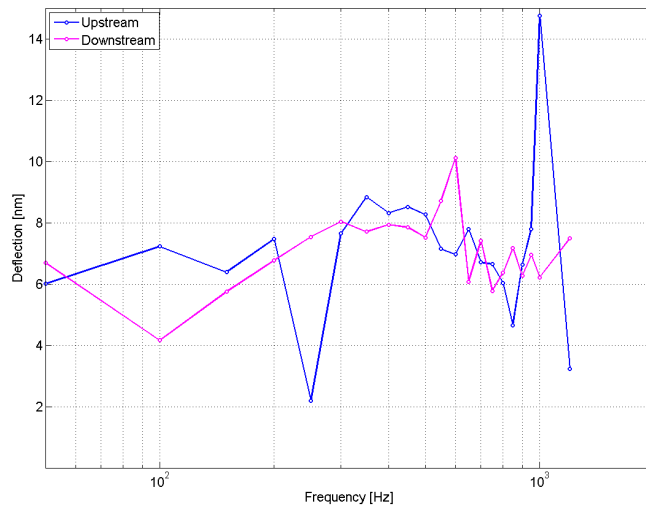


Fig. 5-13: Deflection of the two sides of the membrane of a single hair sensor as a function of frequency. It concerns the third hair sensor in an 'Inline-150 μ m' structure with sensor 1 and sensor 2 being removed.

A different experiment is conducted on a pair of hair sensors separated by 400 μ m. In this case it concerns sensors two and three within a 'Inline-400 μ m' row structure. In this structure, sensor 1 is removed, leaving two sensors with the same specifications in the structure [Fig. 5-14]. The deflection of both sides of the sensors is measured at three different points. The flow is set at a constant 10 mm/s using data from calibration experiment three. The average deflection of the three points on the upstream side of each sensor is displayed in a graph [Fig. 5-14]. The data of the points on the downstream side is used later for a modal decomposition.

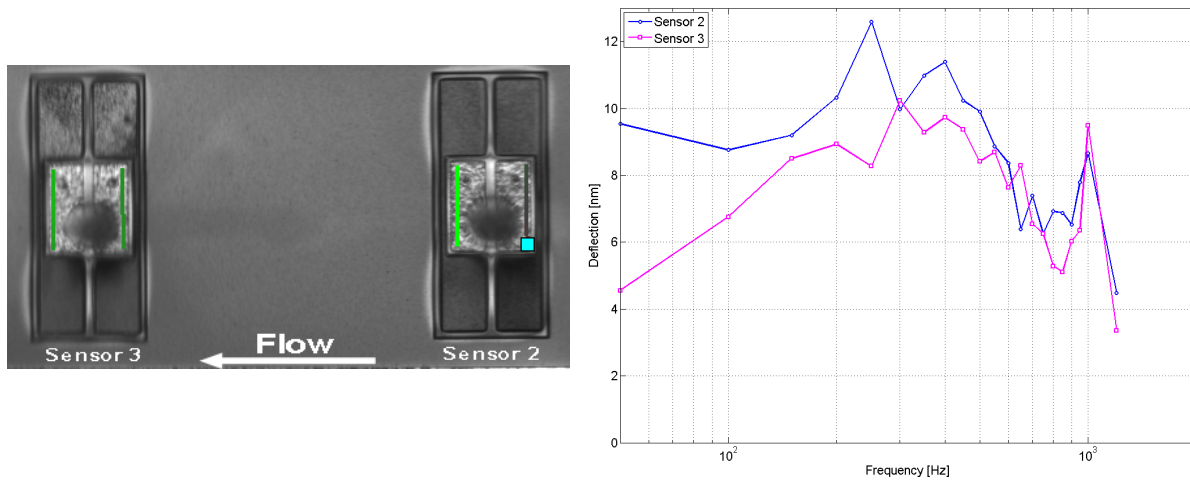


Fig. 5-14: Left: optical microscope image of the structure, 'Inline-400 μ m' with sensor 1 removed. Right: deflection of the two sensors, sensor 2 and sensor 3 using a flow of 10 mm/s at different frequencies.

At lower frequencies there is a difference of about 5nm between the two sensors, however this difference decreases as the frequency of the flow increases. Viscous effects could play a role here, however the image [Fig. 5-14] indicates that the hairs on these two sensors are not perfectly aligned with respect to their membrane. The center of the hair on the sensor on the right appears to be above the torsion axis while the hair on the left sensor seems to be off by a few microns. This alignment issue could also explain these results.

The results of all these acoustic experiments indicate that it is possible to extract deflection data of individual sensors in a structure using a laser vibrometer. The results of the early experiments using the speaker at a constant voltage showed effects that could be based on viscous coupling. But since results on a solo sensor under these circumstances are not available this remains unknown. Variations in the fabrication process and processing conditions all contribute to different deflection values measured between different sensors and different chips. This makes comparing results between structures and between chips rather difficult.

5.6 Electrostatic experiments and results

The effect of hair sensor motion itself on other hair sensors is studied by actuating certain hair sensors by alternately charging their capacitors. In each structure there is one particular sensor that can be set in motion. Detailed information about this is available in the device reference list [Appendix A]. The hair sensors are set in motion by applying a combination of AC and DC voltage to the electrodes on the membrane. Applying a combination of AC and DC voltage to one of the electrodes already results in a tilting motion. Besides the basic mode at frequency f , using single sided actuation will trigger a second order mode. The power to the sensor using single sided actuation is equal to:

$$P_{\text{single}} = (DC + AC \sin(2\pi ft))^2 = DC^2 + 2 \cdot AC \cdot DC \cdot \sin(2\pi ft) + \frac{1}{2} AC^2 (1 + \sin(4\pi ft)) \quad (127)$$

By applying voltage to both electrodes, provided the AC parts are 180° out of phase, only the mode at frequency f is triggered. The power to the sensor is then equal to:

$$P_{\text{double}} = (DC + AC \sin(2\pi ft))^2 - (DC - AC \sin(2\pi ft))^2 = 4AC \cdot DC \sin(2\pi ft) \quad (128)$$

The substrate is grounded while the two electrodes on top of the membrane are supplied with the voltage signals. In the experiments, this voltage is supplied by a dual channel wave generator (HP 3245A) capable of generating two AC signals having a constant phase delay (180°) [Fig. 5-15 Left] The deflection of the sensor membranes is again measured using a laser vibrometer. The chip with the sensors structures is wire-bonded to a PCB. This PCB is wired to the wave generator and positioned under the scanning head of the vibrometer setup [Fig. 5-15 Right].

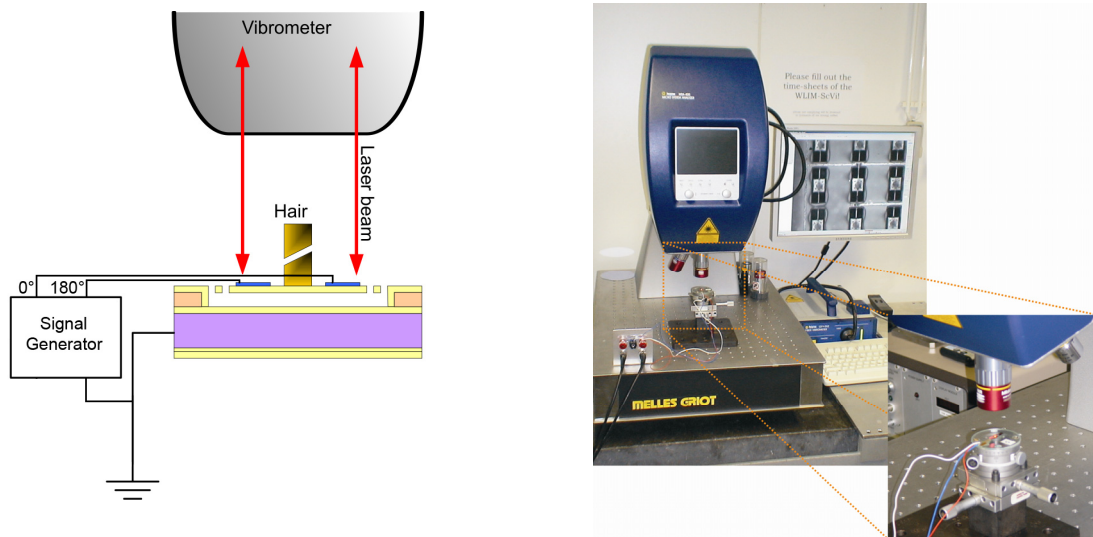


Fig. 5-15: Electrostatic measurement setup. Left: schematic overview of the setup used in the electrostatic experiments. Right: photo of the actual setup, the chip on a pcb fitted to a rotation table capable of being moved horizontally in two directions.

Electrostatic analysis in section 2.9 indicates that the theoretical pull-in voltage for vertical pull-in is 2.93V. To be on the safe side an AC voltage of $0.3 V_{pp}$ with an offset of 0.175 V DC is supplied to the hair sensor. The experiments focused on a the 'Inline' series of sensors in a row. The deflection of the sensor membranes with respect to the substrate is measured at three different point on the membrane. The deflection of the substrate with respect to itself is measured as well. The data gathered from the 'Inline' structures with separations of 150 μm , 200 μm and 300 μm is averaged and displayed in graphs [Fig. 5-16]. The deflection data of the three actuated sensors is displayed in a separate graph on a linear scale to compare the deflection values between actuated sensors. The deflection of the three actuated hair sensors is between six and ten nanometer. The deflection of the other sensors in the three 'Inline' row structures is of the same magnitude as the deflection measured on the substrate.

In each of the three 'Inline' row structures, the second and third hair sensor did not indicate any flow effect induced by the motion of the actuated hair sensor. Either there is no effect or the effect is so small that it cannot be distinguished from the noise in case the measurement sensor is at a distance of 150 μm or more from the actuated sensor.

In this case all measurements are conducted on structures on a single chip, the data in the lower right graph [Fig. 5-16] shows that there can be quite some difference in the response between sensors having the same specifications on a single chip.

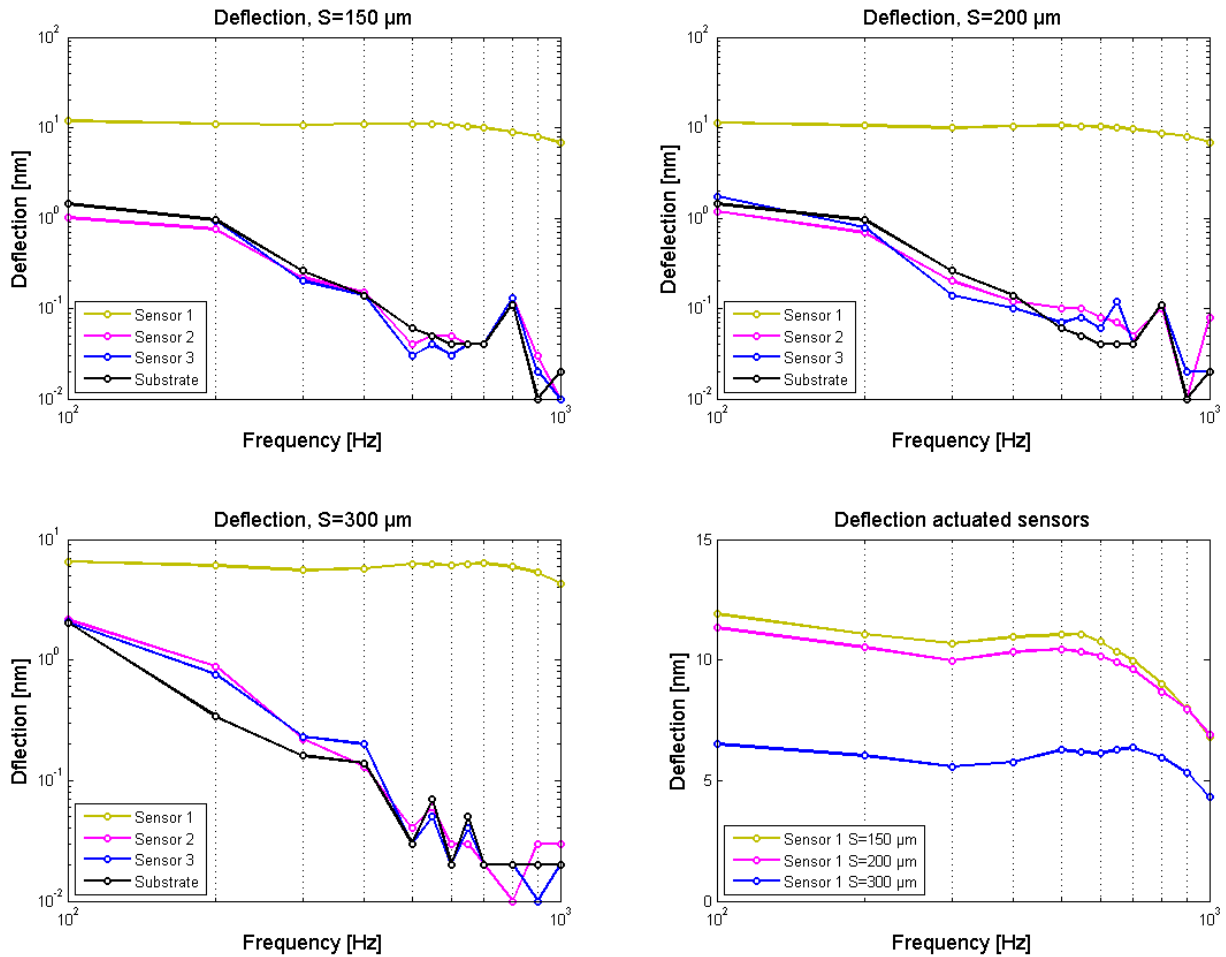


Fig. 5-16: Results on electrostatic measurements. Upper left: row of sensors, separation 150 μm ('Inline-150 μm '). Upper right: row of sensors, separation 200 μm ('Inline-200 μm '). Lower left: row of sensors, separation 300 μm ('Inline-300 μm '). Lower right: Deflection of the first sensors in 'Inline-150 μm ', 'Inline-200 μm ' and 'Inline-300 μm '.

Comparing results of these electrostatic experiments with the results of the acoustic experiments indicates that the clear peak at 600 Hz as seen in some of the acoustic experiments was caused by the loudspeaker.

5.7 Modal decomposition

Just like a vector in a coordinate system is the sum of a number of basic vectors, the motion of the hair sensors can be dissected into different specific motions as well. In section 2.8, three of these specific types of motion are already introduced. In the torsion mode, the sensor membrane tilts about the axis of the suspension beams [Fig. 5-17 A]. Besides the torsion mode, there is the vertical mode in which the sensor moves vertically up and down [Fig. 5-17 B]. In the transversal motion, the hair sensor is tilting sideways [Fig. 5-17 C]. The suspension beams are now alternately bending up and down. In the fourth mode, the diagonal mode, two corners on the same diagonal of the membrane are moving upwards while the other two corners of the membrane move down [Fig. 5-17 D].

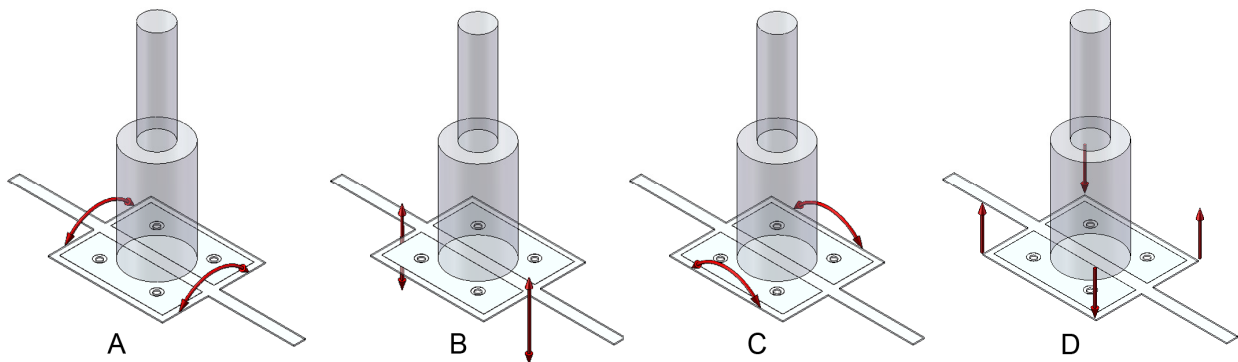


Fig. 5-17: Four different modes of operation, A) torsion , B) vertical, C) transversal, D) diagonal

Using the measurement data from at least four scan-points, the motion of the hair-sensor can be dissected into these four different modes. In the calculation of the amplitudes of the four different modes, a symmetric sensor is assumed. Deviations in symmetry occur for instance when the hair is not perfectly straight or when the hair is not in the center of the membrane. Asymmetry affects the motion of the sensor therefore the resulting amplitude of each of these modes can deviate from its real amplitude.

Depending on the mode of interest, the number and location of the scan-points, the amplitude of the mode is calculated by adding, subtracting and averaging the measurement data. Using scan-points on the four corners of the membrane [Fig. 5-18], the four modes can be calculated using the equations listed in [Tab. 5-1]. For more accuracy extra scan-points can be defined however adjusting the modal equations is required as well.

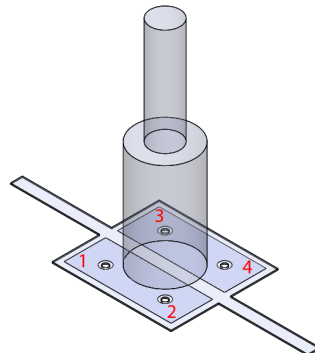


Fig. 5-18: Position of the four scan-points (flow coming from the lower left corner).

Mode	Formula	Mode	Formula
Torsion	$\frac{sp1+sp2-sp3-sp4}{4}$	Transversal	$\frac{sp1-sp2+sp3-sp4}{4}$
Vertical	$\frac{sp1+sp2+sp3+sp4}{4}$	Diagonal	$\frac{sp1-sp2-sp3+sp4}{4}$

Tab. 5-1: Equations for modal analysis

In two of the acoustic experiments discussed in section 5.5, the deflection of each side of the sensor was measured at three points. The measurement data of these points is used to split the motion of the sensor into the four modes discussed above. The data of all six points is only used in the calculation of the torsion mode and the vertical mode. For these modes, the expressions listed in the table are adjusted appropriately [Tab. 5-1]. For the transversal and diagonal mode only the deflection data at the four corners of the membrane is used.

The results of a modal decomposition on the motion of a solo sensor show that the torsion mode has a relatively constant amplitude compared to the other three modes, this mode is clearly preferred [Fig. 5-19 Left]. The results also indicate that the vertical mode is preferred to the

transversal and diagonal one. These two modes show a similar amplitude which is about an order of magnitude lower than the amplitude of the torsion mode. The amplitudes of the vertical, transversal and diagonal mode appear to decrease with frequency, however at 850 Hz the amplitudes of these modes starts to rise again. The measurement data used for this decomposition shows a major increase in the average deflection of the three points on the upstream side of the sensor at that frequency [Fig. 5-19 Right]. The average amplitude of points on the downstream side remains behind however. This might explain the sudden increase in the amplitude of the vertical, transversal and diagonal mode. The original data of the three points on the upstream side of the membrane indicates the sudden increase at 1 kHz is common for all three points, the exact reason for this however remains unknown.

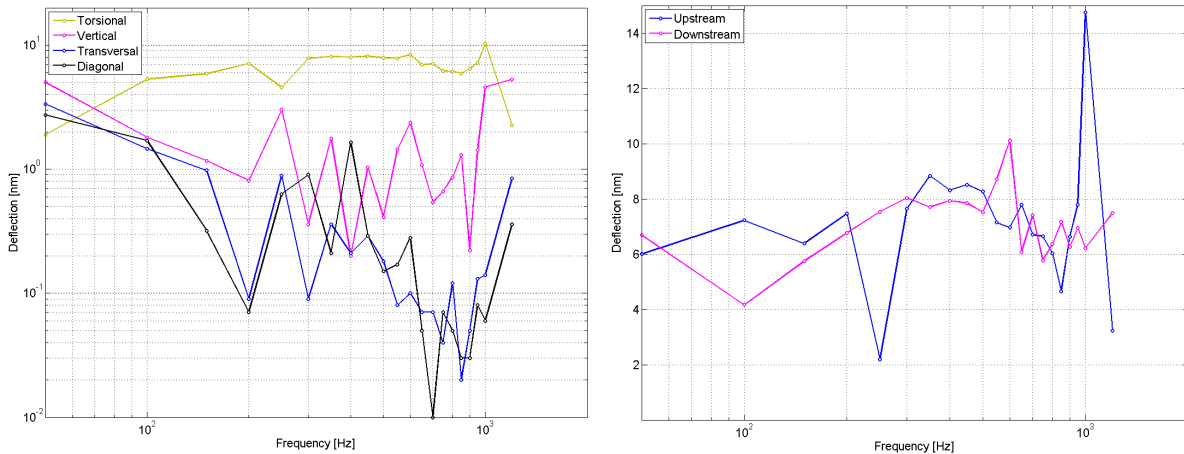


Fig. 5-19: Left: modal decomposition of an acoustic measurement on a solo sensor (10 mm/s). Right: average deflection of the two sides of the sensor in an acoustic experiment at 10 mm/s

A modal decomposition of the data on two hair sensors separated by 400 μm shows a similar result [Fig. 5-20]. The amplitude of the torsion modes of these two sensors here is larger compared to the solo sensor. It is an order of magnitude higher compared to the other modes. Also here, the vertical mode indicates a preference to the diagonal and transversal modes. The data on these sensors as well as the data on the single sensor show a decrease in the torsion mode at about 1 kHz. Since no data is available for higher frequencies it is unknown if this decrease continues.

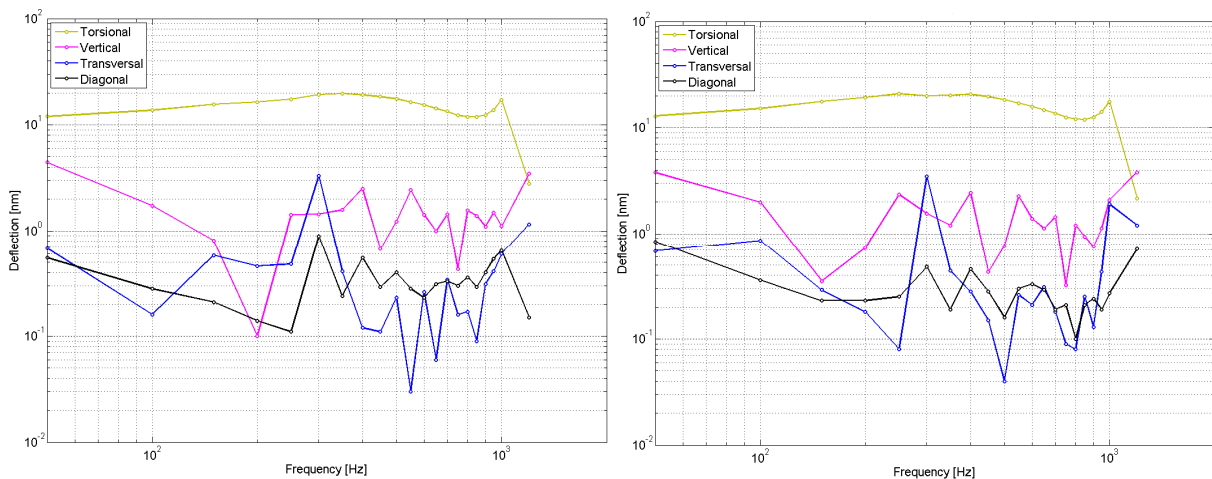


Fig. 5-20: Modal decomposition of two sensors with a separation of 400 μm . Sensor 1 has been removed in this experiment. Left: modal decomposition of sensor 2. Right: modal decomposition of sensor 3.

6 Conclusions

The MEMS fabrication steps of the new generation of bio-inspired hair sensors were used to design and realize an experimentation platform to characterize the viscous coupling effects between adjacent hairs. The hair sensor design is adapted to accommodate the requirements of the viscous coupling research. The experimentation platform was successfully realized by the cleanroom technicians and inspection of the devices only revealed a few minor issues related to mask design which can be easily solved in future designs.

By means of various characterizations, the modified sensors were found to be capable of detecting flow perturbations. Using a laser vibrometer setup, the motion of the individual sensors is easily picked up and the magnitude of the membrane deflection is measured optically. The hair sensors were subjected to the near-field, flows from a loudspeaker. Increasing the distance between sensors in a row, resulted in a reduced deflection amplitude of the second and third sensors in the rows. However it remains unsure if this observation is caused by viscous effects.

Managing the flow conditions during the different acoustic experiments is quite a challenge; even though the flow-source, a loudspeaker, is calibrated several times, still the frequency transfer characteristic of the hair sensors is not clear.

In the experiments where a hair sensor was set in motion by electrostatic forces, no considerable viscous coupling effects were observed on adjacent sensors in the same row. It is noteworthy to mention that deflection range of these hair sensors was already at the system noise level. Hence, the fact that adjacent hair sensors did not pick up any disturbance does not really prove the absence of viscous coupling effects.

Using the modal decomposition, the motion of the sensors was studied in more detail. Dissecting the motion of a sensor into different components helps to gain knowledge about the actual motion of the sensor. Modal analysis on two acoustic experiments indicated that the torsion mode is preferred to the vertical, transversal and diagonal mode. This preference starts to decrease at frequencies around 1 kHz.

Due to the limited amount of chips (containing the experimentation platform) available and their limited lifespan, there wasn't enough opportunity to complete the intended experimental characterizations. The presented experiments focused on hair sensors arranged in a row, sensor separation being an important parameter in viscous coupling. Despite the fact that the presence of the viscous coupling effect between the hair sensors is not yet understood, nevertheless a lot of knowledge and constructive insights were gained to improve the design and to continue the work on this subject.

6.1 Future improvements

Design

The current experimentation platform has some design issues that need correction in the future. An important modification is the location of the different structures on the chip. Due to limited space, currently some of the structures are positioned behind each other. The flow is unable to pass these structures without being obstructed by other structures. A second important issue concerns the design of the hair sensors. The current platform contains two types of flow sensors, one with and the other one without metal lines running over its suspension beams. More reliable results can be obtained if the design of all sensor is equal. Hence, it is better to have metal lines running over the beams of all the sensors. The connection to the wiring on the chip can be omitted where desired.

Fabrication

An important issue concerning the fabrication of the experimentation platform is the dicing of the chips. The chips used in the viscous coupling research came in very irregular shapes possibly affecting the airflow. The shape and alignment of the SU-8 hairs on top of the sensors needs some attention as well. Variations in the shape and location of these hairs were observed in the experiments.

Experiments

The source of the flow needs a lot more attention. It is very important the flow over the chip is characterized and known, either by carefully characterizing the flow source or by measuring the flow over the chip using a calibrated flow-sensor.

References

- [1] M.A. Landolfa and J.P. Miller, "Stimulus–response properties of cricket cercal filiform hair receptors", *J. Comp. Physiol. A*, Vol. 177: pp. 749–757.
- [2] R. Levi, J.M. Camhi, "Wind direction coding in the cockroach escape response: winner does not take all", *Journal of neuroscience*, Vol. 20 Nr. 10, pp 3814-3821, May 2000
- [3] T. Shimozawa and M. Kanou, "Varieties of filiform hairs: range fractionation by sensory afferents and cercal interneurons of a cricket", *J. Comp. Physiology A*, vol. 155, pp. 485-493, 1984
- [4] T. Kumagai, T. Shimozawa and Y. Baba, "The shape of the wind-receptor hairs of cricket and cockroach", *J. Comp. Physiology A*, vol.183, pp. 187-192, 1998
- [5] M.A. Landolfa, G.A. Jacobs, "Direction sensitivity of the filiform hair population of the cricket cercal system", *J. Comp. Physiology A*, vol. 177, pp. 759–766, 1995
- [6] W. Gnatzy, J. Tautz, "Ultrastructure and mechanical properties of an insect mechanoreceptor: stimulus transmitting structures and sensory apparatus of the cercal filiform hairs of *Gryllus*", *Cell and tissue research*, Vol. 213, pp. 441–463, 1980
- [7] T. Shimozawa, J. Murakami and T. Kumaga, "Cricket wind receptors: thermal noise for highest sensitivity known", *Sensors and sensing in biology and engineering*, F. Barth, J. Humphrey, T. Secomb, Ed., Berlin: Springer Verlag, 2003, pp. 145-157
- [8] G.J.M. Krijnen, J. Floris, M. Dijkstra, T.S.J. Lammerink, R.J. Wiegerink, "Biomimetic Micromechanical Adaptive Flow-Sensor Arrays", *Proceedings of the SPIE*, Volume 6592, pp. 65920F, 2007
- [9] B. Bathellier, F.G. Barth, J.T. Albert, and J.A.C. Humphrey, "Viscosity-mediated motion coupling between pairs of hairs on the leg of the spider *Cupiennius salei*", *J. Comp. Physiology A*, vol. 191, pp. 733-746, August 2005
- [10] B. Cummins, T. Gedeon, I. Klapper and R.Cortez, "Interaction between arthropod filiform hairs in a fluid environment", *J. Theoretical Biology*, vol. 247, pp. 266-280, July 2007
- [11] T. Shimozawa, T. Kumagai and Y. Baba, "Structural scaling and functional design of the cercal wind-receptor hairs of cricket", *J. Comp. Physiology A*, vol. 183, pp. 171-186, July 1998
- [12] A.C. Humphrey, R.Devarakonda, I. Iglesias and F.G. Barth, "Dynamics of Arthropod Filiform Hairs. I. Mathematical Modelling of the Hair and Air Motions", *Philosophical transactions: Biological sciences*, Vol. 340 No. 1294 pp. 423-444, 1993
- [13] G.G. Stokes, "On the effect of the internal friction of fluids on the motion of pendulums", *Math. Phys. Pap.*, Vol. 3, 1880-1905
- [14] F. Barth, J. Humphrey, U. Wastl, J. Halbritter and W. Brittinger, "Dynamics of arthropod filiform hairs.III. flow patterns related to air movement detection in a spider (*Cupiennius salei* Keys.)", *Philos. Trans. R. Soc. London*, Ser. B, vol. 347 pp. 397-412
- [15] T. Shimozawa and M. Kanou, "The Aerodynamics and sensory physiology of range fractionation in the cercal filiform sensilla of the cricket *Gryllus bimaculatus*", *J. Comp. Physiology A*, vol. 155, pp495-505, July 1984
- [16] T. Steinmann, J. Casas, G. Krijnen and O.Dangles, "Air-flow sensitive hairs: boundary layers in oscillatory flows around arthropod appendages", *J. experimental biology*, Vol. 209 pp. 4398-4408, 2006

- [17] H. Schlichting, "*Boundary layer Theory*", 7th ed. J. Kestin. New York, McGraw-Hill, 1979, pp. 93-95, 135-141.
- [18] W. Young and R. Budynas, "*Roarks formula's for stress and strain*", 7th ed. New York McGraw-Hill, 2002, Ch 10.
- [19] E. Saucedo-Flores, R. Ruelas, M. Flores and J. Chiao, "Study of the pull-in voltage for MEMS parallel plate capacitor actuators", *Mat. Res. Soc. Symp. Proc.*, Vol. 782, 2004
- [20] H.E. de Bree, V.B. Svetovoy, R. Raangs and R. Visser, "*The very near field theory, simulations and measurements of sound pressure and particle velocity in the very near field*", ICSV11, St. Petersburg, 2004

A. Appendix , Device reference list

In this appendix the details of the different sensor structure designs are discussed. This appendix acts as a reference guide for the different names of the structures and the numbers of the sensors in these structures. The reference numbers of the sensors are shown in images of the mask designs. As an example the design of a regular hair sensor is displayed together with the set of masks that is necessary to fabricate this sensor [Fig. A-1].

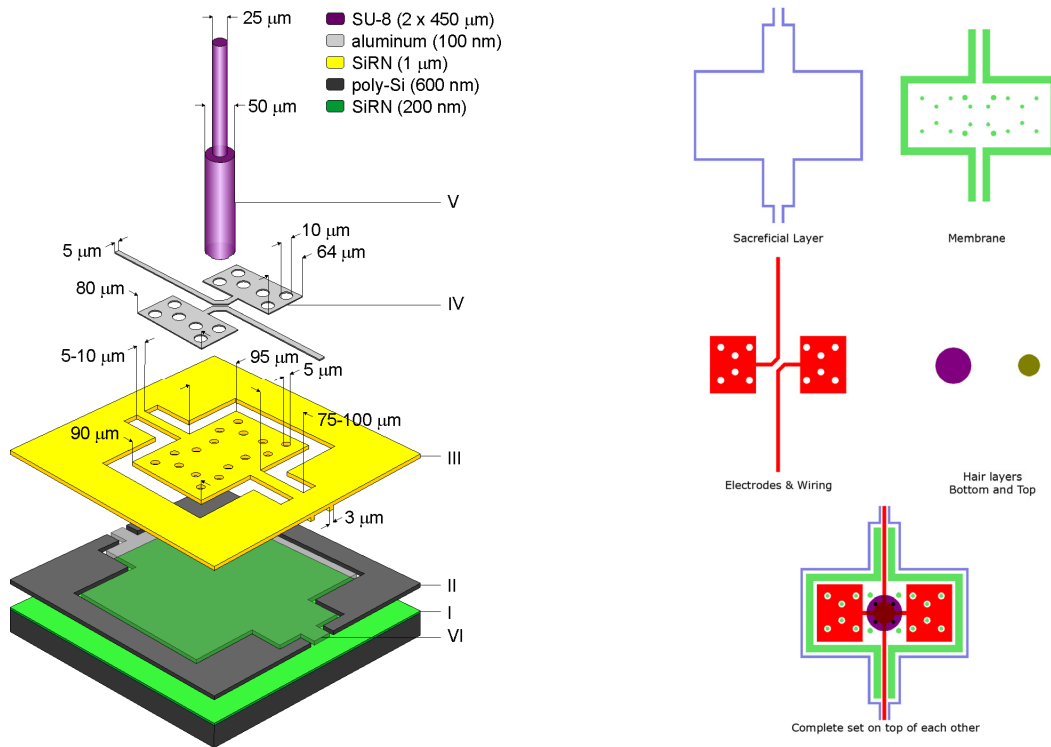


Fig. A-1: Left: regular hair sensor design overview showing materials, layer thicknesses, sensor dimensions and processing order. Right: top view of the set of masks necessary to fabricate the device.

In this appendix, the hair sensor reference numbers are displayed in figures showing a complete set masks on top of each other. To be able to distinguish hair sensors having long hairs (900 μm) from the ones having short hairs (450 μm), the mask of the bottom part of the hair is not displayed. So in the mask images displayed, absence of a circular shape represents a hair sensor with a short hair (450 μm).

Inline

This refers to the structures with three hair sensors in a row. The separation between the sensors is increased among the different structures. On the chip twelve of these rows each containing three sensors are available [Fig. A-2]. There are six groups of two structures, each group of two rows has a different separation between its sensors. In each row, the first sensor can be actuated by charging its capacitors. The remaining two sensors are able to move free under the viscous action of the flow. The distance between the hair sensors in the six groups is varied, separations of 100 μm, 150 μm, 200 μm, 300 μm, 400 μm and 600 μm are available. All the sensors in these structures contain hairs with a length of 900 μm. The individual structures are named "Inline" followed by the separation between the sensors and a character (A or B) referring to one of the two groups containing these structures on the chip (for instance 'Inline-150 μm-A'). The location of the different groups is shown on the complete mask of the chip at the end of this appendix.

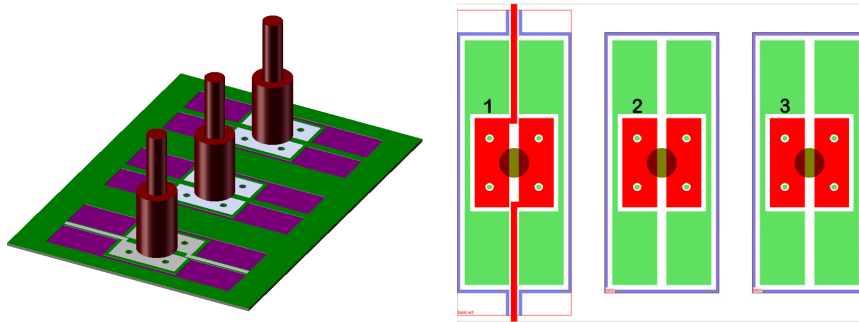


Fig. A-2: Left: row design of the 'Inline' series of hair sensor structures. Right: mask design of this structure (Inline-150 μ m).

Inline-Cmb

Inline-Cmb structures contain a set of two sensors in which the orientation of the second sensor is rotated 90° with respect to the first one [Fig. A-3]. The first hair sensor can be actuated and the second one is able to move freely. The viscous coupling chip contains three groups of two sensors arranged in this pattern. All six sensors have a 900 μ m long hair and the separation between the sensors in the groups is 188 μ m, 238 μ m and 288 μ m respectively. Again the separation between the sensors is added to the name to designate a particular structure.

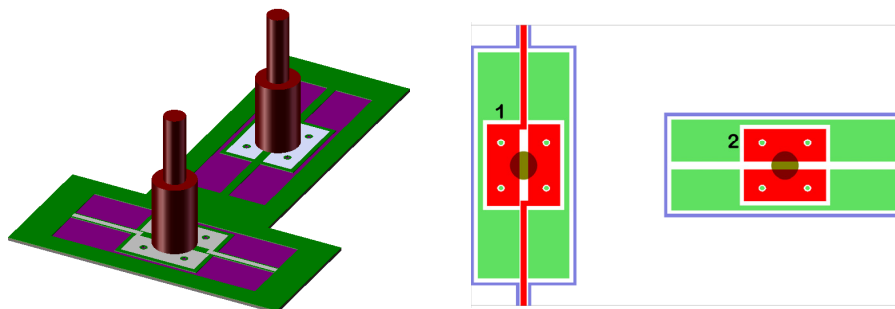


Fig. A-3: Left: design of two sensors having a different direction of sensitivity. Right: mask design of this structure (Inline-Cmb-238 μ m).

Sh-Array

In the shifted Array (Sh-Array) nine sensors with hairs of 900 μ m are arranged in a 1-2-1-2-1-2 pattern. The six rows are shifted with respect to each other [Fig. A-4]. On the chip three of these structures having separations of 113 μ m, 150 μ m and 200 μ m between the rows are available. In all three structures the hair sensor on the first row can be actuated.

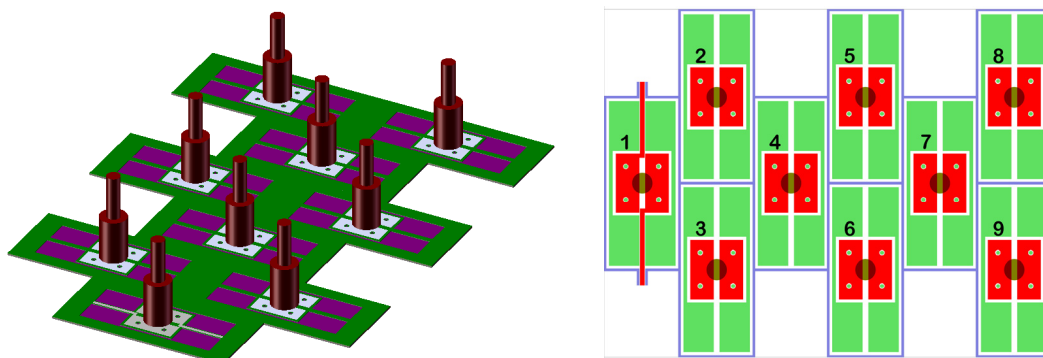


Fig. A-4: Left: design of a shifted array of sensors, Right: Mask design of this structure (Sh-array-133 μ m)

Sh-Array-Shrs

These structures are similar to the shifted row structures above. They consist of four sensors in a 1-2-1 arrangement [Fig. A-5]. The sensors on the second and third row have a hair only 450 μm in length. As discussed in the introduction, in the mask image of this structure the bottom part of the hair is absent to gain a better contrast between the hair sensors with long and short hairs. Again the distance between the rows in these structures is varied and the sensor on the first row can be actuated. Structures with separations of 100 μm , 150 μm and 200 μm between their rows are available on the chip.

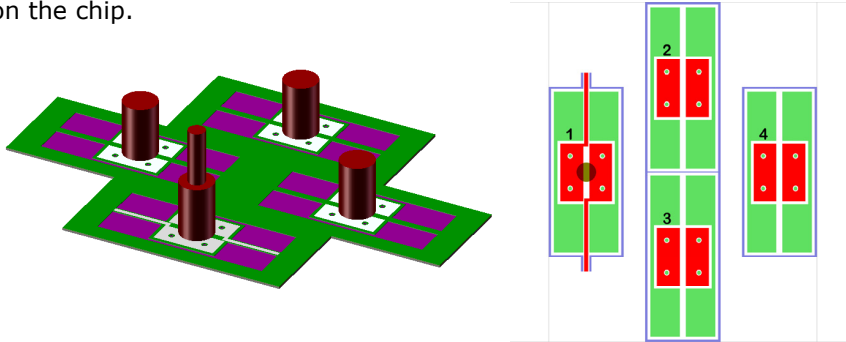


Fig. A-5: Left: design of a shifted array of hair sensors with short hairs. Right: mask design of the shifted array with short hairs structure (Sh-Array-Shrs-150 μm)

Array

In the array structures, hair sensors are arranged in a three by three matrix. The common features of the five different matrix structures on the experimentation platform are off course the matrix shape with three rows and three columns, so there are nine hair sensors in each design. A second common feature in these designs is the sensor in the centre. This sensor has a long hair (900 μm) and can also be actuated. The eighth remaining sensors can move freely. Each matrix design has a duplicate on the chip. The location and reference character (A or B) of each of the matrix designs is shown on the chip map at the end of this appendix.

Array-300

This is a basic matrix design, all nine hair sensors in this structure have a hair of 900 μm in length [Fig. A-6]. The separation between both the rows and the columns in this design is kept at 300 μm .

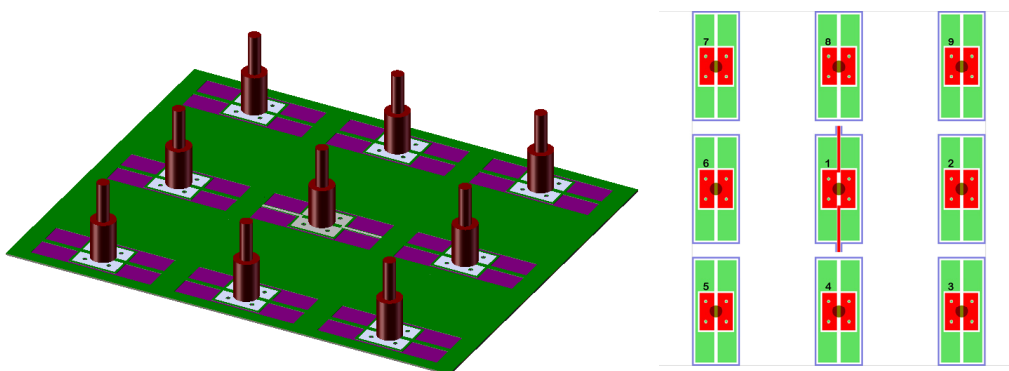


Fig. A-6: Left: matrix design, three rows of three sensors having a long hair. Right: Mask design of a matrix of sensors (Array-300 μm)

Array-300-Shrs

In this matrix the eight hair sensors surrounding the sensor in the middle have a short hair [Fig. A-7]. The separation between the rows and columns is kept at 300 μ m as well.

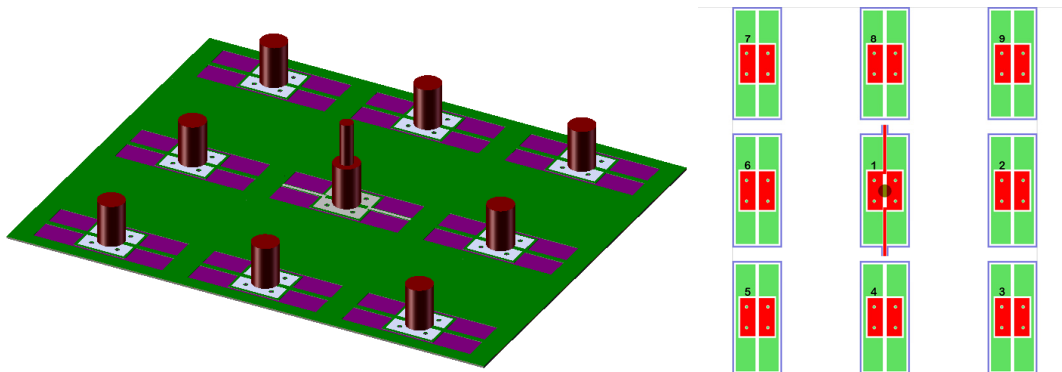


Fig. A-7: Left: Matrix design with the eighth surrounding sensors having a short hair. Right: mask design of this structure (Array-300-Shrs).

Array-Cmb and Array-Cmb-Shrs

In the last three matrix designs, the orientation of the four sensors having an even number is rotated 90° with respect to the other sensors. In the first of these three designs the separation between the sensors is kept at 300 μ m and all the sensors have a hair of 900 μ m (Array-Cmb-300 μ m) [Fig. A-8 A]. In the second design the distance between the sensors is reduced to 250 μ m (Array-Cmb-250 μ m)[Fig. A-8 B]. In the last design the separation is kept at 250 μ m but the length of hairs of the eighth sensors surrounding the sensor in the center is reduced to 450 μ m (Array-Cmb-Shrs-250 μ m) [Fig. A-8C].

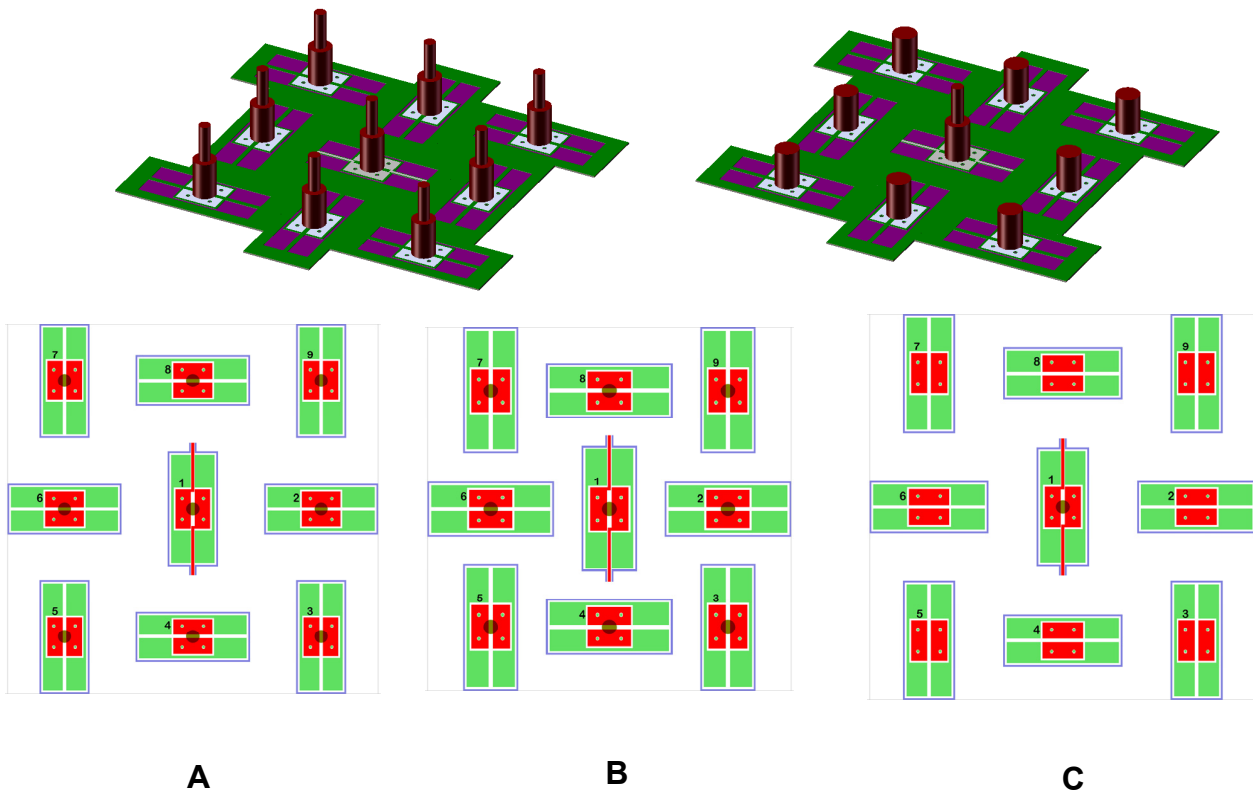


Fig. A-8: Upper left: Matrix design with the eight surrounding sensors having long hairs. Upper right: Matrix design with the eight surrounding sensors having short hairs. Lower: Masks of three matrix designs, A: separation 300 μ m, long hairs B: separation 250 μ m, long hairs and C: separation 250 μ m, short hairs.

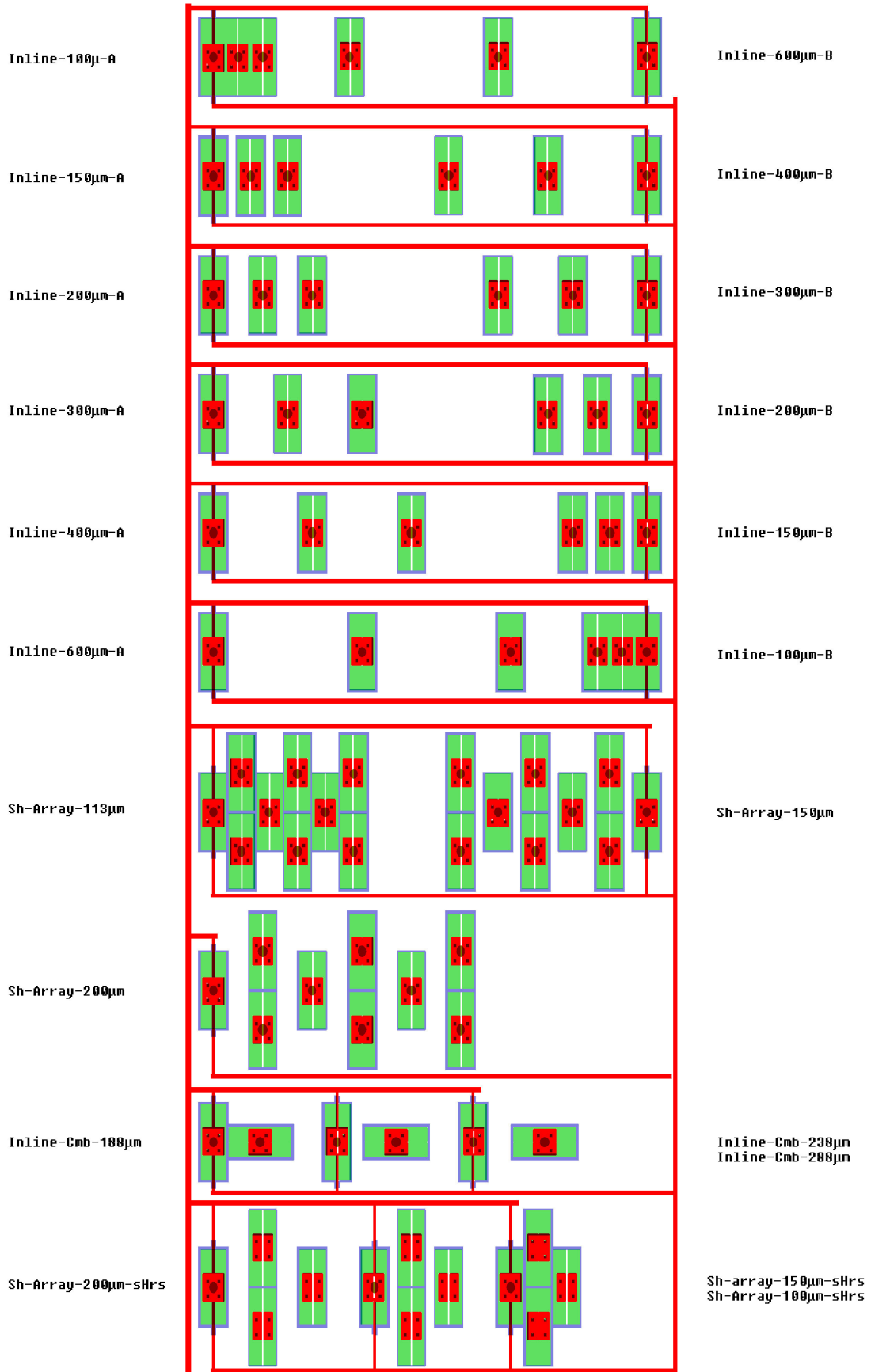


Fig. A-9: Overview of the top part of the chip design

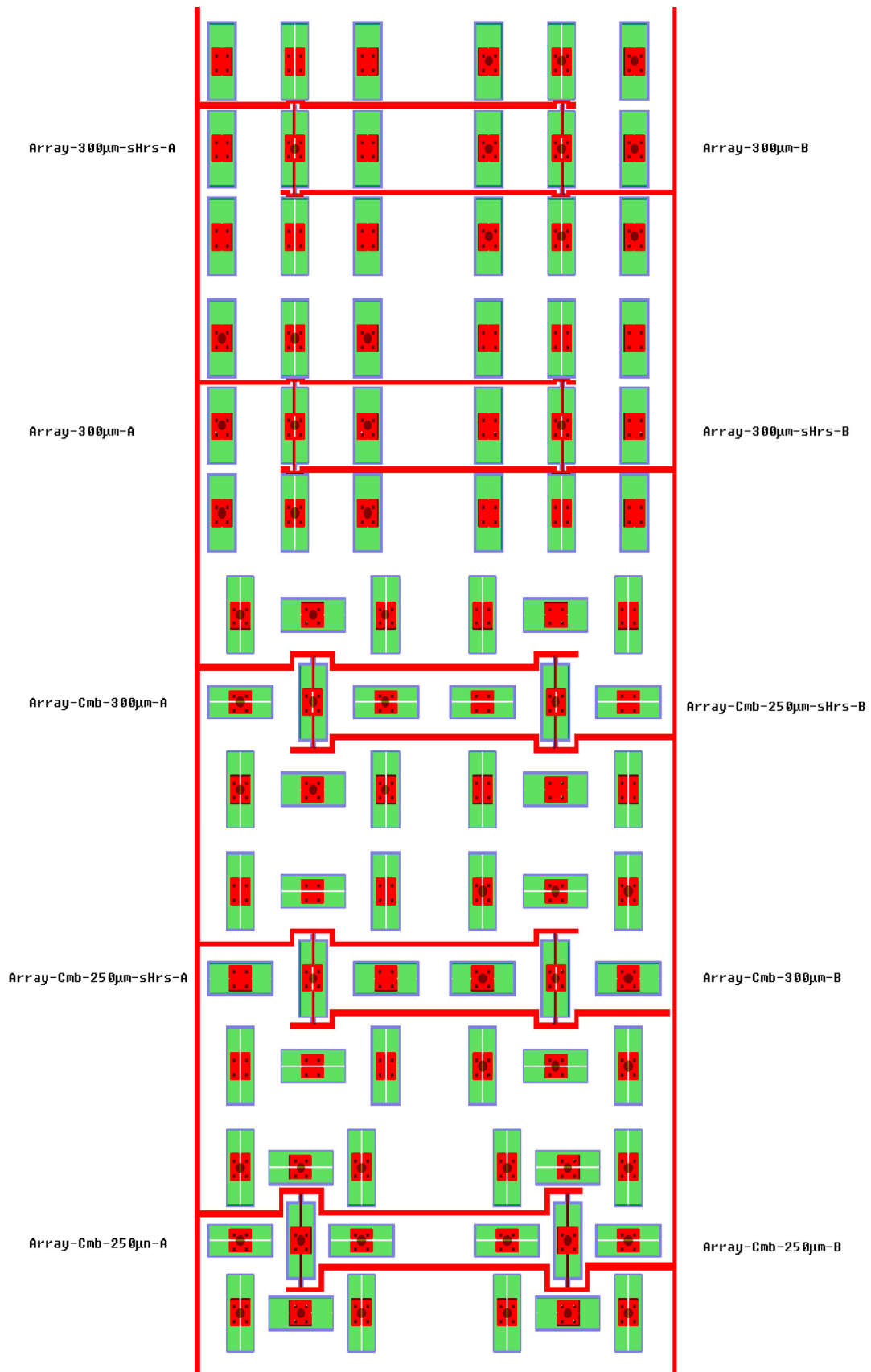


Fig. A-10: Overview of the bottom part of the chip design.